FOURIER-PLANE MODELING OF THE JET IN THE NUCLEUS OF THE GALAXY M81

by

ARVIND RAMESSUR

submitted in accordance with the requirements

for the degree of

MASTER OF SCIENCE

in the subject of

ASTRONOMY

at the

UNIVERSITY OF SOUTH AFRICA

SUPERVISOR: **PROF L L LEEUW**
CO-SUPERVISOR: **DR M BIETENHOLZ**

FEBRUARY 2017

Revised: December 2017

0.1 ABSTRACT

The mildly active nuclear region in the galaxy M81 (henceforth, M81*) is one of the nearest low-luminosity active galactic nuclei (LLAGN) whose structure is marginally resolved when probed with Very Long Baseline Interferometry (VLBI). Motivated by the way resolved radio sources usually appear on the smallest scales, i.e., a core with a one-sided jet structure, we developed a strictly one-sided, asymmetric triangular model, which we call ASYM, with brightness distribution along a line segment on the sky, with maximum brightness at one end of the segment fading linearly to zero at the other end. The ASYM model is compared and contrasted with an elliptical Gaussian model (hereafter, GAUS), by fitting existing VLBI data of M81* at 39 epochs between 1993 and 2003 at 8.4 and 5.0 GHz with the two models. Contrary to what we envisioned, we find that for 77% of our epochs, a simple GAUS model fits the visibility data of M81* at 8.4 GHz better (i.e., has a lower reduced χ^2) than the ASYM model. We conclude that M81* is not strictly a one-sided, asymmetric jetted source; as is thought to be the case for the majority of AGN observed at VLBI scales. Our results imply that M81* is mostly symmetrical with a significant jet counterpart which cannot be overlooked.

keywords: Galaxies: Active − galaxies: Individual (M81, NGC 3031) − galaxies: Sub-parsec-scale jet − galaxies: Supermassive Black Hole (SMBH) − Technique: Fourier-Plane Modeling − Instrumentation: Very Long Baseline Interferometry (VLBI) − VLBI: Astronomy & Astrometry.

0.2 DECLARATION OF AUTHORSHIP

UNIVERSITY OF SOUTH AFRICA
Department of Mathematical Sciences

In accordance with the appropriate regulations, I, Mr RAMESSUR Arvind; student ID: 53747429, hereby submit the above Research Master's thesis for examination.

(i) I declare that FOURIER-PLANE MODELING OF THE JET IN THE NUCLEUS OF THE GALAXY M81 is my own work and that all the sources that I have used or quoted have been indicated and acknowledged by means of complete references.

(ii) I further declare that I have not previously submitted this work, or part of it, for examination at UNISA for another qualification or at any other higher education institution.

(iii) The research work in this thesis was carried out under the supervision of Prof Lerothodi L. Leeuw at the College of Graduate Studies, University of South Africa, P.O. Box 392, Unisa, 0003 Pretoria, South Africa and Dr Michael F. Bietenholz at Hartebeesthoek Radio Observatory, P.O. Box 443, Krugersdorp, 1740, South Africa.

(iv) I have adhered to the 'Harvard system of referencing' for referencing, quotations, and citations in my thesis.

(v) I have not allowed and will not allow, anyone, to copy my work with the intention of passing it off as his or her own work.

....

SIGNATURE DATE (dd/mm/yy)

Mr RAMESSUR Arvind
arvind@hartrao.ac.za

0.3 ACKNOWLEDGEMENTS

I owe a great deal of gratitude to my two supervisors, Prof Lerothodi L. Leeuw and Dr Michael F. Bietenholz. Their extensive guidance, expertise, and constructive criticism ensured that this research project ran smoothly and brought about an original and significant contribution to knowledge in the field of radio astronomy. This thesis would not have been made possible to pursue and bring to fruition without a proper comprehension of theories, concepts, and programming skills which I have been fortunate to learn through multiple interactions with my supervisors, to whom I am indebted. Also, their useful comments, positive evaluation, and generous donation of time to proof-read this thesis are much appreciated.

Conducting this research (including the thesis write-up and amendments) was not an easy task, and rather, many issues had to be surmounted. Nevertheless, my friends and colleagues (Mekuanint Kifle Hailemariam and Sayan Basu) and my supervisory team were always there to inspirit my effort to prevail over these difficulties. Their suggestions, recommendations, and guidance provided such a boosting environment which enabled me successfully conduct this research master's thesis.

I would like to seize this opportunity to further express my gratitude to Dr Michael F. Bietenholz for providing me with the opportunity to become involved in a highly interesting and active area of research that I have found truly enjoyable to be a part of. His enthusiastic attitude and attention to details while allowing me considerable flexibility created a relaxed but focused working environment that has helped me to think critically and grow as a scientist. I look forward to many more years of continued support and more of his insights in the future.

There are far too many people from the Hartebeesthoek Radio Astronomy Observatory (HartRAO) who provided me with invaluable assistance during my research work in South Africa for me to list individually. However, I would like to give special mention to a few. Special thanks to Dr MacLEOD Gordon for sharing his know-how about research and management, which contributed to my self-development. I also wish to thank Mr Blose Siphelele, Dr Botha Roelof and, Dr Quick Jonathan for their technical assistance and ensured that the HartRAO server ran properly for the continuation of my research work; Mrs Coetzer Glenda for her hospitality and facilitating my stay at the HartRAO facility. Lastly, I am grateful to Prof Combrinck Ludwig, and late Dr Michael (Mike) Gaylard for their support, encouragement, and funding opportunities for me to attend the IAU 313 symposium in Ecuador.

There are several other people from the University of South Africa (Unisa) and elsewhere who stand out as worthy of mention. I wish to thank Prof Derck P Smits for imparting his knowledge about radio astronomy during journal club sessions. I would also like to extend my gratitude to the Mail & Guardian's science journalist, Sarah Wild, who assisted me to polish my writing style and lucidity so that I could easily communicate my research work to the general public. Also, special thanks to Prof Reitumetse Mabokela (University of Illinois, USA) for sharing her experience and expertise about the art of writing proposals for research funding.

0.3.1 Statement of Contributions

I would also like to acknowledge the following people and organisations/institutions which contributed to this research project:

1. This research has made use of NASA's Astrophysics Data System, NASA/IPAC[1] Extragalactic Database, (NED) which is operated by the Jet Propulsion Laboratory, California Institute of Technology, under contract with the National Aeronautics and Space Administration.

2. The LaTeX Typesetting program was used to generate this thesis, along with Adobe Illustrator 2015[2] for the graphical illustrations. The Gnuplot software was used to generate the various plots in this thesis.

3. Data reduction, imaging, and model-fitting were done using the following astronomical software:

   (i) NRAO Astronomical Image Processing System ($\mathcal{AIPS}$)[3],

   (ii) KARMA[4], and

   (iii) DIFMAP[5].

[1] http://ned.ipac.caltech.edu/

[2] http://www.adobe.com/africa/products/illustrator.html

[3] http://www.aips.nrao.edu/

[4] http://www.atnf.csiro.au/computing/software/karma/

[5] http://www.cv.nrao.edu/adass/adassVI/shepherdm.html

4. A python program was written by Dr Michael F. Bietenholz and fed into $\mathcal{AIPS}$ to generate our test data files in order to ascertain that our geometrical model was doing the correct minimisation.

5. This research work is supported by Hartebeesthoek Radio Astronomy Observatory (HartRAO)[6] and South African Square Kilometer Array (SA SKA)[7]. The financial assistance of the National Research Foundation (NRF) toward this research is hereby acknowledged.

[6]http://www.hartrao.ac.za/

[7]http://www.ska.ac.za/

Dedicated to my parents and my sister

Contents

List of Figures

List of Tables

0.4 THESIS OUTLINE

The chapters of this thesis are laid out as follows and a summary of the key points to take away are enumerated at the end of each chapter.

- *Chapter 1 - Rationale*: The opening chapter discusses the importance of studying AGN jets in a broader context. We discuss the rationale and uniqueness of this thesis including how this work complements and does not duplicate other researchers' efforts to understand and explain some fundamental questions relating to AGN jets. We also discuss how this research work may have some useful applications for astrometry and geodesy.

- *Chapter 2 - Radio Interferometry in a Nutshell*: The intent of this chapter is to convince the reader that producing an image is not always the best way to analyse VLBI data. We put emphasis that there is a lot to be learned by an inspection of the data in the visibility domain via the model fitting technique.

- *Chapter 3 - The Nuclear Region of the Galaxy M81*: This chapter summarises the current state of knowledge and provides a review of the past and ongoing research related to the central nuclear region of the galaxy M81. We describe the observations and data reductions of M81*. We also show representative images of M81 and M81* along with an animated time-lapse VLBI movie. We then highlight the problem statements and our motivation for coming forth with a new model.

- *Chapter 4 - Fourier-Plane Modelling*: This chapter deals with the scaffold and analytical expressions for some common models. We also derive our new geometrical model and conduct various tests to ascertain that our model is doing the correct minimisation.

- *Chapter 5 - Results and Discussions*: In this chapter, we analyse and discuss our results. We argue what we can learn as a result of this research work and most importantly, what will be learned that somebody else does not already know.

- *Chapter 6 - Conclusions and Future Outlook*: In the last chapter, we conclude and wrap up this thesis by discussing a perspective for the future.

Acronyms

AGN Active Galactic Nuclei. 2–7, 21–23, 32, 33, 35, 36, 38, 50, 62, 68–71, 74

ASYM Point-Source Approximation of an Asymmetric Triangle Model. 40–44, 49, 50, 53–55, 59–63, 67, 68, 70, 74

DOT Point Source Model. 43, 44, 53

GAUS Elliptical Gaussian Model. 38, 53–55, 59, 61–63, 67, 68, 70

ICRF International Celestial Reference Frame. 4, 5

LLAGN Low-Luminosity Active Galactic Nuclei. vii, 3, 5, 7, 22

SMBH Supermassive Black Hole. 2, 4, 6, 22, 23, 32, 70

SSR Sum-of-Squares Residual. 16–19

VLA Very Large Array. 14, 26, 27, 30, 59

VLBI Very Long Baseline Interferometry. 1–5, 7, 10–12, 15, 21–24, 26–28, 30, 32, 33, 35, 39, 68–70, 74

Nomenclature

Symbols

$M_\odot$	Solar Mass	$M_\odot \approx 1.989 \times 10^{33}$ kg
M81*	Nuclear region of the galaxy M81 (*pronounced* "M81 star")	
Sgr A*	Nuclear region of the Milky Way galaxy (*pronounced* "Sagittarius A star")	
$\mathrm{I}(x, y)$	Sky Brightness (Intensity) Distribution	
u-v	Projected baseline coordinates	
$\mathrm{V}(u, v)$	Visibility Distribution	
α	Spectral Index	
ν	Frequency of observation	
τ_ν	Optical depth	
Θ	Apparent source size	
λ	Wavelength of observed radiation	
θ	Angular resolution	
i	Index notation	
j	Imaginary Number	
$\mathfrak{F}\{\ \}$	Fourier transform operator	
§	Section	

Abbreviations

Decl. Declination

kpc kiloparsec

mas milli-arcsecond

P.A. or p.a. Position Angle

pc parsec

R.A. Right Ascension

Journal Abbreviations

A&A Astronomy and Astrophysics

AJ Astronomical Journal

ApJ Astrophysical Journal

ApJS Astrophysical Journal Supplements Series

ARAA Annual Reviews of Astronomy and Astrophysics

MNRAS Monthly Notices of the Royal Astronomical Society

PNAS Proceedings of the National Academy of Science

Organisation/Institution Acronyms

HartRAO Hartebeesthoek Radio Astronomy Observatory

IAU International Astronomical Union

NRAO National Radio Astronomy Observatory

NRF National Research Foundation

SKA SA South African Square Kilometer Array

UNISA University of South Africa

'Nature has devised numerous mechanisms by which the universe could become self aware, and where humanity could spring forth from the ashes of ancient supernovae and gaze upon the heavens to contemplate its origins. Astrophysical jets are one such mechanism.'

– D.A. Clarke

1 Rationale

1.1 Introduction to Active Galactic Nuclei & Jets

In the mid-1960s, astronomical observations revealed the existence of sources smaller than the resolution provided with connected-element interferometry. The causality arguments for the rapid intra-day flux variability and flat spectrum components of the nuclear region of quasars and radio galaxies imply that the radiation arose from the smallest physical regions, of the order of several light days, which translates into the apparent sizes of less than milliarcsecond on the sky plane (Dent, 1965; Sholomitskii, 1965). For instance, if Δt is the variability timescale, then the source cannot extend to larger scales than the light crossing time, i.e., the radius of the source, R, should obey $R < c\Delta t$[1]. The inferences made clear the need of angular resolution beyond what the connected-element interferometer could achieve to measure their angular sizes

[1]Doppler boosting effect has to be taken into account for a relativistically moving source, see §3.5.2

and to determine their structural variations (e.g., Shields, 1999). Hence, interferometric arrays with baseline lengths of thousands of kilometres were made possible through the development of a new technique known as Very Long Baseline Interferometry (VLBI). The theoretical framework for VLBI is introduced in § 2.2 of this thesis.

Being the only radio astronomical technique which probes the sky at milliarcsecond scales, VLBI provides a unique means to study and analyse the otherwise unresolved nuclear regions of extra-galactic radio sources, even at high redshift, at a resolution of about a parsec (pc). It also allows images of regions small enough to show morphological changes on human timescales to be made. Consequently, the advent of the global VLBI network triggered a series of subsequent high-resolution observations of bright and compact radio sources, known as Active Galactic Nuclei (AGN) - located in the nucleus of the parent galaxy - performed at various frequencies and with the time intervals on the order of several weeks to years.

There is a growing body of evidence that a Supermassive Black Hole (SMBH), which is a black hole of mass 10^{6-9} $M_{\odot}$[2], lurks in the nucleus of AGN and it is responsible for the observed nuclear activity (e.g., Miyoshi et al., 1995; Kormendy & Richstone, 1995). The inflow of matter occurring in the gravitational potential well, where the SMBH resides, leads to the release of an enormous amount of energy; a fraction of this energy is funnelled into relativistic jets[3] (e.g., Maltby & Moffet, 1962; Blandford & Znajek, 1977; Urry & Padovani, 1995) along the rotation axis of an accretion disc (Marek et al., 1998). It has been widely accepted for quite a while that essentially all AGN pass through a jet phase, i.e., they become active when sufficient amount of matter falls on them (Di Matteo et al., 2005).

The term "core" is used ambiguously in the literature. We define *core* as the physical core of the source, closely associated with the SMBH. The location of the core is therefore not dependent on either frequency or resolution. It is also notable that the existence of a core onto which accretion of the surrounding matter occurs can explain the very high efficiency of energy release, and the compactness of the nuclear regions. The energy source of activity of galactic nuclei can be linked to both the rotational energy of the SMBH and the energy of the accreting matter. For any given mass, there is a critical luminosity called the Eddington limit[4] (Krolik, 1999). Consequently, the

[2]Where, $M_{\odot} \approx 1.989 \times 10^{33}$ kg is the solar mass.

[3]The term *jet* was probably first coined by Baade & Minkowski (1954) to the "protrusion" out of the nuclear regions of the nearby galaxy M87.

[4]The luminosity at which radiation pressure on free electrons balances the gravitational force acting on

observed luminosity of the central nuclear region of AGN ($10^{43} - 10^{47}$ erg s^{-1}) demand minimum central masses in the range $10^5 - 10^9$ M$_\odot$, supporting the hypothesis that the detected AGN are in fact associated with SMBH cores.

Being synchrotron emitters[5], AGN jets are prominent in radio frequencies (Blandford & Konigl, 1979). Interestingly, without taking full advantage of the aperture synthesis technique developed by Martin Ryle[6] (Ryle & Hewish, 1960), the relatively small size of the synthesised beam of the Caltech interferometer led to the identification of quasars (Schmidt, 1963), the determination of radio source spectra (Kellermann, 1964), and the detection of extragalactic radio sources displaying two-sided jets which are symmetrical (i.e., jets are often close to being equal in brightness) at large scales (Fomalont, 1969). However, since the inception of the VLBI technique, an overwhelming number of AGN jets observed at milliarcsecond scales have shown to be predominately one-sided and appear highly asymmetric (i.e., one side, generally denoted as jet is more pronounced than its counterpart) (e.g., Lister et al., 2009a,b; Cawthorne, 1991).

1.1.1 Low-Luminosity AGN (LLAGN)

About 40% of nearby bright galaxies and a majority of the population of AGN show evidence of low-level nuclear activity with Hα luminosity $< 10^{40}$ erg s^{-1} (e.g., Ho et al., 1997b,a; Ho, 2008). Low-Luminosity Active Galactic Nuclei (LLAGN) present in compact nuclear radio sources share characteristics with their high-luminosity counterparts - Seyfert and radio galaxies. One such characteristic is the presence of compact nuclear regions and pc-scale jets (Nagar et al., 2005), where the flat-spectrum of the nuclear radio source is generally interpreted as the synchrotron self-absorbed base of the jet.

LLAGN typically have small angular size (Anderson & Ulvestad, 2005); an exemplar being the galaxy M81 which has the distinction of being the nearest spiral galaxy hosting an LLAGN

the accreting matter. $L_{Edd} \approx 1.51 \times 10^{38} (M/M_\odot)$ erg s^{-1}, where $M_\odot \approx 1.989 \times 10^{33}$ kg is the solar mass.

[5]The synchrotron radiation arises due to relativistic charged particles gyrating in a magnetic field. The magnetic field which is generated in the vicinity of the core which is assumed to occur in an accretion disc. Detailed considerations of radiative processes in AGN jets is beyond the scope of this thesis. Ancillary information about the physical principles can be found in Rybicki & Lightman (1979), Chapters 6 and 7.

[6]In 1974, Professor Martin Ryle shared a Nobel Prize in Physics for developing the aperture-synthesis technique; see Chapter 2 for details.

(dubbed M81*), which is in fact only marginally resolved, and which has an elongated radio structure, identified as a sub-pc scale jet (Bietenholz et al., 2000).

1.1.2 Sgr A* and its nearest sibling

Although it is a unique place in our own Galaxy, the Galactic Centre (GC) is undoubtedly not unique in the universe. For this reason, the GC has frequently been used as an analogy for other distant galaxies for us to better understand the nature of their nuclear regions. The prototypical and well-studied radio source, Sagittarius A star, Sgr A* in our GC is identified with a nuclear SMBH of mass 4.3×10^6 $M_\odot$ (Ghez et al., 2008; Gillessen et al., 2009). However, the Galactic Centre of Sgr A* in our own galaxy is not the best place to dig for answers. This is predominantly due to the intrinsic weakness of the GC, the obscuration in the Galactic plane, and scatter broadening[7] (Doeleman et al., 2001). The apparent angular size of Sgr A* shows a wavelength, λ^2 dependence (at centimetre wavelength) of the scattering effect and it has been pushing the VLBI observations of Sgr A* to much shorter wavelengths, towards vanishing image blurring (Bower et al., 2006). Moreover, nearby background sources are also scatter-broadened, which make it difficult to calibrate the longest VLBI baselines.

Unlike Sgr A*, the compact nuclear regions of the weakly active galaxy M81 is not strongly affected by obscuration or scatter broadening, and it is marginally resolved with VLBI at various frequencies, e.g., see Bietenholz et al. (2000). VLBI observations have shown that the relatively quiet SMBH in M81* powers a jetted radio source, much weaker in brightness and smaller in size than those of distant quasars, but larger and more luminous than Sgr A*. Qualitatively, Sgr A* has very similar physical properties to that of M81* and it was suggested by Reuter & Lesch (1996) that M81* may be a more energetic version of Sgr A*. Therefore, the radio source of the galaxy M81 can be considered as the nearest analogue of Sgr A*, at a higher power level.

[7]Scatter broadening is the effect which arises from scattered radio waves by the intervening interstellar medium owing to electron density fluctuations. It causes observable effects such as fluctuations in flux density (scintillation), temporal broadening of a pulse signal, angular broadening of a source, and image wander (Rickett, 1990).

1.1.3 VLBI Astrometry and Geodesy

A pertinent question is how to reliably estimate the core position in AGN. In other words, how to truly establish a kinematically stable point at the sub-milliarcsecond level in AGN which can be used to build highly accurate reference frames such as the International Celestial Reference Frame (ICRF) which serve geodetic purposes as well.

Most extragalactic radio sources are at redshifts of ~ 1.0 and thus should show no detectable proper motion and their astrometric position should be invariant with time. While the sources are indeed stable with time and exhibit no detectable motion on the long term (e.g., Bartel et al., 1986) at shorter time scales (months to years), however, instabilities at the level of several hundreds of microarcseconds are detected (Ma et al., 2009). Such instabilities are usually attributed to changes in intrinsic structure that the sources undergo which can, in turn, affect the precision of their position estimates and hence potential VLBI astrometric instabilities (e.g., Fey & Charlot, 2000).

For the sake of checking the consistency of the positions of the ICRF sources and their stability, one needs to monitor potential variations in their structures (Fey et al., 1996). Moreover, apart from conducting new VLBI observations of ICRF sources, older data are also imaged and re-analysed (e.g., Piner & Kingham, 1997). Whenever significant discrepancies in the accuracy of the source positions are discovered in such comparisons, the particular sources in question are considered less reliable for use and are dropped from the geodetic observing schedules.

An example to illustrate the above discussion is the source 3C 273. When it was imaged in 1986, 3C 273 showed measurable internal structure, which made it impossible to truly establish a kinematically stable point at the sub-milliarcsecond level without detailed study; the jet components were stretched out to over several mas from its nucleus (Sovers et al., 1998). Comparative images at other epochs show the rapid motion of the components of the jet in 3C 273 along with recurrent jet components. After 1986, this particular source was discarded from most geodetic observing schedules due to its poor astrometric quality.

1.2 Aims and Objectives

Our main aim in this thesis is to understand the geometry of an LLAGN at VLBI scales. A promising candidate that we used for our investigation is the marginally resolved LLAGN in the nearby galaxy M81 identified with a sub-pc scale jet structure (see Chapter 3 for details).

In LLAGN, the jet nature in compact radio nuclei has not been yet established and the question is left open whether in fact an LLAGN show resemblance, physically and/or geometrically to that of high-luminosity AGN, i.e., a quasar and radio galaxies. We briefly discussed above, one of the intriguing characteristics of pc scale jets of AGN observed at the smallest scales is that they are predominantly one-sided. If M81* could be a missing link between Sgr A* and high-power AGN, the study of M81* might therefore not only disclose its true nature but could also bridge the gap in our understanding between the radio-loud/radio-quiet AGN dichotomy (e.g., Kellermann et al., 1989).

The secondary aim of this thesis is our desire to alleviate the burden of source position maintenance in astrometry by identifying an accurate estimation of the core position in AGN. However, the identification of the position of the most stable point (i.e., the core in a galaxy and other AGN) is a hard nut to crack. One method to constrain the location of the core of an AGN is by determining astrometrically which component is stationary with respect to a physically unrelated source that can be assumed to be stationary on the sky. Such a method has previously been used, for instance by Bartel et al. (1986) for the source 3C 345, and later by Bietenholz et al. (2004) for M81*, using the centre of SN 1993J as an astrometric reference point.

The issue of position variation in AGN can only be solved in the future if one can identify and use a truly kinematically stable point in the sky. In this thesis, a new strategy is exploited to provide a reliable estimate of an already well-established core position in M81* and the approach herewith - though ambitious an attempt - may also be applicable to other AGN serving the purposes for both astrometry and geodesy.

To recapitulate, insufficient resolution due to the baseline length of our instrument (see Chapter 2) limits our scope to elucidate AGN jets activity and/or to pin down its core position. However, one can resort to other means to achieve similar objectives; by observing source structure on larger scales (from sub-parsec to parsec scales) at various frequencies and epochs, by observing the source for a longer period of time; up to 24-hours, and by employing different astronomical

techniques such as imaging and/or model-fitting in the Fourier-plane.

As we will further discuss in Chapter 2, the imaging technique approach suffers from deconvolution errors, and the noise statistics are influenced by the non-linear deconvolution procedure. In essence, our objective in this thesis is the preference of the Fourier-plane model-fitting technique over imaging which allows us to fit a simple parametric model directly to the interferometric observables. The interferometric observables are also known as visibilities and they embody important information about the source brightness distribution. A source's geometric properties such as its positions, component sizes, and separation of its discrete components significantly smaller than the beam can be measured via model-fitting, provided the signal-to-noise ratio is high.

Fits for mathematically simple component shapes, such as a point source, a circular and/or elliptical Gaussians are generally preferred for AGN. However, in view of the fact that the AGN jet in M81* has an asymmetric appearance (images along with a VLBI movie are shown in Chapter 3), developing a more sophisticated model that reflects the shape of M81* could be more useful.

Summary of Chapter 1 - Rationales:

1. This chapter served as a preface whereby a short chronological overview of the VLBI technique and progress made to understand the nature of AGN are briefly discussed.

2. We highlighted that one of the intriguing characteristics of well resolved AGN jet is that they are quite one-sided, with the jet being intrinsically much brighter than its counterpart.

3. We then narrowed down our attention to the low-power AGN and disclosed that the LLAGN that the galaxy M81 hosts is unique in the sense that it is marginally resolved by virtue of its closeness from Earth, and it is unaffected by obscuration and scatter broadening unlike our own Milky Way galaxy.

4. We pointed out that a detailed analysis of the source structure and its core position are impeded due to the source large nuclear size and the self-absorbed base of the relativistic jet of AGN.

5. Moreover, we briefly discussed how an attempt of locating a kinematically stable point at $\sim$ sub-milliarcsecond level in a nuclear radio source could be beneficial for Astrometry and Geodesy.

6. Finally, the aims and objectives of this thesis are briefly highlighted and we emphasised

that the Fourier-plane modelling approach would be used to better understand the nature of M81* and to estimate its already well-established core position which could, in turn, be used to pin down the core position of other AGN.

'The initial mystery that attends any journey is: how did the traveler reach his starting point in the first place?'

– LOUISE BOGAN, *Journey Around My Room.*

2

Radio Interferometry in a Nutshell

2.1 Introduction to Aperture Synthesis

Angular resolution and sensitivity impose fundamental limits in observational astronomy. Observations with a single element telescope have limited angular resolution which is set by diffraction. Instruments responding to the emission from a point source located at infinity (i.e., a plane wave), is the Fourier transform of the aperture distribution, and the width of the Point Spread Function (PSF) of the telescope determines the smallest angular scale that it can resolve.

Typically, the telescope diameter, D limits the angular resolution, θ through the ratio λ/D, where λ is the wavelength of observed electromagnetic radiation. So, the diffraction limit decreases with both an increasing observing frequency (or decreasing wavelength) and an increasing aperture of the instrument. Therefore, the most plausible way to achieve a higher angular resolution in order

to resolve a radio source of small angular size, at a given frequency, is to increase the instrument aperture. The Arecibo radio telescope (D = 305 m) in Puerto Rico and the Five-hundred-meter Aperture Spherical radio Telescope (FAST) in China, which is currently the largest single-dish radio telescope on Earth, yield an angular resolution of $3'$ and $1.7'$ respectively at a wavelength of 21 cm. To have a diffraction limit of $1''$ at a wavelength of 21 cm, the diameter of the radio telescope would need to be $\sim$ 52 km! Budget and engineering limitations prevent erecting a dish of $\sim$ 52 km. Instead, a significantly large aperture can be synthesised from two or more radio telescopes to increase the resolution above the diffraction limit for a single dish.

Radio interferometry is a technique where two or more radio telescopes - with antenna spacings known as baselines - are used to observe a radio source in synchrony. The incoming signal from a radio source incident on each pair of antennas' receiver system with a certain path difference in the array is combined[1] to provide a measure of the correlated flux density, see e.g., Thompson et al. (2001, chap 3). The interferometer does not directly measure the structure of a source but measures the Fourier transform of the sky brightness distribution $\mathrm{I}(x, y)$ from Fourier components $\mathrm{V}(u, v)$ for all baselines in the array recorded at discrete (u, v) points or visibilities $(u_k, v_k), k = 1, \ldots, \mathrm{M}$. The u-v coordinates correspond to the projected baseline, measured in wavelengths.

The fundamental equation of interferometry is typically derived by introducing the Van-Cittert Zernike Theorem (VCZ) (Thompson et al., 2001, chap 3), where the interferometric observable (i.e., the complex visibility) V is the measured spatial coherence function at a particular u-v coordinates on a baseline:

$$\mathrm{V}(u, v) = \int\int \mathcal{A}_N(x, y)\mathrm{I}(x, y)e^{-2j\pi(ux+vy)}dxdy,^{2} \tag{2.1}$$

where, (x, y) specifies the direction cosines relative to the phase-tracking centre. The $\mathrm{V}(u, v)$ is complex valued (and has units of flux density, e.g., Jy), (u, v) denotes the projected baseline coordinates, and therefore the spatial frequencies of the brightness distribution, measured in wavelengths. $\mathrm{I}(x, y)$ is the sky brightness distribution of the source (e.g., Jy beam^{-1}) and $\mathcal{A}_N(x, y)$ is the normalised reception pattern of the antenna.

Put differently, the plane wave which reaches the antennas is the Fourier transform of the point source of radio emission, and two-element interferometer - a single baseline - measures a single

[1]The combination of these two signals is done in the correlator, which behaves like a multiplier and integrator with respect to time (Thompson et al., 2001, section 1.3).

[2]Unless otherwise specified, all integral limits will be assumed to be from $-\infty \rightarrow +\infty$

spatial frequency (a visibility or u-v) component of the Fourier transform of the source brightness distribution, i.e., one angular scale. Therefore, an interferometer can also be treated as a spatial filter permitting only some of the spatial frequencies of the Fourier transform of the source brightness distribution. Consequently, the angular size scales observable by an interferometer depend on the range of baseline lengths: the shortest baseline defines the largest observable structure size while the longest baseline dictates the smallest observable structure, i.e. angular resolution.

In a similar manner, we make a transition to synthesise an aperture by the simultaneous use of several interferometer baselines of an array of pairwise connected elements and subsequently, a large number of spatial frequencies or visibilities can be made possible to be observed. Moreover, as the Earth rotates, the projected length and orientation of each baseline changes thus adding more visibilities and trace ellipses in the u-v plane. The superposition of all the ellipses with the phase-tracking centre as their origin from all the baselines for certain array is called the u-v *plane coverage*; zero on this plane corresponds to a zero length baseline, while the maximum dimension of the u-v plane is determined by the maximum baseline length in each direction. Since the visibility is a complex quantity, $\mathrm{V}^*_{ij}(u,v) = \mathrm{V}_{ij}(-u,-v)$ leads to two arcs in the u-$v$plane; symmetric to the u-v origin (e.g., see Figure 3.4 for an illustration).

A complete reconstruction of an arbitrary brightness distribution is only feasible if all the points in the u-v plane are measured. Nevertheless, one usually does not have a complete u-v coverage for an interferometer but only *samples* at a limited set of points in the u-v plane. In order to densify the u-v coverage - in the aim of reducing the holes in the u-v plane - one could either increase the number of antennas in an array or observe the source for a longer period of time.

2.2 Very Long Baseline Interferometry (VLBI)

The advent of the atomic clock made it possible to simultaneously observe a radio source using intercontinental baselines. As stated earlier, the longer the baseline (which corresponds to smaller spatial frequencies), the finer are the structures that an interferometer can detect. In contrast, shorter baselines are sensitive to large scale structures. VLBI facilities such as American Very Long Baseline Array (VLBA) and the European VLBI Network (EVN) are usually outfitted to perform VLBI observations with baselines of different length. For VLBA antennas, the short

baselines are clustered around the VLA[3] to provide sensitive baselines between the VLBA and VLA in phased-array mode, and the two outermost antennas Mauna Kea (Mk) and St. Croix. (Sc) provide the longest baseline of 8 611 km in the VLBA array. In the global array, the baseline length between Mauna Kea (Mk) and Effelsberg (Eb) is 10 328 km (see Figure 3.2). With a global array with a maximum baseline spanning up to 10 000 km (which is $\sim$ 78% the diameter of Earth), we can achieve an angular resolution of $\sim$ 1.51 and $\sim$ 0.90 mas at 5.0 and 8.4 GHz respectively.

In VLBI, the radio telescopes are not physically connected via cables, and therefore, direct correlation of the signal is not possible. The measured signal is time-stamped at each station and recorded on a hard drive pack. After the observing session, the pack is shipped to the correlator, where the data are re-synchronised according to the time labels, and then correlated by multiplying and averaging. The observer receives the correlated visibilities which have to be calibrated out personally as errors are introduced to the data during the observation and correlation process. Since this thesis made use of self-calibrated VLBI data, we digress slightly to discuss calibration in the upcoming section.

2.2.1 Calibration Techniques for VLBI

The radio waves emitted by a radio source suffer from errors in both amplitude and phase. Consequently, they are treated separately in the calibration process. Amplitude errors mostly arise from faulty calibration of the system temperature of individual antennas and errors in the determination of the aperture efficiency. The error in the amplitude leads to the overall brightness offset of the source. The electronics associated with a radio telescope and variations in the refractive index of the atmosphere are mostly responsible for the error in the phase which in turn leads to the loss of source structure information. *Gains* refer to the instrumental, positional, and atmospheric contributions to corrupting the true amplitude and phase of the incoming radio waves. Calibration involves the determination of the amplitude and the phase of the complex gain in order to retrieve the true visibility distribution.

The relationship between the measured and the true visibility can be written as:

$$\mathrm{V}_{\mathrm{ij}}^{\mathrm{M}} = \left(\mathrm{G}_{\mathrm{i}} G_{\mathrm{j}}^{*}\right) \mathrm{V}_{\mathrm{ij}}^{\mathrm{T}} + \mathrm{a}_{\mathrm{ij}} + \epsilon_{\eta \mathrm{ij}}, \tag{2.2}$$

[3]The Karl G. Jansky Very Large Array (VLA) is a radio astronomy observatory located in central New Mexico and it consists of 27 radio antennas of D = 25 m in a Y-shaped configuration. For more information, please visit: http://www.vla.nrao.edu/

where the first term on the right-hand side is the product of the complex gains of antennas i and j. The second term, G_{ij} represents the gain of the baseline made by antennas i and j, and is mainly due to the correlator gain errors, a_{ij} is an offset term, while ϵ_{ij} is the system noise term.

For connected-element interferometer, calibration relies upon the observations of a calibrator source of known or assumed structure, usually unresolved of known (almost constant) flux density over a long time interval (amplitude calibrators), and known (a stable) position (phase calibrators). A calibrator source near[4] the source of interest, whose true visibility is known due to the aforementioned properties of the calibrator, the antenna gains can be solved as a function of time. Interpolation of these gain solutions then provides approximate values for the use in the correction of the source visibility data (Cornwell, T. and Fomalont, E. B., 1999).

However, in VLBI calibration, due to temporal and spatial variations in the atmosphere, the inferred values of G_{ij} from a calibrator may not apply to the source observed at a different time, and in a different part of the sky. This implies that unlike the connected-element interferometer, where calibrator sources are used to calibrate the absolute phase of the visibility data, in VLBI, only the delay and delay rate (i.e., the derivative of phase with frequency and time respectively) are calibrated. Since VLBI requires high instrumental stability, the absolute phase is usually left uncalibrated (Cornwell, T. and Fomalont, E. B., 1999). Consequently, absolute position determination is often waived in VLBI observations. Another obstacle is that on VLBI scales, most compact sources are also the most variable in flux density and cannot be used directly to supply the gain amplitudes and phases.

The self-calibration technique can be used to circumvent the need for stable flux calibrators on VLBI scales. The basic principle of self-calibration is to consider the antenna gains as free parameters (i.e., allowed to be degrees of freedom in the determination of the source brightness distribution) that can be iteratively adjusted to provide the best match between an assumed model of the source of interest and the set of observed visibilities (Cornwell, T. and Fomalont, E. B., 1999).

[4]The separation and frequency of nodding depend on the observing band and the maximum baseline length.

2.2.2 Sparsity of VLBI observations and Imaging

As discussed above, the interferometric array measures the visibility function but for scientific purposes, an image of the source brightness distribution is usually required. How do we convert from one to the other? Before proceeding further, please note that since this thesis predominantly deals with non-imaging techniques, the intricacies of the imaging process are only glossed over here.

In principle, the visibility distribution $\mathrm{V}(u,v)$, and the sky brightness distribution $\mathrm{I}(x,y)$ form a Fourier pair:

$$\mathrm{V}(u,v) = \int\int \mathrm{I}(x,y) e^{-2j\pi(ux+vy)} dxdy \tag{2.3}$$

So we can obtain the sky brightness distribution by a Fourier inversion:

$$\mathrm{I}(x,y) = \int\int \mathrm{V}(u,v) e^{2j\pi(ux+vy)} dudv \tag{2.4}$$

A two-element interferometer measures a single u-v component of the Fourier plane of the radio source brightness distribution. The use of more than such two-element interferometers or observation with one interferometer, along with taking into account the Earth's rotation is needed for restoration of the entire Fourier plane. For an optimal amount of information of a radio source, it is desirable to recover a maximum number of u-v points. For an interferometer of N antennas, there are $\mathrm{N}\,(\mathrm{N}-1)\,/\,2$ u-v points in a single measurement. For example, the Very Long Baseline Array (VLBA) has 10 antennas and yields 45 possible baseline combinations. When observations are done in a "snap-shot mode", the visibility function is measured only at the 45 points on the u-v plane, and when Earth rotation synthesis is employed, each of those 45 points becomes an arc and subsequently an ellipse for full Earth-rotation synthesis (e.g., see Figure 3.4 for an illustration).

However, in practice, the true visibility function $\mathrm{V}(u,v)$ is not available and one usually has noisy and poorly calibrated samples of the visibility function at discrete locations in the Fourier plane. Omitting the role of noise and calibration errors, one can represent the measured visibility, $\mathrm{V}^{\mathrm{M}}(u,v)$ by introducing the *sampled* visibility function $\mathrm{S}(u,v)\mathrm{V}(u,v)$, i.e.,

$$\mathrm{V}^{\mathrm{M}}(u,v) = \mathrm{S}(u,v)\mathrm{V}(u,v), \tag{2.5}$$

where the sampling function $\mathrm{S}(u,v)$ is unity at measured (u,v) and zero where no data are sampled.

Substituting this sampled complex model visibility function into the Fourier inverse, we obtain

not the true image $\mathrm{I}(x, y)$ but an inferior image, the *dirty* image or dirty map:

$$\mathrm{I}^{\mathrm{D}}(x, y) = \int\int \mathrm{S}(u, v)\mathrm{V}(u, v)e^{2j\pi(ux+vy)}dudv \tag{2.6}$$

The *dirty* image I^{D} is the Fourier transform of the *sampled* visibility function:

$$\mathrm{I}^{\mathrm{D}} = \mathfrak{F}^{-1}\{(\mathrm{SV})\} \tag{2.7}$$

Applying the convolution theorem, we find that the dirty image is the convolution of the true or desired image I^{T} with a dirty or synthesised beam B or the point spread function (PSF) of the synthesis array, corresponding to the sampling function:

$$\mathrm{I}^{\mathrm{D}} = \mathrm{B} \star \mathrm{I}^{\mathrm{T}}, \tag{2.8}$$

From this point, we have seen that an initial dirty image can be formed from the visibility samples collected by an interferometric array. In order to mitigate the effect of Fourier plane sampling deficiencies or artefacts in the dirty image, one can use some deconvolution methods such as the Högbom CLEAN algorithm (Högbom, 1974) to produce a "clean" image. The residual amplitude and phase errors that are still left in the visibility data lower the quality of the image, and as such, self-calibration can be used to correct the antenna gains.

2.3 Non-Imaging Data Analysis

To re-iterate, an interferometer measures the Fourier transform of the sky intensity distribution or sky brightness distribution $\mathrm{I}(x, y)$ from Fourier components $\mathrm{V}(u, v)$ for all baselines in the array recorded at (u, v) points $(u_k, v_k), k = 1, \ldots, \mathrm{M}$.

With a two-element interferometer, M may range from ten to a few hundred and up to over a million with a multi-element array such as the Very Large Array (VLA). For large M, ergo collection of measured visibilities, the conventional method of using interferometry allows for an image reconstruction through an inverse Fourier transform whereby the sky brightness of the observed source in the sky can be recovered as discussed in the sections above. When combined with certain deconvolution algorithms, such as the Högbom CLEAN algorithm (Högbom, 1974), this approach of imaging a set of visibilities may be effective if we are dealing with relatively extended sources.

However, for small M and if the source observed is very compact, relative to the diffraction limit of the interferometer, imaging of the source can be problematic. The source size estimation, based on measurements performed in the sky plane may be prone to strong biases. For instance, the Fourier transform involved in imaging spreads errors that are localised in the (u, v) plane throughout the image, so different pixels in an image will have correlated errors, while measurements at different points in the (u, v) plane are largely uncorrelated (Taylor et al., 1999). Thus, for such cases, the quantitative analysis including estimates of errors in the derived quantities is often best performed in the (u, v) plane via a technique known as *model-fitting*, especially if a reasonable model for the source can be assumed and one can fit the Fourier transform of the model directly to the visibility measurements. Also, as we shall discuss in depth in the upcoming sections, some quantitative astronomical questions can be addressed better in the visibility domain than in the image plane.

2.3.1 Why Model Fitting?

In VLBI, model-fitting[5] is the choice for quantitative analysis of a source which is structurally simple to be accurately represented by one or a collection of well-separated, discrete components, for example, point sources, or circular/elliptical sources with a Gaussian distribution of flux. The choice of positions and sizes of the model component is done based on the visual inspection of the map. However, the form of the chosen model may not be correct, then it becomes necessary to explore a *range of different model types*.

There are two classes of model:

1. *Physical models* start with a physical picture including densities, opacities, and sources of energy. Typically a radiative transfer calculation is used to create a synthetic image which can be compared to observations.

2. *Geometric models* are simple shapes that describe the radio emission regions, i.e., features of the source but without any physics involved. Geometric models are useful for very simple cases when a source is marginally resolved or when physical models are too complex with far too many unknown parameters. Turning to geometrical models may allow us to narrow

[5]Model-fitting was the way data were handled in order to discern source structure in the early days of radio interferometry. A classic example is the model of Cygnus A, which Jennison and Das Gupta fitted to interferometry data at 2.4 m wavelength in 1953 (Jennison & Das Gupta, 1953).

down the possibilities of physical models and in extracting some useful information. For instance, geometrical models can be used to extract basic parameters, typically the size of the emission regions in the cases where physical models are not available.

For a given a set of observations, one is often required to examine the visibility data directly by fitting a geometrical model to it that relies on adjustable parameters. Structurally complex radio sources with multiple extended emission are problematic for model fitting. The pitfall of the Fourier-plane model fitting technique is that it does not have a unique solution, and therefore it becomes crucial that one does not introduce more parameters in the model than are clearly needed by the visibility data.

An important application of model-fitting is that the fitted values from a model can also be used to quantify time evolution in the brightness distribution of a source. For example, which components have changed, and are the changes in component flux density, physical size of the source, and/or location (position angle); or we can compare the relative positions of components at different epochs in order to measure an apparent change (separation/motion and speeds of multiple components) in the structure of a radio source. Furthermore, alteration in source morphology can also be compared using two different geometrical models to see which of the two models is a better fit for a particular set of the visibility data (e.g., Taylor et al., 1999).

2.3.2 Least-Squares Fitting

For a discrete set of data points (which may be "noisy"), it is beneficial to *fit* a user-defined function or model with adjustable parameters through the data points in the aim of finding the set of parameters which can subsequently be used to determine how well the model fits the data and estimate an error range for each parameter. The fit is judged on the basis of the residuals or sum of the squared differences, i.e., Sum-of-Squares Residual (SSR) between the input data and the model function, evaluated at the same place. This quantity is often called chi-squared, χ^2.

Consider a model of the N data points or observed visibilities $\mathrm{V}_i(u, v)$, where $\mathrm{N} = 0, \ldots, \mathrm{N}-1$. The model which we require to fit is of the form, $\mathrm{F}(u, v)$ and depends on a number M of parameters, $\mathbf{a}_j$ where $j = 0, \ldots, \mathrm{M}-1$ (There can be different parameters such as flux density, position angle, length, and so on). There are two questions we can ask ourselves. Namely,

1. Given the data $\mathrm{V}_i(u, v)$, and adjustable parameters $\mathbf{a}_j$, we choose a set of $\mathbf{a}_j$. How good is a given choice of $\mathbf{a}_j$'s? In other words, what is the value of $\mathbf{a}_j$'s which best represent the data $\mathrm{V}_i(u, v)$ if we put $\mathbf{a}_j$ inside the "real function" or model $\mathrm{F}(u, v)$?

2. Given a "real" set of $\mathbf{a}_j$'s, what is the probability that the data passes through the curve given by the function $\mathrm{F}(u, v)$ with an error of $\pm\triangle\mathrm{V}$?

Keeping these two questions in mind, we can actually formulate a method of doing a fit, i.e., the *least-square fit*.

The purpose of the model is to reproduce the observations within their uncertainty, i.e.,

$$\mathrm{V}(u, v) = \mathrm{F}(u, v; a_1, \ldots, a_{\mathrm{M}-1}) + \text{noise} \tag{2.9}$$

If we assume that each data points V_i has a measurement error that is independently random and distributed as a *Gaussian distribution* around the "true" model $\mathrm{F}(u, v)$, and if we make another assumption that the data is a sample from a population having a true model with a given standard deviations, σ of these normal distributions are the same at all points. Then the probability $\mathrm{P}(\mathrm{V}_i)$ that our observations (measurements) V_i is within an interval of $\triangle\mathrm{V}$ around $\mathrm{P}(u, v)$ from the true model $\mathrm{F}(u, v)$ is given by:

$$\mathrm{P}(\mathrm{V}_i) = \exp\left[-\frac{1}{2}\left(\frac{\mathrm{V}_i - \mathrm{F}(u, v)}{\sigma}\right)^2\right]\triangle\mathrm{V}$$

For a sample of sufficiently large size, and knowing the population standard deviation, one can use the statistics of the chi-square distribution to describe a "goodness of fit" by looking at the variable χ^2. For example, given a set of N data points, the total probability that all the N points are an interval of $\pm\triangle\mathrm{V}$ around $\mathrm{P}(u, v)$ from the true model $\mathrm{F}(u_i, v_i)$ is given by the product:

$$\mathrm{P} \propto \prod_{i=0}^{\mathrm{N}-1}\left\{\exp\left[-\frac{1}{2}\left(\frac{\mathrm{V}_i - \mathrm{F}(u_i, v_i)}{\sigma}\right)^2\right]\triangle\mathrm{V}\right\} \tag{2.10}$$

When the model function $\mathrm{F}(u, v)$ have adjustable parameters, to find the most suitable values of $\mathbf{a}_j$'s for a given set of data points, Equation 2.10 must be maximised or the negative of its logarithm must be minimised, i.e.,

$$\max(\mathrm{P}) \approx -\min\left[\sum_{i=0}^{\mathrm{N}-1}\frac{\mathrm{V}_i - \mathrm{F}(u_i, v_i)}{2\sigma^2} - \mathrm{N}\log\triangle\mathrm{V}\right] \tag{2.11}$$

If each data point $\mathrm{V}_i(u, v)$ has its own known standard deviation σ_i, then we can modify the above equation by putting a subscript i on the symbol σ. Hence, the best estimate of $\mathbf{a}_j$'s is obtained

by minimising the quantity, *chi-square*:

$$\chi^2 = \sum_{i=0}^{\mathrm{N}-1} \left(\frac{\mathrm{V}_i - \mathrm{F}(u_i, v_i; a_1, \ldots a_{\mathrm{M}-1})}{\sigma_i} \right)^2 \tag{2.12}$$

The minimisation of χ^2 (SSR between the input data points and the function values) with respect to the function $\mathbf{a}_j$'s is called the *least-square fit*.

If the errors are Gaussian distributed, then near the minimum χ^2 follows the chi-square distribution with $\nu = \mathrm{N} - \mathrm{M}$ degree of freedom (DOF) (where N is the number of data points and M is the number of adjustable parameters in the fit). The SSR can be used to calculate the *variance* of the residuals, also known as *reduced chi-square* (SSR/DOF) or the *standard deviation* of the fit, sqrt(SSR/DOF), which is the *rms of the residuals*.

How do we know if this χ^2 is a good fit or not? In statistics, to describe a "goodness of fit", one could look at the variable, χ^2. For reduced χ^2 close to unity (DOF$\gg$ 1) is an indication that the sum of squared deviations between the fitted model function and the data points is the same and thus a good fit. A reduced χ^2 much larger than 1.0 indicate a bad fit, maybe due to incorrect data error estimates, data errors not normally distributed, systematic measurement errors or an incorrect model function. Similarly, a reduced χ^2 less than 1.0 indicates SSR is less than that expected for a random sample from the function with normally distributed errors. The data error estimates, for example, may be too large (errors σ_i have been overestimated).

2.3.3 Fitting Procedures in OMFIT

For model-fitting of complex visibilities, one can use the $\mathcal{AIPS}$'s OMFIT program, originally written by Ketan. M. Desai. The algorithm that attempts to minimise SSR is known as the *least-squares fitting*. The non-linear Least Square algorithm that the OMFIT program uses is the Levenberg-Marquart Method (Bevington & Robinson, 1992), whereby each step or iteration in the algorithm calculates the SSR with a new set of parameter values. The Marquardt-Levenberg algorithm selects the parameter values for the next iteration and the process continues until a preset criterion is met, either the fit has "converged" (i.e., the relative change in SSR is less than a certain limit), or it reaches a preset iteration count limit.

In OMFIT, the information of each iteration is displayed where one evaluate the progress of the fit. To repeat, the χ^2 is the sum of squared differences or SSR between the data and our fitted model divided by the number of degrees of freedom, which OMFIT is going to minimise.

However, our visibility data do not have well-known uncertainties but are related to the true ones by some scale factor K. So in OMFIT, the reduced χ^2 would be close to [K/visibility data_uncertainty], where K[6] is an unknown constant for our particular dataset, instead of [1/visibility data_uncertainty]. So the χ^2 and reduced χ^2 values that OMFIT reports will be off by a factor of K^2 compared to the statistical one (its "true" value). Since K is unknown, OMFIT does not use the absolute magnitude of χ^2 for any convergence criterion, it only compares the different values of χ^2 to find the lowest one. So to judge which of the two models represent a statistically good fit or not, in our analysis, we compare the relative value of their reduced χ^2 for that particular set of visibility measurements rather than the absolute value obtained from each model.

A word of caution here is that nonlinear fitting is not guaranteed to converge to the global minimum (the solution with the smallest sum of squared residuals, SSR), and one could find themselves stuck at a local minimum. The routine cannot determine whether a local minimum is reached and it is up to us, the user, to judge the convergence. The OMFIT program may, and often would lose track if SSR is large and changing slowly as the parameters are varied. To improve the chances of finding the global minimum, the starting values should be set in the vicinity of the solution, i.e., within an order of magnitude. The chance of stopping at another minimum can be lessened by choosing starting values closer to the solution. A reasonably good fit obviously, is no evidence there is not a better fit. Sometimes, it might be desirable to fit the model with alternative sets of starting values which cover a decent range for each parameter.

To recapitulate, in this thesis the Fourier-plane model-fitting technique is preferred as it allows some quantitative astronomical questions to be better addressed in the visibility domain than in the image plane. For instance, in comparing two images made at different epochs, it can be difficult to determine whether apparent changes in a source structure are due to real changes in the source, or just to differences in the u-v plane sampling and the imaging parameters. It is much more accurate and surest strategy to compare the measured visibilities directly.

[6]K is independent of which model we are fitting but the same for each visibility in a single data set.)

Summary of Chapter 2 - Radio Interferometry in a Nutshell:

1. This chapter dealt with the preliminaries for radio interferometry, where we limit our discussion to mostly non-imaging data analysis. Further details about the fundamentals of radio interferometry can be found in the textbook "Interferometry and Synthesis in Radio Astronomy" by Thompson et al. (2001).

2. We explained that a source brightness distribution, which is structurally simple enough at a given resolution can be accurately represented by a parametric model.

3. We also explained why model-fitting is the surest strategy to disentangle real changes in the structure of a source with small angular size (compared with the synthesised beam).

4. We described the least-square fitting technique which attempts to minimise the variations between the data and the model by fitting the parameters of the components to those of the actual visibilities.

5. A statistical overview of least-squares fitting where the goodness of a fit is quantified using the value of reduced χ^2 is described at length, and we also elaborated on the fitting procedures adopted for OMFIT.

'There are known knowns. These are things we know that we know. There are known unknowns. This is to say, there are things that we know we don't know. But there are also unknowns unknowns. There are things we don't know we don't know.'

– Donald Rumfeld

3

The Nuclear Region of the Galaxy M81

3.1 Introduction to the galaxy M81

The nearby spiral galaxy M81 (alias: NGC 3031, 0951+693) is situated at a distance of 3.96 ± 0.29 Mpc (Bartel et al., 2007) from Earth, and has the uniqueness of being the nearest spiral galaxy harbouring an AGN, with the only nearer AGN located in the elliptical galaxy Centaurus A (Israel, 1998 cited in Bietenholz et al., 2004). The proximity of the galaxy M81 to our Galaxy and its high declination (J2000.0 coordinates $\alpha = 09^{\mathrm{h}}55^{\mathrm{m}}33.173^{\mathrm{s}}$ and $\delta = 69^{\circ}3'55.062''$), also makes global VLBI observations of the low-power AGN at high spatial resolution feasible; in the frame of its host galaxy and at different epochs and frequency.

3.2 Characteristics of the galaxy M81

The Hubble Space Telescope (HST) spectroscopic observations imply a central mass of $7.0^{+2}_{-1} \times 10^7 M_\odot$ for the nuclear SMBH in M81 (Devereux et al., 2003). The weakly active central radio source in M81 emits in radio wavelengths with a compact structure and exhibits both low-ionisation nuclear emission-line region (LINER; Heckman, 1980) and Seyfert 1 characteristics. M81* thus appears closely related to the more distant and powerful AGN observed in quasars and radio galaxies. However, M81* is unusual both in that it occurs in a spiral rather than an elliptical galaxy, and in being relatively small and faint. The radio luminosity of M81* is around 100 mJy, i.e., on the order of $\sim 10^{37.5}$erg s^{-1} (e.g., see Ho et al., 1999), and it is thus classified as a LLAGN.

The explosion of the radio luminous supernova SN 1993J in M81, which happened around 28 March 1993 (Ripero & Garcia, 1993), triggered an intense campaign of VLBI observations using the most sensitive radio telescopes in the Northern Hemisphere to study the evolution of the supernova. Most of these VLBI observations of SN 1993J were phase-referenced to M81* and therefore a large number of VLBI observations of M81* were acquired as a byproduct. This enabled the determination of very accurate relative position between M81* and SN 1993J, where the latter is located $170''$ away towards the South-West in a spiral arm (see Figure 3.7) of the galaxy (Bartel et al., 2000b,a). Since the position of SN 1993J is not likely to be frequency dependent, one can turn the process around and essentially use SN 1993J as a phase-reference source to correctly align the images of M81*.

3.3 Observed Properties of M81*

The observed radio properties of M81* are enumerated as follows:

1. *Flux Variability*: M81* is one of the most extensively studied LLAGN in total flux. Its bright nuclear region ($\sim 70 - 400$ mJy) displays rapid and large amplitude intraday fluctuation (Ho et al., 1999; Sakamoto et al., 2001) and on the timescale of several weeks and years (Bietenholz et al., 2000; Martí-Vidal et al., 2011). The rapid variability, estimated from the analysis of its light curve, suggest that M81* is an extremely compact source.

2. *Intrinsic Size and Orientation*: Bietenholz et al. (2000) have shown that the apparent source

size of M81* is $\Theta \sim 0.5$ mas ($\sim$ 1800 AU) at 8.4 GHz, and follows a power-law with frequency ($\Theta \propto \nu^{-0.8\pm0.05}$) between 2.3 GHz and 22 GHz. Moreover, M81* is interpreted as consisting of a core-jet morphology with a weak extended emission to the North-East rotating with frequency (i.e., M81* is frequency dependent changing from $\sim 75^\circ$ at 2.3 GHz to $\sim 40^\circ$ at 22 GHz).

3. *Position of brightness peak*: According to Blandford & Konigl (1979), the jet in AGN observed on VLBI scales can be considered to be conical and the feature observed as the peak brightness is interpreted as the "photosphere" of the jet, within which the emission regions in the inner part of the jet, closest to the core is optically thick and outside which they are optically thin.

   The position of VLBI peak brightness, r_ν, where most of the emission comes from at a given observing frequency (ν_o), is seen at various distances from the SMBH (e.g., see schematic illustration 3.1). This frequency-dependent position of the peak brightness in AGN jet is described as $r_\nu \propto \nu^{-1/k}$, where k is a coefficient related to the magnetic field, particle density distribution, and the shape of the electron energy distribution. In M81*, the position of the radio brightness peak changes depending on observing frequency, moving towards the southwest (Bietenholz et al., 2004).

4. *Radio Spectrum*: Synchrotron self-absorption[1] (Konigl, 1981) results in spectra ($S \propto \nu^{+\alpha}$, where S is the flux density and ν the frequency) that are inverted up to a turnover frequency where the optical depth is high, $\tau_\nu = 1$. The radio spectrum of AGN generally consists of a flat or inverted spectrum (spectral index, $\alpha \gtrsim 0$) close to the central nuclear region. The flat overall spectrum comes from the blending of optically thin and thick parts of the jet. Farther out along the jet, the optical depth is low and the spectrum steep ($\alpha < 0$).

   At 8.4 GHz, M81* has a flat or slightly inverted synchrotron spectrum with a spectral index $\alpha = +0.3$ from a frequency of $\sim$ 1 GHz ($S \propto \nu^{+\alpha}$) up to a turnover frequency, $\nu_c = 200$ GHz (Reuter & Lesch, 1996). If due to synchrotron self-absorption in the jet, such a high turnover frequency, suggests a very dense plasma and a high magnetic field, and/or a rather flat energy distribution of the relativistic synchrotron-emitting particles (e.g., see §. 4.1. in Reuter & Lesch, 1996).

[1]Synchrotron self-absorption is referred to the appreciable absorption of the synchrotron radiation by the radiating electrons themselves; resulting in an optically thick radiation region.

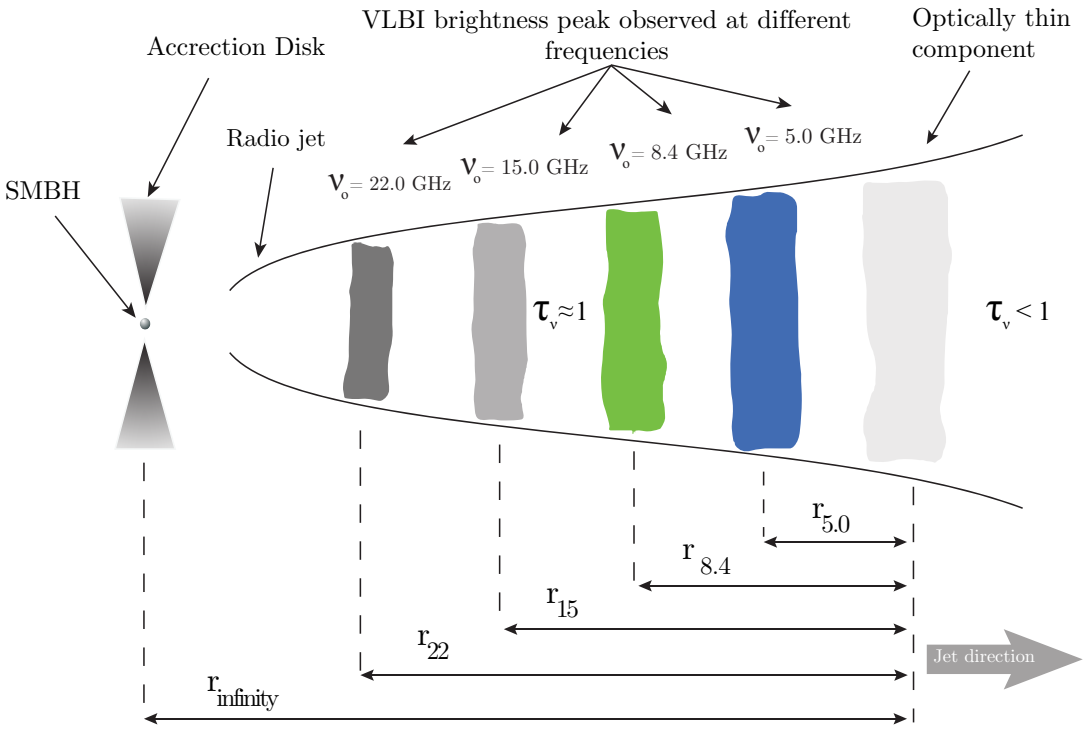

Figure 3.1: An illustration of Blandford & Konigl jet showing how the frequency-dependent position and size of the radio emitting region vary in an AGN jet. The coloured shadings show the emission region where the source size decreases with increasing frequency.

3.4 Observations and Data Reduction

As discussed in § 3.2, M81* was observed as a phase reference source for the continuing multi-frequency program of VLBI observations of SN 1993J (Bartel et al., 2002). A global array of between 11 and 18 radio telescopes (see Table 3.1, and Figure 3.4) participated in the observations with a total time of 12 – 18 hours for each run, yielding a dense *u-v* coverage, e.g., see Figure 3.4. Each telescope was equipped with a hydrogen maser as a time and frequency standard. High sensitivity VLBI observations were conducted using large aperture antennas and the MKIII or the MKIV VLBI data acquisition system was used with sampling rates of 128 or 256 Mbits s^{-1}. Moreover, the sources OQ 208 and 0954+658 were observed occasionally during each session as fringe finders and calibrator sources. In each session, data at the frequencies of 14.8, 8.4, 5.0, 2.3, and 1.7 GHz were recorded, with 8.4 and 5.0 GHz being the standard frequencies used in almost every session. In this thesis, we consider only the VLBI observations at 8.4 and 5.0 GHz, mostly

recorded with right circular polarisation (IEEE convention), and for later runs the left circular polarisation was also used (Bietenholz et al., 2000).

Table 3.1: 8.4 and 5.0 GHz VLBI Observations of M81★

Date (dd/mm/yy)	Antennas (Two-letter codes)	Total time (hrs)
(1)	(2)	(3)
	8.4 GHz	
26 Jun 93	BrFdHnKpLaMkNl PtSc	11.26
18 Sep 93	Mc RoAq YBrFdHnKpLaMkNlOvPtSc	06.73
16 Dec 93	EbMc AqGbYBrFdHnKpLaMkNlOvPtSc	17.70
28 Jan 94	Eb YBrFdHnKpLaMkNlOvPtSc	16.84
14 Mar 94	Eb NtGoRo GbYBrFdHnKpLaMkNlOvPtSc	05.66
21 Apr 94	Eb NtGoRo GbYBrFdHnKpLaMkNlOvPtSc	07.13
21 Jun 94	Eb NtGoRo GbYBrFdHnKpLaMkNlOvPtSc	07.10
29 Aug 94	Eb NtGoRo GbYBrFdHnKpLaMkNlOvPtSc	09.27
30 Oct 94	Nt RoAqGbYBrFdHnKpLaMkNlOvPtSc	09.04
23 Dec 94	Eb NtGoRoAqGbYBrFdHnKpLaMkNlOvPtSc	15.93
12 Feb 95	EbMcNtGoRoAqGbYBrFdHnKpLaMkNlOvPtSc	11.30
17 Aug 95	Eb YBrFdHnKpLaMkNlOvPtSc	10.27
18 Dec 95	Ro YBrFdHnKpLaMkNlOvPtSc	15.53
07 Apr 96	GoRo Y FdHnKpLaMkNlOvPtSc	15.89
31 Aug 96	Eb YBrFdHnKpLaMkNlOvPtSc	08.02
13 Dec 96	Eb YBrFdHnKpLaMkNlOvPtSc	16.89
06 Jun 97	Eb GbYBrFdHnKpLaMkNlOvPtSc	10.78
14 Nov 97	EbMcNtGoRo GbYBrFdHnKpLaMkNlOvPtSc	10.66
02 Jun 98	EbMc Ro YBrFdHnKpLaMkNlOvPtSc	13.35
07 Dec 98	EbMcNtGoRo YBrFdHn LaMkNlOvPtSc	11.65
24 Feb 00	EbMcNtGoRoAqGbYBrFdHnKpLaMkNlOvPtSc	14.69
12 Nov 00	EbMcNtGoRoAqGbYBrFdHnKpLaMkNlOvPtSc	11.75
	5.0 GHz	
26 Jun 93	BrFdHnKpLaMkNl PtSc	14.59
14 Mar 94	Mc YBrFdHnKpLaMkNlOvPtSc	06.33
21 Jun 94	Mc YBrFdHnKpLaMkNlOvPtSc	06.64
29 Aug 94	Mc YBrFdHnKpLaMkNlOv Sc	09.28
31 Oct 94	YBrFdHnKpLaMkNlOvPtSc	14.30
23 Dec 94	Mc YBrFdHnKpLaMkNlOvPtSc	15.37
10 May 95	Eb YBrFdHnKpLaMkNlOvPtSc	06.92
18 Dec 95	Ro YBrFdHnKpLaMkNlOvPtSc	14.55

07 Apr 96	GoRo	Y FdHnKpLaMkNlOvPtSc	13.43
31 Aug 96	Eb	YBrFdHnKpLaMkNlOvPtSc	06.33
13 Dec 96	Eb	YBrFdHnKpLaMkNlOvPtSc	16.92
14 Nov 97	EbMcNtGoRo	GbYBrFdHnKpLaMkNlOvPtSc	07.51
20 Nov 98	EbMcNtGoRo	GbYBrFdHnKpLaMkNlOvPtSc	10.69
16 Jun 99	EbMcNt	GbYBrFdHnKpLaMkNlOvPtScWb	07.96
23 Nov 99	EbMcNt	YBrFdHnKpLaMk OvPt WbOnJb	11.85
09 Jun 01	EbMcNt	YBrFdHnKpLaMkNlOvPtSc OnJb	11.80
24 May 02	EbMc	YBrFdHnKpLaMkNlOvPtScWbOn	11.74

The description of the columns of above table is given as follows. Columns:

(1): The dates of the observing run.

(2): Ground radio telescopes (see Figure 3.4) and the two-letter codes. This list also consists of the location and diameter of the antennas: Eb = 100m, MPIfR, Effelsberg, Germany; Mc = 32m, IdR-CNR, Medicina, Italy; Nt = 32m, IdR-CNR, Noto, Italy; Go = 70m, NASA-JPL, Goldstone, CA, USA; Ro = 70m, NASA-JPL, Robledo, Spain; Aq = 46m, CRESTech/York Univ. and Geomatics/NRCan, Algonquin Park, Ontario, Canada; Gb = 43m, NRAO, Green Bank, WV, USA; Y = phased VLA; equivalent diameter 130m, NRAO, near Socorro, NM, USA; Br = 25m, NRAO, Brewster, WA, USA; Fd = 25m, NRAO, Fort Davis, TX, USA; Hn = 25m, NRAO, Hancock, NH, USA; Kp = 25m, NRAO, Kitt Peak, AZ, USA; La = 25m, NRAO, Los Alamos, NM, USA; Mk = 25m, NRAO, Mauna Kea, HI, USA; Nl = 25m, NRAO, North Liberty, IA, USA; Ov = 25m, NRAO, Owens Valley, CA, USA; Pt = 25m, NRAO, Pie Town, NM, USA; Sc = 25m, NRAO, St. Croix, Virgin Islands, USA, Wb = 12 × 25m, Westerbork, Netherlands; On = 25m, Onsala, Sweden; JB = 26m, Jodrell, UK.

(3) : Sum over all the baselines of the number of hours spent on M81* after data calibration and editing.

The phased VLA was used in all of these VLBI observations, and the interferometric data resulted in accurate flux measurements at 8.4 GHz of M81* and SN 1993J. Both senses of circular polarisation were recorded with a bandwidth of 50 MHz per polarisation. The VLBI data were correlated using the Very Large Baseline Array (VLBA) processor in Socorro, New Mexico, U.S.A. The data reduction, i.e., initial calibration, editing, and fringe-fitting, was performed by Bietenholz et al. (2000) using the NRAO's software package, $\mathcal{AIPS}$.

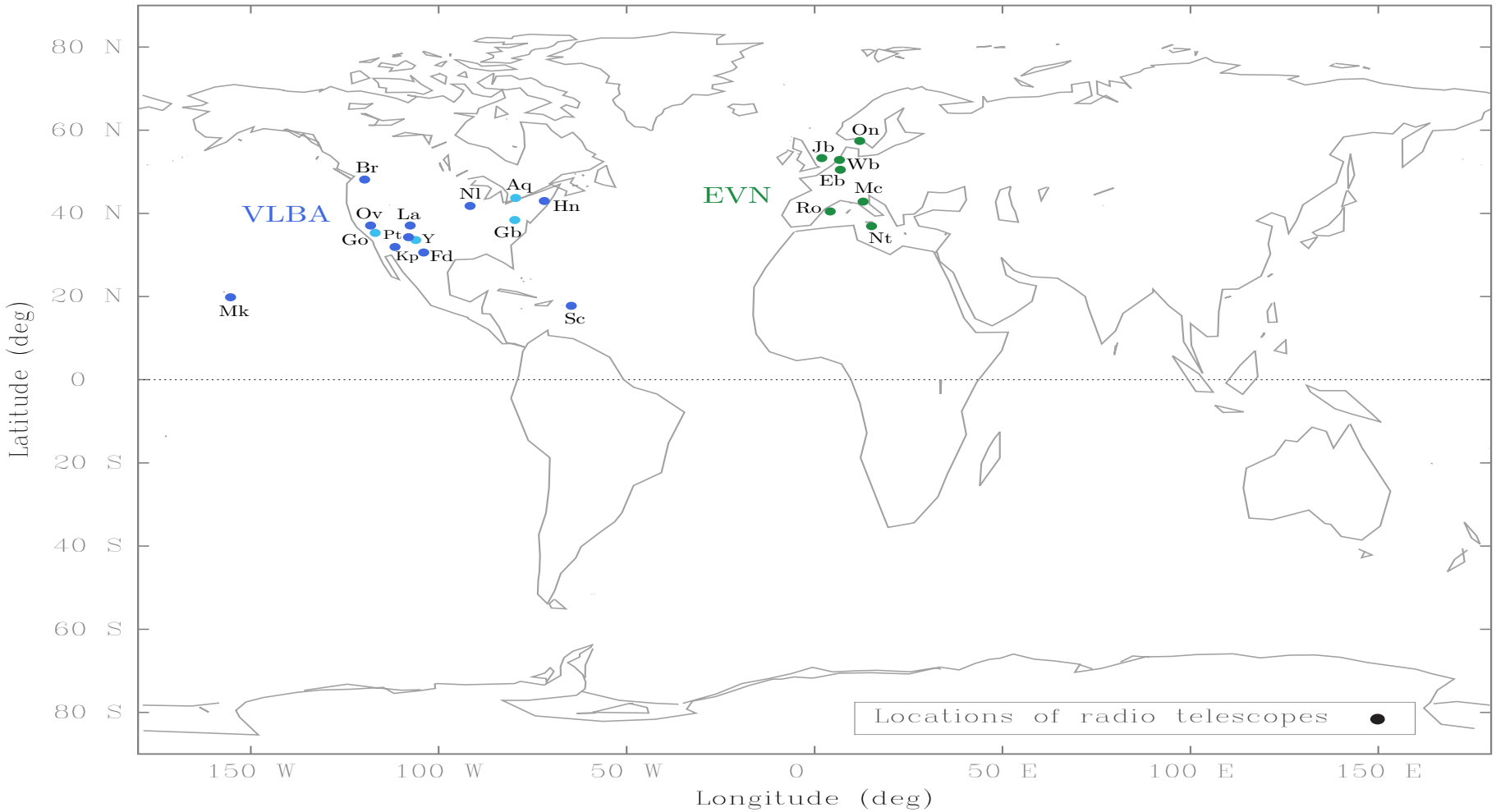

Figure 3.2: The filled circles show the toponym - derived from the Global Positioning System (GPS) locations - of the radio telescopes around the globe which participated in our VLBI observation of M81* from 1993 to May 2002. The Very Long Baseline Array (VLBA), and other stations including the VLA in phased-array mode are shown in blue and pale blue respectively. The stations of the European VLBI Network (EVN) are shown in green.

Our most extensive data sets available consist of 39 epochs of observations, observed at both 5.0 GHz (17 data sets), and 8.4 GHz (22 data sets), spanning between 1993 and 2003. A wider range in frequency would have been better, but all the other frequencies have much poorer sampling compared to the those at 8.4 and 5.0 GHz, which can be useful to look for correlation (or lack thereof) between that two range of frequencies. Figure 3.3 shows the time distribution of all the epochs used in our analysis; green squares indicate the 8.4 GHz data sets and blue squares indicate the 5.0 GHz data sets.

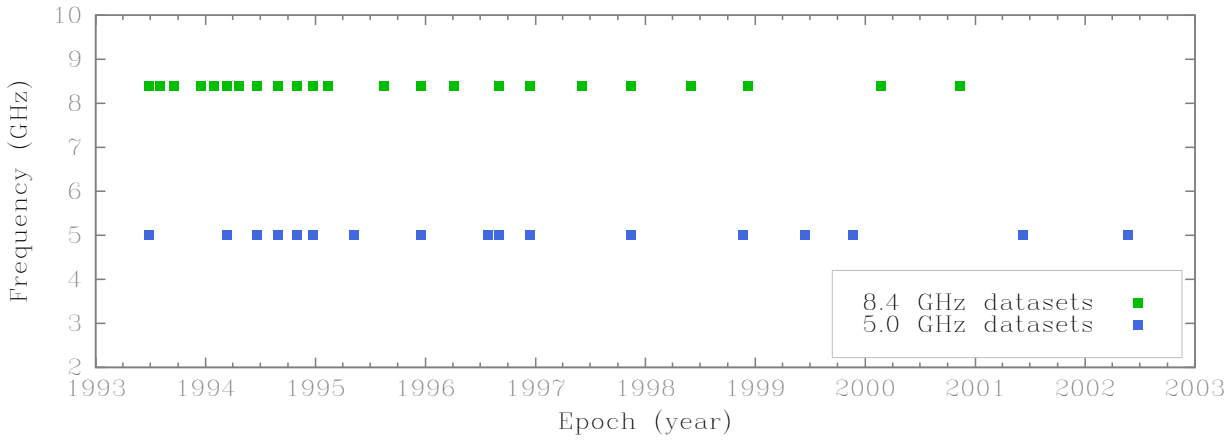

Figure 3.3: Time Sampling of our VLBI monitoring. The squares indicate our datasets at 8.4 GHz and 5.0 GHz respectively.

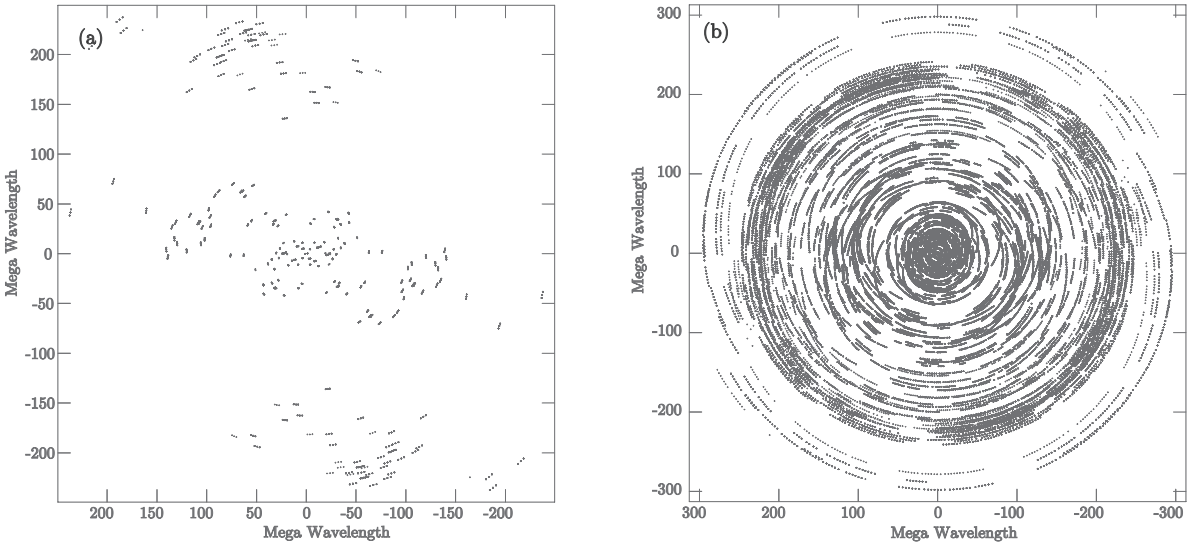

Figure 3.4: (a) is a snapshot (20 mins) and (b) is a full (11.75 hrs) experiment of the u-v plane coverage of M81* at 8.4 GHz that was observed on November 12, 2000. The plots show the density and nearly circular u-v coverage and the spatial frequencies to which the observation is sensitive. Both u and v are given in Mega-wavelengths.

Next, we inspect one of our continuum VLBI data. Consider the data of VLBI observation of November 12, 2000, in which our source M81* was observed at 8.4 GHz. Our data has already been fringe-fitted and amplitude calibrated. Some of the most useful two-dimensional plots of our visibility dataset are shown in the following Figures. A plot of the u-v plane coverage (Figure 3.4), shows the spatial frequencies to which the observation is sensitive.

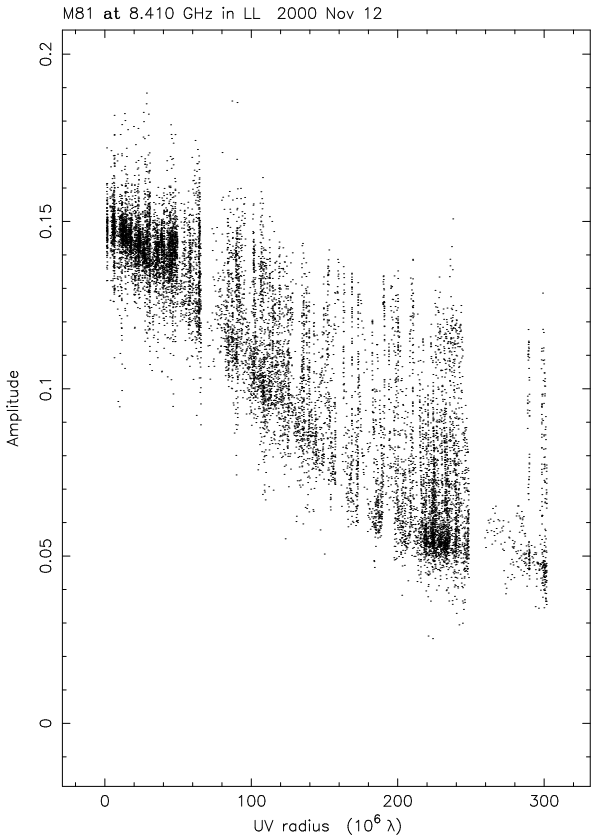

Figure 3.5: A plot of visibility amplitude as a function of radius in the u-v plane (projected baseline).

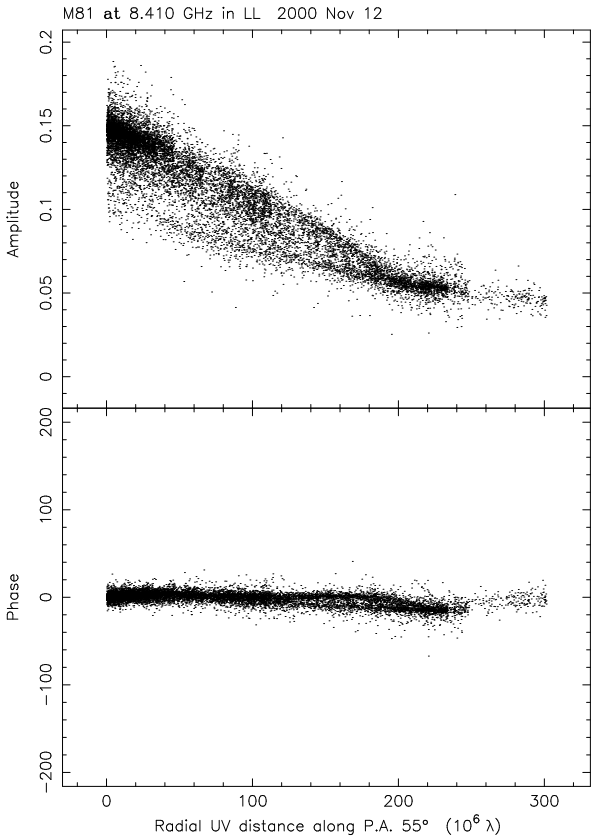

Figure 3.6: The plot of amplitude and phase as functions of the component of baseline length projected in position angle 55°.

Figure 3.5 shows the visibility signature of M81*, where the source is extended and not dominated by a point source component which would have a constant amplitude; the correlated flux density decreases with baseline length since the longer baselines sample the smaller-scale structure. Figure 3.6 is a cut of amplitude and phase along the radial line of the u-v plane corresponding to a position angle of $\sim 55^\circ$ (measured North of East) along the image plane; which is the mean position angle of the orientation of the jet in M81* as we shall see in Chapter 5 § 5.2.1. The bottom panel of Figure 3.6 shows that the distribution of visibilities is mostly concentrated at the visibility phase = 0.

3.4.1 Images of M81 and M81*

Figure 3.7 shows a multi-wavelength image of the galaxy M81. The two brightest sources in the optical image are indicated in green radio contours - M81* is located at the centre of the galaxy and the supernovae SN 1993J is located at the southwest of M81*; the sources are separated by $\sim$ 2.8 arcmins. The inset depicts our VLBI image of M81* at 4.8 GHz taken on 24th of February 2000, revealing a compact asymmetric source with an elongated structure which can be traced out to $\sim$ 1 mas (which translates to $\sim$ 0.016 pc) to the northeast. We produced a VLBI time-lapse animated movie[2] showing the evolution of M81* at 8.4 GHz from 1993 to 2000.

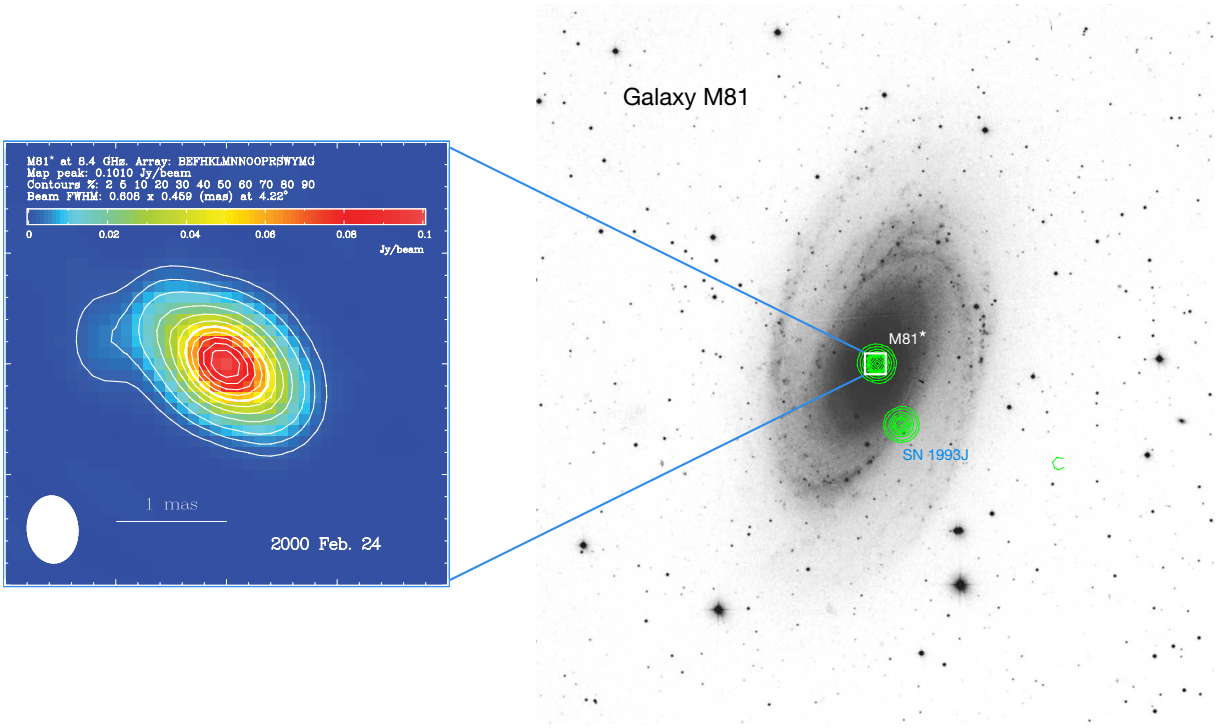

Figure 3.7: Figure 3.7 shows an optical image of the spiral galaxy M81 observed with the Palomar 48-inch Schmidt Telescope (Sandage & Bedke, 1994) that we overlaid with radio contours (left-hand) from NRAO/VLA Sky Survey (Condon et al., 1998). The (*green*) contours show the radio emissions, the source in the centre of the galaxy being M81* and the southwest one being SN 1993J; the contour levels are at 5, 10, 20, 30, 40, **50** (heavy contour), 60, 70, 80, and 90% of the peak brightness, which was 81.4 mJy beam^{-1}. The inset shows our VLBI image of M81* at 8.4 GHz on 24th of February 2000. The FWHM size of the restoring beam is indicated at lower left which is 0.608 $\times$ 0.459 mas FWHM at 4.22°. The contours drawn are at 2, 5, 10, 20, 30, 40, **50** (heavy contour), 60, 70, 80, and 90% of the peak brightness, which was 101.0 mJy beam^{-1}. North is up and East is to the left.

[2]http://tinyurl.com/Arvind-Ramessur-Thesis-2017

The Figures 3.8 and 3.9 show two more representative images of M81* taken at two different epochs (12 Nov. 2000 and 23 Nov. 1999 at frequencies of 8.4 and 5.0 GHz respectively). At each frequency, M81* is only marginally resolved and has a simple brightness distribution, elongated approximately in the southwest to northeast direction. From a visual inspection, a slightly asymmetric compact structure is visible and being somewhat more extended to the northeast, consistent with earlier findings in Bietenholz et al. (2000). The structure of M81* observed on 12 Nov. 2000 points towards what seems to be a relatively weak blob[3] which is located roughly along the rotation axis of the galaxy. At 5.0 GHz, slight changes in the structure are visible, and no subcomponents are identifiable (also see Figure 5.3). The effective size (extent of the emission to the North-East is roughly proportional to $\nu^{-0.8}$ as discussed in § 3.3), and orientation vary with frequency, with both the size and position angle, p.a. (North through east), decreasing with increasing frequency.

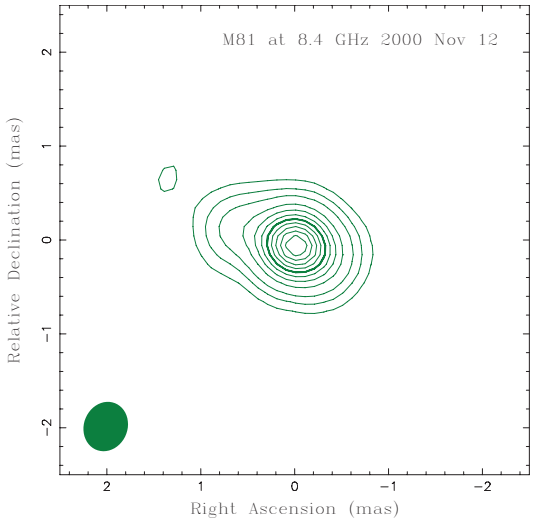

Figure 3.8: The image of M81* at 8.4 GHz showing a very compact source with a weak extension. The image has a restoring beam of 0.535×0.465 mas FWHM at $-21.6°$. The contours are at 2, 5, 10, 20, 30, 40, **50** (heavy contour), 60, 70, 80, 90% of the peak flux density of 89.3 mJy beam^{-1}.

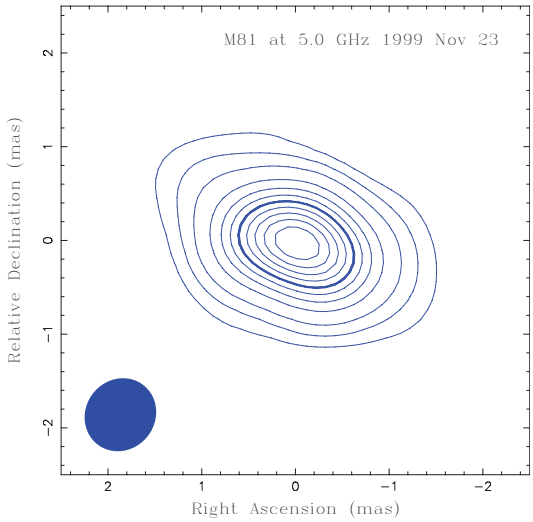

Figure 3.9: The image of M81* at 5.0 GHz showing slight changes to the compactness of the source. The image has a restoring beam of 0.801×0.742 mas FWHM at $-37.4°$. The contours are at 2, 5, 10, 20, 30, 40, **50** (heavy contour), 60, 70, 80, 90% of the peak flux density of 93.7 mJy beam^{-1}.

[3]The blob seems to be an ejection of a new jet component, which could be preceded to a flare in M81*, peaking on Nov. 1998; See Figure 5.1. However, further investigation would be required and the ejection can only be considered suggestive, not reliable.

3.5 Problem Statement

3.5.1 The Observer: Limits of Resolution

Even though the frequency and the size of the Earth ($\sim$ 12 742 km) set a limit to the angular resolution that can be achieved by ground-based VLBI observations, space-deployable antennas are also possible. The Space-VLBI (VLBI-Space Observing Programme–VSOP) and RadioAstron[4] represent a logical step in the evolution of radio interferometry and has played an important role in AGN research as it has the potential to provide the highest angular resolution images of any observation technique.

The Japanese HALCA satellite of VSOP project was placed in an orbit with an apogee height above the Earth's surface of 21 400 km. Observations at 1.6 and 5.0 GHz of HALCA's 8 m radio telescope, and simultaneous ground-based radio telescope can synthesise an aperture over twice the size of the Earth, providing a maximum angular resolution of $\sim$ 0.6 mas (Hirabayashi et al., 1998). In the case of Space-VLBI observations of AGN, the angular resolution is usually sufficient to resolve the two-dimensional jet transverse to its flow and individual features can be recognised at significantly smaller separations from its central component, e.g., Gabuzda & Gómez (2001). However, in the case of M81*, even from Space-VLBI observations at 5 GHz, the emitting structure could not be completely resolved (Bartel & Bietenholz, 2000).

When the angular size of a source is small (compared with the synthesised beam) and/or the observations have low signal-to-noise ratio, quantitative measurements of the physical parameters, in particular, the length and orientation of the AGN jet, model-fitting on the visibilities is preferred. In model-fitting, the component sizes and positions can be determined with an accuracy smaller than the resolution. Bietenholz et al. (1996, 2000, 2004) demonstrated that a robust way to investigate the structural variability of M81* is to model the visibility data directly in the u-v plane. They used a two-component model fit, i.e., an elliptical Gaussian to model the emission of the central part and a point source to model the weak jet extension.

In addition, for high precision astrometry, a reliable estimation of the position of the SMBH in the inner-most area of AGN, close to the jet-launching region is required. This is observationally

[4] http://www.asc.rssi.ru/radioastron/

difficult. High-frequency VLBI observations[5] with high angular resolution are able to access this region due to the opacity effect. (Bietenholz et al., 2000) have estimated the location of the core in M81* using astrometry at 8.4 GHz and the most stable point was found to be located at 0.6 ± 0.3 FWHM from the centre of the Gaussian model, towards the southwest. That location was subsequently confirmed by using multi-frequency relative astrometry, referenced to the shell centre of SN 1993J Bietenholz et al. (2004).

3.5.2 The Observed: Sidedness in AGN

Although kpc and Mpc scales extragalactic radio sources display two-sided large scale structures, one of the intriguing characteristics of pc-scale jets imaged with VLBI resolution is that they appear overwhelmingly one-sided (Bridle & Perley, 1984; Parma et al., 1987; Zensus, 1997; Xu et al., 2000). In fact, 94% of the 135 AGN observed between 1994 and 2007 in the MOJAVE[6] sample (only 5 seem to have two-sided jets on the pc-scale) have apparent one-sided jet morphologies, where the jet typically extends for a few mas on one side of the bright central component (e.g., Lister et al., 2009a,b). In some cases, the counter-jet is unseen on mas-scales when observed with VLBI.

Two main reasons (not necessarily mutually exclusive) that could account for the apparent single-sidedness or asymmetry in AGN at VLBI scales are:

1. *Circumnuclear obscuration*: The asymmetric appearance of jet at pc-scale could be due to the stronger free-free absorption toward the counter-jets owing to an obscuring ionised gas (distributed in the tori/wraped discs) intervening along our line of sight (Walker et al., 2000; Jones et al., 2001). For instance, the inner edge of the torus is expected to be ionised by the intense radiation field from the central source. At a distance of the inner edge, likely between $0.3-1$ pc from the AGN, a region of depth ~ 0.1 pc is fully ionised at a temperature of $\sim 10^4$ K and density few $\times 10^4$ cm^{-3} (Morganti, 2002). Such an ionised gas will radiate thermal emission and will cause free-free absorption of nuclear radio components viewed

[5] At high frequencies, the change in position of the brightness peak will be much less than that at low frequencies (e.g., $\propto \nu^{-1}$).

[6] Monitoring Of Jets in Active galactic nuclei with VLBA Experiments (MOJAVE) program is a multi-epoch 15 GHz survey aimed at monitoring relativistic motion in AGN jet on parsec-scales in the northern sky.

through the torus. Therefore, supporting the presence of free-free absorption towards the jet-counter is the absence of those jet-counterpart in a number of observed Seyfert galaxies down to the scale of $\sim$ 1 pc that nevertheless show symmetric radio emission on the larger scale (e.g., Wilson et al., 1998; Ulvestad et al., 1999).

2. *Relativistic beaming*: The jets have intrinsically similar emissivity, but the asymmetry observed may be indicative of relativistic Doppler or beaming effect which enhances the surface brightness of the jet that is closer to the line of sight, leaving a reduced visibility of the receding jet as it is beamed away from Earth. The detection of superluminal motion (Rees, 1966) in radio galaxies and quasars (e.g., Zensus, J. A. and Pearson, T. J., 1988; Unwin et al., 1989; Cotton et al., 1999) shows that small-scale jets are relativistic and strongly beamed in many cases. Additional support of the Doppler favouritism is the statistical evidence that the brighter jet points towards the observer (Laing, 1988). Therefore, if the jet is slightly asymmetric then relativistic beaming will still give an apparent one-sided jet.

   If we consider the simplest case of an optically thin spherical blob moving towards the observer at an angle θ to the line of sight, the apparent flux density $S_{obs}(\nu)$ of the blob is given by:

$$S_{obs}(\nu) = S_{rest}(\nu)\,\delta^{3-\alpha}, \tag{3.1}$$

   where the blob has a power-law spectrum, $S_\nu \propto \nu^{-\alpha}$, and rest-frame flux density $S_{rest}(\nu)$. δ is the Doppler enhancement factor:

$$\delta = \gamma^{-1}\left(1 - \beta cos\theta\right)^{-1}, \tag{3.2}$$

   where γ is the Lorentz factor and β is the bulk velocity of the blob relative to the speed of light, c.

   The predicted ratio of the apparent flux densities of the jet and counter-jet (i.e., the ratio between the approaching and receding jet, J) can be expressed in terms of α and β:

$$J = \left(\frac{1 + \beta cos\theta}{1 - \beta cos\theta}\right)^{p}, \tag{3.3}$$

   where, $p = 3 - \alpha$ (e.g., Urry & Padovani, 1995). Substituting moderate values of $\beta = 0.95$, $\theta = 10^\circ$, and $\alpha = 0.7$ yield a resulting jet to counter-jet ratio of 10^4. Obviously, the jet is significantly brighter than the counter-jet even for a mildly relativistic jet. This example strengthens the notion why observed radio sources at mas scales are most likely to show one-sided jet.

In this thesis, we confine our attention to the observations of M81* at the smallest scales. Owing to the small angular size of M81*, a resolution limit is imposed by our instrument (see preceding text § 3.5) preventing us from obtaining a good estimate of the inclination of the central accretion disc and jet system (i.e., it is pole-on viewed or not is still uncertain). Consequently, the source symmetry or a jet/counter-jet ratio (J) of M81* is difficult to determine.

The fits to all the 5.0 and 8.4 GHz observations (owing to extensive datasets at those frequencies) from 1993 to 2003 shown in Figure 3.3 could provide us with a more comprehensive picture of the structure and evolution of the jet. There is evidence of jet propagation for both short (< 1 month) and longer (1 to 2 years) timescales as the jet in M81* expands (Bietenholz et al., 2000). With 10 years of observations from the global VLBI array, we need an improved geometrical model (preferably one-sided) to further explore the evolving jet in M81* and expose its nature.

Summary of Chapter 3 - The Nuclear Region of the galaxy M81:

1. In the course of this chapter, we reviewed the different characteristics and properties of the nuclear region of M81 (dubbed M81*), which is the main character of this thesis.

2. We described the 10 years of our archival data sets of 5.0 GHz (17 data sets), and 8.4 GHz (22 data sets) for the observations of M81*, and its data reduction. We also include representative images of M81* which is shown to be a compact source with a weak protrusion (interpreted as a jet of the order of ~ 1 mas in length at 8.4 GHz) along the northwest-southwest axis.

3. We produced a VLBI time-lapse animated movie of M81* showing the evolution at 8.4 GHz spanning the period 1993 to 2000.

4. We called our readers attention on the primary concerns that we face to unravel the nature, and in studying the evolving jet in M81* probed at VLBI (including space-VLBI) scales due to its angular size.

5. In closing, we gave an overview of the relativistic effects such as Doppler beaming/boosting effect that is thought to explain the one-sidedness in AGN observed at VLBI scales. We then emphasised that a new model which is strictly one-sided is necessary to track the evolution of jet component in M81*.

'The Universe is full of magical things, patiently waiting for our wits to grow sharper.'

– Eden Phillpotts

4

Fourier-Plane Modelling

4.1 Point Source(s) - DOT Model

Common geometrical models which represent an assumed form of the sky brightness distributions are point sources and Gaussians. Point sources or delta-function components are mostly used to characterise unresolved sources. A point source can be mathematically described by a Dirac delta or δ-function. When located at some offset on the sky from the phase centre, denoted as (a, b), the complex visibility has non-zero phases. The expected normalised visibility is one, as shown in Equation 4.3.

In one-dimension, for an integrable function $f(x)$:

$$\begin{aligned}\int_{-\infty}^{+\infty} \delta(x) f(x) dx &= \int_{-\infty}^{+\infty} f(0)\delta(x) dx \\ &= f(0) \int_{-\infty}^{+\infty} \delta(x) dx \\ &= f(0) \times 1 \\ &= f(0),\end{aligned} \tag{4.1}$$

which is the definition of the δ-function. This implies that the integral of any function multiplied by a δ-function located about zero is just the value of the function at zero. This concept can be extended to give the *Shifting Theorem*, again for a function $f(x)$, yielding:

$$\int_{-\infty}^{+\infty} \delta(x-a) f(x) dx = f(a),$$

where $\delta(x-a)$ is just a δ-function located at $x = a$ as shown in Figure 4.1.

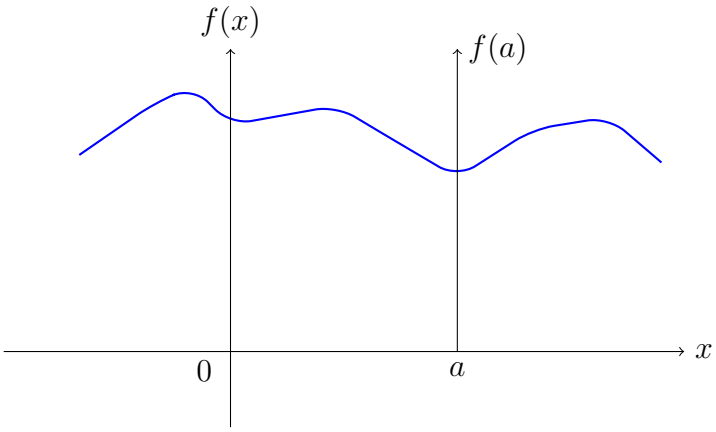

Figure 4.1: Shifting property of the δ-function.

In two-dimensions, for a function $f(x, y)$, we have:

$$\int\int \delta(x-a, y-b) f(x, y) dx dy = f(a, b), \tag{4.2}$$

where $\delta(x-a, y-b)$ is a δ-function located at position a, b. The Fourier transform of a δ-function can be formed by direct integration of the definition of the Fourier transform, and the Shift property in Equation 4.1.

$$\mathfrak{F}\left\{\delta(x)\right\} = \int_{-\infty}^{+\infty} \delta(x) \exp(-2j\pi ux) dx = \exp(0) = 1, \tag{4.3}$$

and then by the *Shifting Theorem*, Equation 4.2, yielding:

$$\mathfrak{F}_x\left\{\delta(x-a)\right\}(u) = \int_{-\infty}^{+\infty} \delta(x-a) e^{-j2\pi ux} dx = \exp(-2j\pi ua) \tag{4.4}$$

so that the Fourier transform of a shifted δ-function is given by a phase ramp. The modulus squared of Equation 4.4 is:

$$|\mathfrak{F}\{\delta(x-a)\}|^2 = |\exp(-2\pi jua)|^2 = 1, \tag{4.5}$$

implying that the power spectrum of a δ-function is a constant, independent of its location in real space.

In principle, the brightness distribution of a point source model is:

$$\mathrm{I}(x,y) = \delta(x-a, y-b),$$

and its corresponding visibility in the two-dimensional Fourier transform is given as:

$$\boxed{\mathrm{V}(u,v) = \exp -2\pi j(ua+vb)}, \tag{4.6}$$

where the amplitude of the visibility is one. Unlike the visibility amplitude, the phase is linearly dependent on the baseline. In the particular case where the AGN is at the pointing centre, the phase will be zero. The interest of observing a point-like source (i.e., an AGN with sufficiently small angular diameter), the measured visibility allows access to the instrumental visibility function.

4.2 Elliptical Gaussian - GAUS Model

The parametrisation of most source geometry (both symmetric and asymmetric) are elliptical Gaussians Elliptical Gaussian Model (GAUS). The Gaussian model owes its success to its easy-to-compute Fourier transform; the Fourier transform of a Gaussian is also a Gaussian. Gaussians are used for accurate measurements of source parameters such as peak flux density, central position, and angular size. In general, the equation for a two-dimensional elliptical Gaussian is given as follows:

$$\mathrm{G}(x,y) = \mathrm{A}\exp\left[-\frac{(x-x_0)^2}{2\sigma_x^2} - \frac{\beta\,(x-x_0)\,(y-y_0)}{\sigma_x\sigma_y} - \frac{(y-y_0)^2}{2\sigma_y^2}\right], \tag{4.7}$$

where A is the peak amplitude, (x_0, y_0) is the central position, σ_x and σ_y are the rms lengths of the major and minor axes, respectively, and the dimensionless parameter β is a measure of the p.a. difference between the principal axes of the ellipse and the coordinate axes (x, y).

The Fourier transform of an elliptical Gaussian yield an elliptical Gaussian with only six free parameters (R.A. & Decl., major axis Full Width at Half Maximum (FWHM), minor axis FWHM, p.a., and peak brightness). However, the elliptical Gaussian is symmetric. In view of the fact that the jet in M81* is asymmetric (see Chapter 3), developing a more sophisticated model which incorporates the asymmetry with a minimal number of parameters can be useful to extract physically interesting information from its VLBI observations.

The way to proceed is to develop a new (and improved) model and an algorithm that attempts to minimise the variations between the data and the model by fitting the parameters of the component to those of the actual visibilities. As discussed in the course of the preceding Chapter 2, this is done using the least-squares fit, and the goodness of fit is quantified using the value of reduced χ^2 (the sum of the squared differences between model and data divided by the number of degrees of freedom). The algorithm will run for a set number of iterations defined by the user, specifying the χ^2 each time; which is the best way of digging out information at or below the resolution limit.

4.3 Point Source Approximation of an Asymmetric Triangle (ASYM) Model

An asymmetrical triangle model with a fixed length parameter may be useful to capture the characteristics features of a radio source structure, and possibly provide an improvements over simple symmetrical models such as the circular or elliptical Gaussian model used for the nuclear region of galaxy M81 and other similar radio sources.

However, the basic properties of the jet in M81* as projected onto the sky plane are probably:

(i) Extended along the jet, but likely unresolved transversely (the jet emission is concentrated along a line on the sky),

(ii) One end of the surface brightness of the jet is higher than the other, and

(iii) The jet is not straight.

Therefore, to make an asymmetric model much more generalisable, rather than developing an exact asymmetrical triangle model, we come forth with an approximate form. In other words, since any

continuous distribution of brightness can be thought of as a collection of point sources, we made use of a collection of point sources to approximate a continuous triangular shape of an asymmetrical triangle, dubbed Point-Source Approximation of an Asymmetric Triangle Model (ASYM). A schematic diagram of the ASYM model is shown in Figure 4.2.

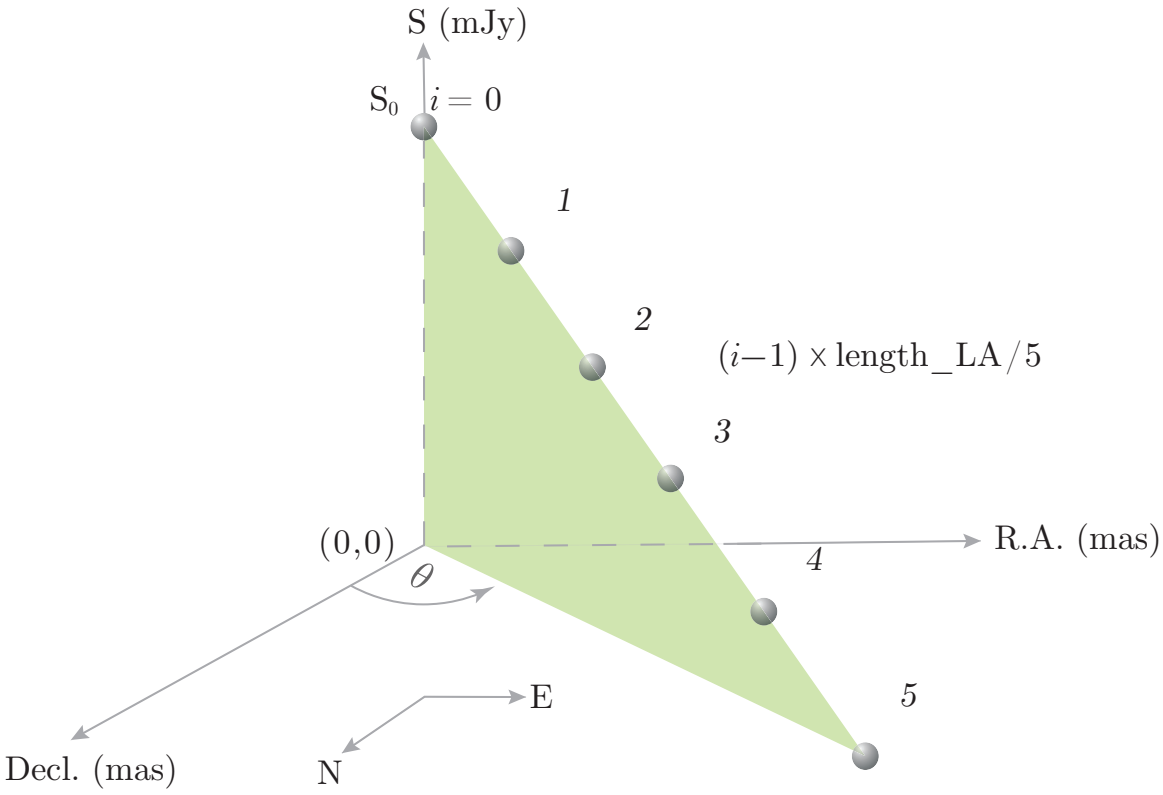

Figure 4.2: Schematic diagram of an asymmetric triangle model approximated to a collection of point sources (ranging from $i = 0$ to $N - 1$, where $i = 0$ is the central point source, also taken as the nominal position of the model. For the sake of simplicity, the schematic diagram illustrates only 6 point sources. Point sources, $i = 1$ to 5 are at $(i - 1) \times$ length_LA/5.

It should be noted that model-fitting programs which can fit point sources are readily available - those that can fit multiple point sources. Why should we develop a new model where one can use, say 6 "DOT" models as a point source approximation for a marginally resolved source? Unlike the usual case of multiple point sources, the parameters of each point source (x, y, and flux-density) are not free and independent[1] but would be rather functionally related. A point-source approximation lends itself easily to distributions along a line and should be relatively easy to generalise to non-linear slopes in flux density. The approximation becomes more accurate the

[1]Using, for instance, 6 "DOT" models would yield 18 parameters, whereby increasing the degrees of freedom, and consequently, it could lead to an over-interpretation of the visibility data.

larger the number of point sources ($n_{\rm pt}$), but this can, of course, make the computations longer.

However, since we only need this approach for sources that are not well resolved, a relatively small number of point sources should be sufficient. The strategy employed to derive the visibility function and its derivatives for the

For a point source of flux density S, the visibility function is denoted as:

$$\boxed{\mathrm{V}(u,v) = \mathrm{S}e^{j2\pi(ux+vy)}} \tag{4.8}$$

For an n^{th} point source in our point-source approximation of the asymmetrical triangle model, we use i as index going from 0 to $(n_{pt}-1)$.

Then for the i^{th} point source:

$$\mathrm{S}_i = \frac{\mathrm{S}_{Tot}}{\frac{(n+1)}{2}} \frac{(n-i)}{n}$$
$$x_i = \mathrm{LA}\frac{i}{n}\sin\theta$$
$$y_i = \mathrm{LA}\frac{i}{n}\cos\theta$$

The model visibility for the i^{th} point source is V_i:

$$\mathrm{V}_i = \frac{\mathrm{S}_{\rm Tot}}{\frac{(n+1)}{2}} \frac{(n-i)}{n} e^{j2\pi(ux_i+vy_i)} \tag{4.9}$$

In our point source approximation of an asymmetric triangle model, the parameters are described as follows:
S: flux density, where $\mathrm{S}_{\rm Tot}$ is the total brightness (mJy) of all the components (S_0 to S_{n-1}),
LA: the length (mas) of the hypotenuse of the "triangle",
θ: the position angle (degrees) of the components, measured from north through east.
x and y: the offset positions (mas) of the components relative to the observing centre, and the brightest point source is at sky position, $x = y = 0$ (i.e., x_0, y_0),
n: the number of components (point sources).

The derivatives of the model visibility with respect to the model parameters are:

(i) V_i with respect to $\mathrm{S}_{\rm Tot}$:

$$\boxed{\frac{\mathrm{dV}_i}{\mathrm{dS}_{\mathrm{Tot}}} = \frac{1}{\frac{(n+1)}{2}} \frac{(n-i)}{n} e^{j2\pi(ux_i+vy_i)}} \tag{4.10}$$

(ii) V_i with respect to the log of LA (LLA):

$$\frac{\mathrm{dV}_i}{\mathrm{dLLA}} = \frac{\mathrm{dV}_i}{\mathrm{dLA}} \frac{\mathrm{dLA}}{\mathrm{dLLA}},$$

where,

$$\frac{\mathrm{dLA}}{\mathrm{dLLA}} = 1.e^{\mathrm{LLA}} = \mathrm{LA},$$

$$\begin{aligned}
\frac{\mathrm{dV}_i}{\mathrm{dLA}} &= \frac{\mathrm{S}_{\mathrm{Tot}}}{\frac{(n+1)}{2}} \frac{(n-i)}{n} e^{j2\pi(ux_i+vy_i)} \frac{d}{\mathrm{dLA}} \left[2\pi j \left(u\mathrm{LA}\frac{i}{n}\sin\theta + v\mathrm{LA}\frac{i}{n}\cos\theta \right) \right] \\
&= \mathrm{S}_i e^{2\pi j(ux_i+vy_i)} j \left(u\frac{i}{n}\sin\theta + v\frac{i}{n}\cos\theta \right) \\
&= \mathrm{S}_i e^{2\pi j(ux_i+vy_i)} j \left(\frac{1}{\mathrm{LA}} ux_i + \frac{1}{\mathrm{LA}} vy_i \right) \\
&= \mathrm{S}_i e^{2\pi j(ux_i+vy_i)} \frac{j}{\mathrm{LA}} \left(ux_i + vy_i \right)
\end{aligned}$$

Therefore,

$$\boxed{\frac{\mathrm{dV}_i}{\mathrm{dLLA}} = \mathrm{S}_i e^{2\pi j(ux_i+vy_i)} j \left(ux_i + vy_i \right)} \tag{4.11}$$

(iii) V_i with respect to θ:

Let

$$\mathrm{R} = \mathrm{S}_i e^{2\pi j(ux_i+vy_i)}$$

$$\begin{aligned}
\frac{\mathrm{dV}_i}{\mathrm{d}\theta} &= \mathrm{R}\frac{\mathrm{d}}{\mathrm{d}\theta} \left[\mathrm{S}_i \left(e^{2\pi j\mathrm{LA}u\frac{i}{n}\sin\theta} e^{2\pi j\mathrm{LA}v\frac{i}{n}\cos\theta} \right) \right] \\
&= \mathrm{RS}_i 2\pi j\mathrm{LA}\frac{\mathrm{d}}{\mathrm{d}\theta} \left(u\frac{i}{n}\sin\theta + v\frac{i}{n}\cos\theta \right) \\
&= \mathrm{RS}_i 2\pi j\mathrm{LA} \left(u\frac{i}{n}\cos\theta - v\frac{i}{n}\sin\theta \right) \\
&= \mathrm{RS}_i 2\pi j \left(uy_i - vx_i \right)
\end{aligned}$$

Therefore,

$$\boxed{\frac{\mathrm{dV}_i}{\mathrm{d}\theta} = \mathrm{S}_i e^{2\pi j(ux_i+vy_i)} 2\pi j \left(uy_i - vx_i \right)} \tag{4.12}$$

After deriving the model visibility with respect to the model parameters, an algorithm for the ASYM model is written and implemented in the model-fitting program, OMFIT. Please see Appendix .1

4.4 Test of ASYM Model with DOT Model

The intent of this section is to test our OMFIT program by comparing the fit for a point source model (henceforth, referred to as the DOT model) and the ASYM model to ensure that the latter is doing the correct minimisation. We start with a test to compare a Point Source Model (DOT) model fit with a restricted version of our ASYM model by fitting only one point source (N = 1), in particular, the point at the nominal position ($i = 0$) for e.g., see graphical illustration 4.4. With only one point source, the ASYM model reduces to a single point source with only real parameters being the x and y positions and its flux density. As a result, we have found that the fitted values for the positions (x_0 and y_0 or E and N offsets) and the flux density agree exactly between the DOT and the ASYM models (i.e., the DOT and ASYM models return the same fitted values and χ^2).

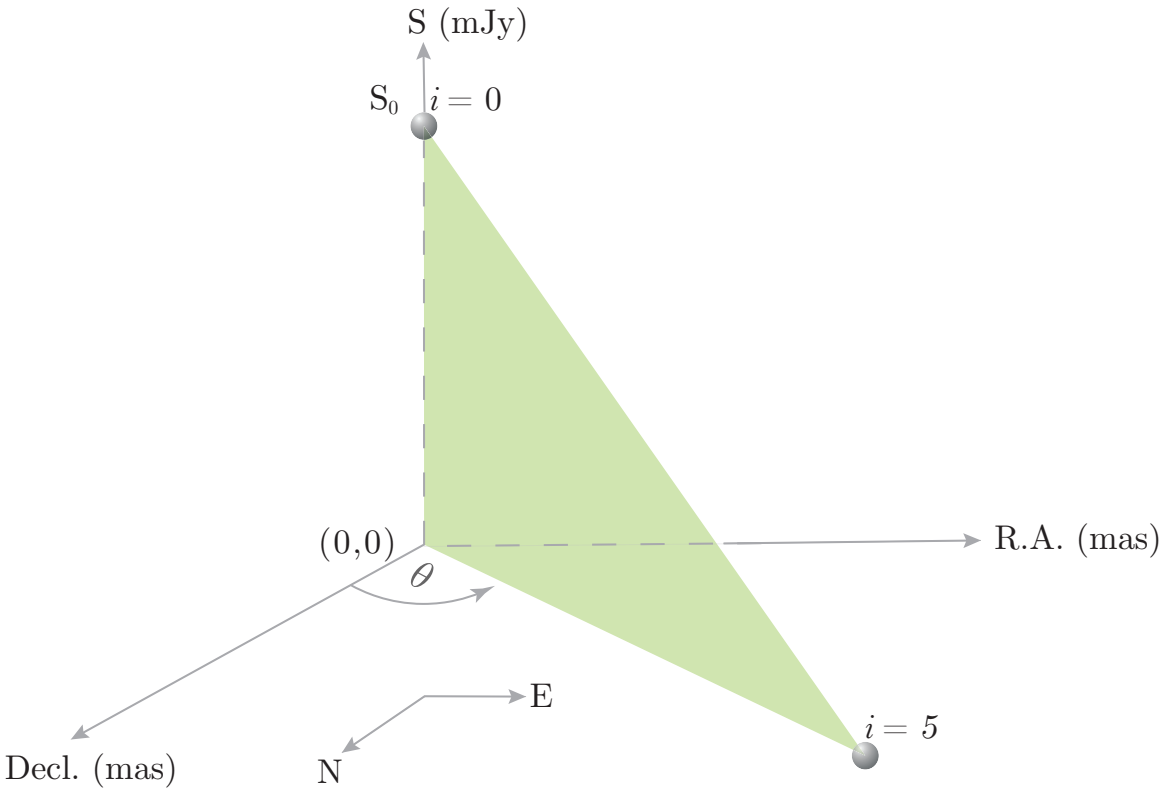

Figure 4.3: Schematic diagram of the ASYM model illustrating the first and last point sources where $i = 0$ is the central point source (also taken as the nominal position of the model), and $i = 5$ is the last point source.

A second test to ascertain that our programming code for the ASYM model in OMFIT is giving the correct output, we isolated only the last point source ($i = 5$) in ASYM model and see if the

latter fits the same point source (N and E offsets) as the DOT model. For ASYM($i = 5$) model, the positions (x and y), length, and position angle parameters all factor into the actual position of the point source. Hence, fixing the positions (x and y) also served to test the length and position angle (free) parameters in ASYM model. After trying some combinations of x and y positions, the length and position angles, the fitted values agree between the DOT and ASYM models to less than their fitted uncertainties. We also obtained exactly the same χ^2 when fixing all the model parameters at equivalent values for DOT and ASYM, suggesting that the model calculation of ASYM is indeed correct.

4.5 Test of ASYM Model with a Sum of N Point Sources

To test our OMFIT program for the ASYM model in its entirety, we made use of three triangle model data for sources near (but not necessarily exactly) at the phase-reference point ($x_0 = y_0 = 0$; except for the data model of length 1.1 mas, labelled as Model_V1.1), and all the model data are noise-free (see Table 4.1). The model data are made up of data sets (using N = 2000 point sources) where the visibility data correspond to a *known* triangle function into OMFIT. Our objective was to see whether our OMFIT program can recover the correct fitted parameter values when we fit ASYM to those three data models. The fitted parameters are the total flux densities (in our test case, all the model data are exactly at 1 Jy), different position offsets, lengths, and position angles as shown in Table 4.1. We also investigated the behaviour of the fits when we increased the number of point sources, N_OMFIT in the OMFIT program for our ASYM model.

The Figures 4.4 and 4.5 respectively show the plots for the fitted flux densities and position angles as a function of the number of point sources in OMFIT. For a data model of the length of 0.5 mas, N_OMFIT = 6 is sufficient to recover its total flux density. However, a misfit in the total flux density can be seen if we use only 6 point source approximation for data models of length > 0.5 mas. The ASYM model recovers the exact total flux density with N_OMFIT $\gtrsim 50$ point source approximation, regardless of the length or p.a. of our test models. Figure 4.5 shows a constant value for the model data's respective fitted position angles, and suggests that the fit for the p.a is independent of the number of point source approximation, N_OMFIT.

Table 4.1: Parameters of the triangle test models

Model versions	No. of Point sources, N	Total Flux Density (Jy)	length (mas)	Epos (mas)	Npos (mas)	p.a. (°)
Model_V2.0	2000	1.0	2.0	0.00	0.0	-12.0
Model_V1.1	2000	1.0	1.1	0.30	0.8	70.0
Model_V0.5	2000	1.0	0.5	0.00	0.0	30.0

Moreover, the Figures 4.6 and 4.7 respectively show the dependence of the model lengths and position offsets as a function of N_OMFIT and 1/N_OMFIT. In both cases, the model lengths and position parameters are recovered when N_OMFIT $\gtrsim$ 50 point source approximation is used, and both parameters vary linearly as a function of 1/N_OMFIT. Lastly, we analysed the behaviour of the fit for the model data positions as a function of length as shown in Figure 4.8a, and we found that there is a linear variation of the position offsets as a function of the model lengths.

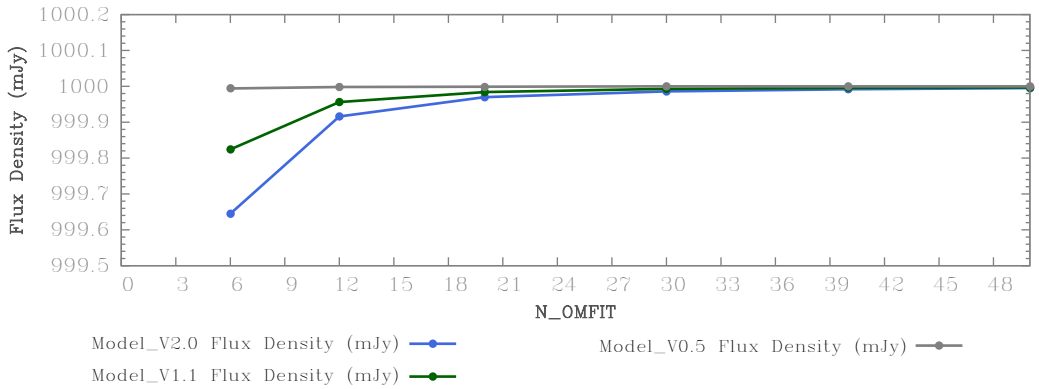

Figure 4.4: Behaviour of the total flux densities of the model data as a function of N_-OMFIT.

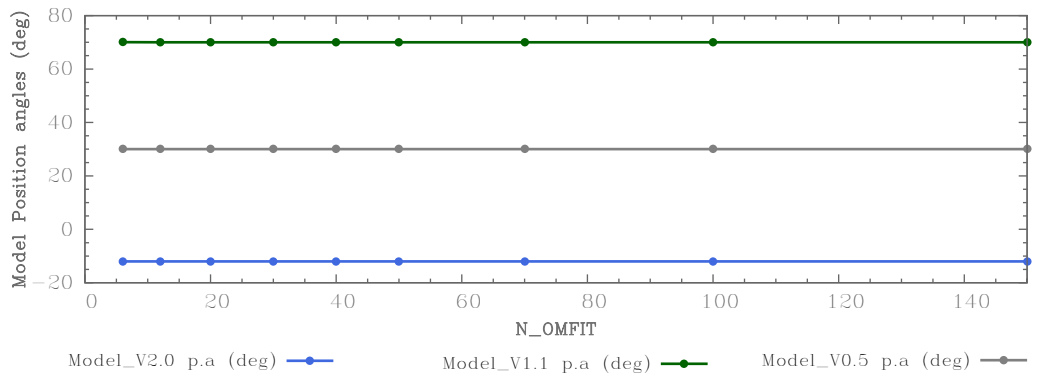

Figure 4.5: Behaviour of the position angles of the model data as a function of N_OMFIT.

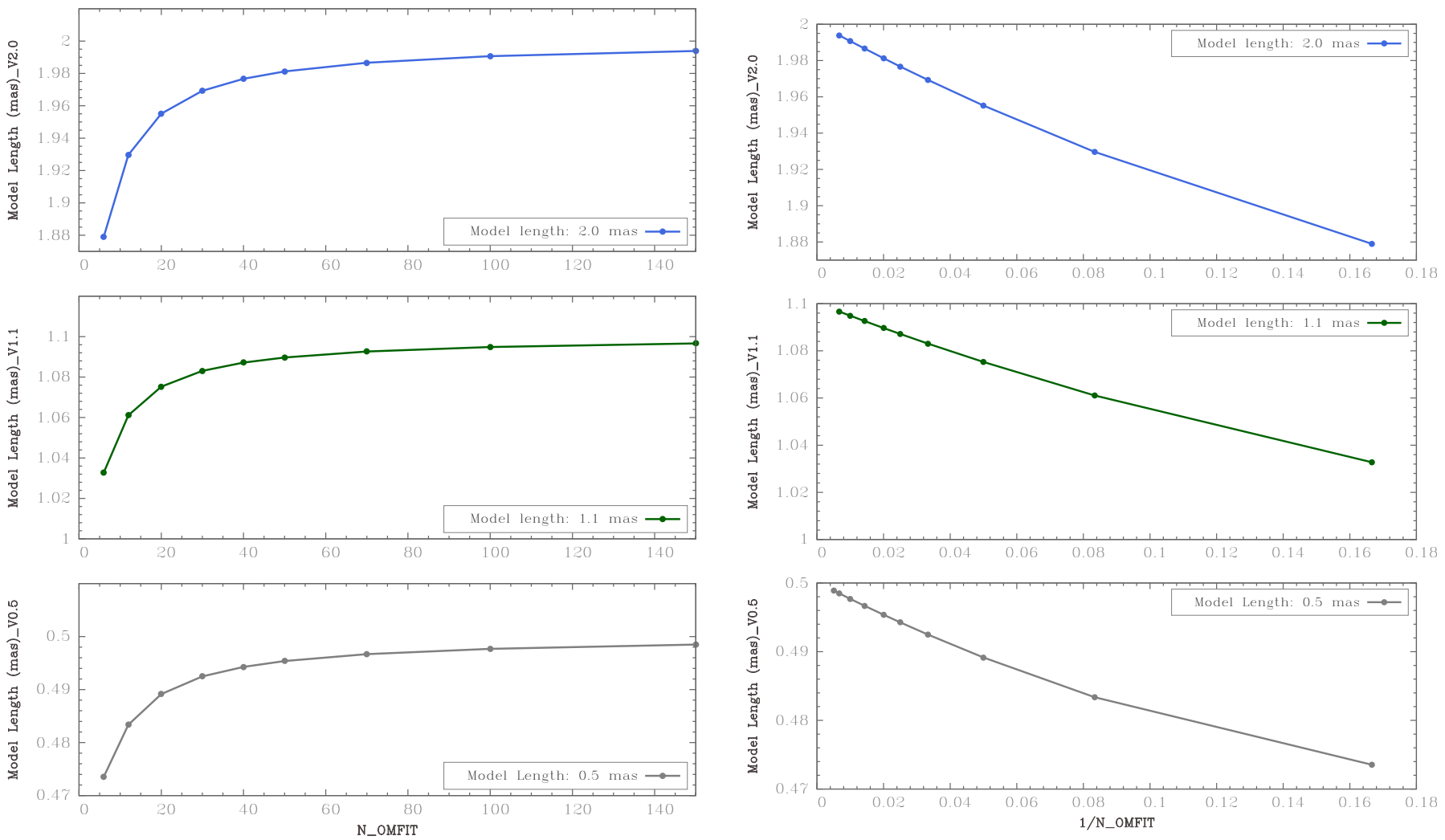

Figure 4.6: Behaviour of lengths of the model data as a function of N_OMFIT and 1/N_OMFIT.

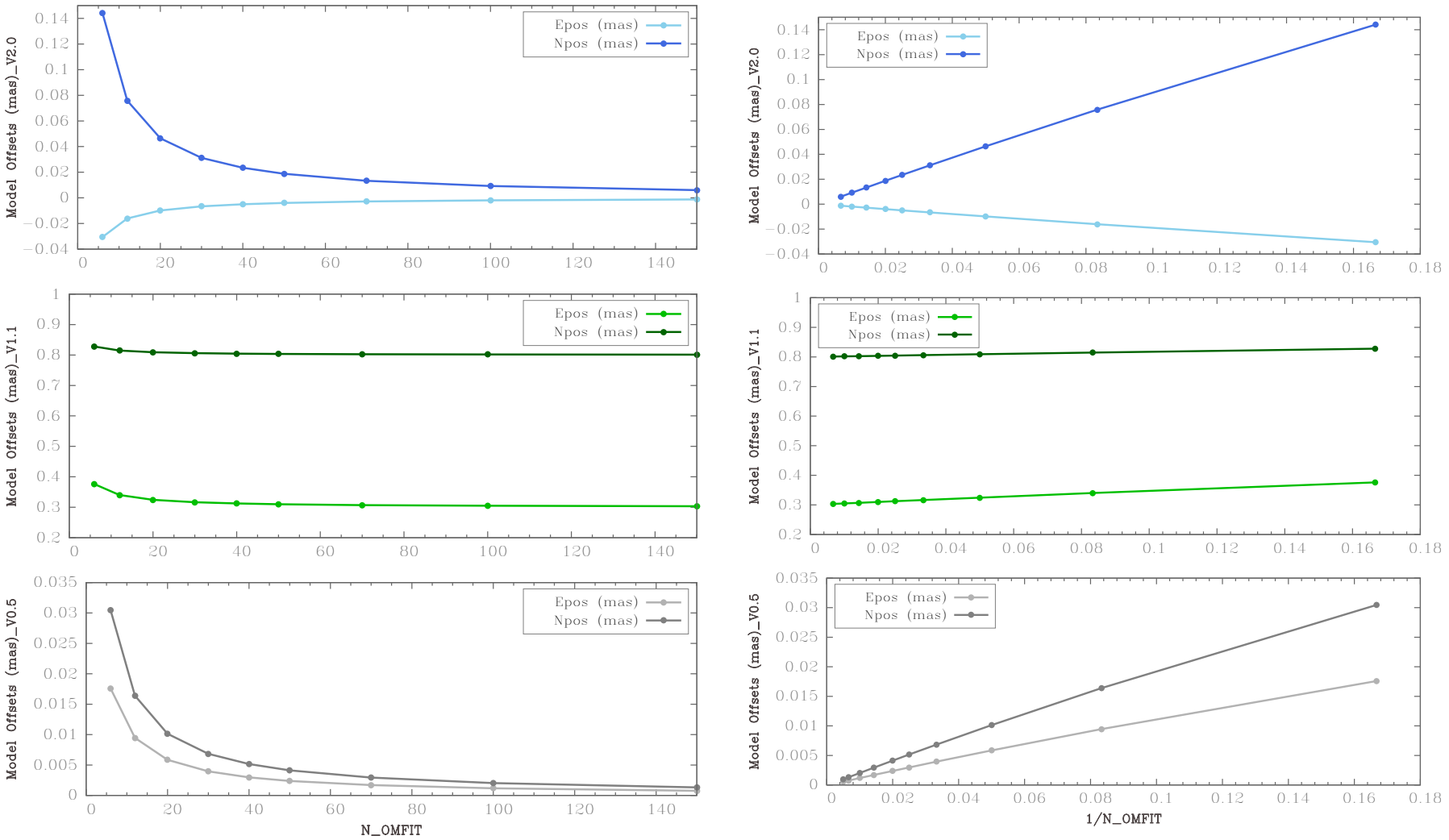

Figure 4.7: Behaviour of position offsets of the data models as a function of N_OMFIT and 1/N_OMFIT.

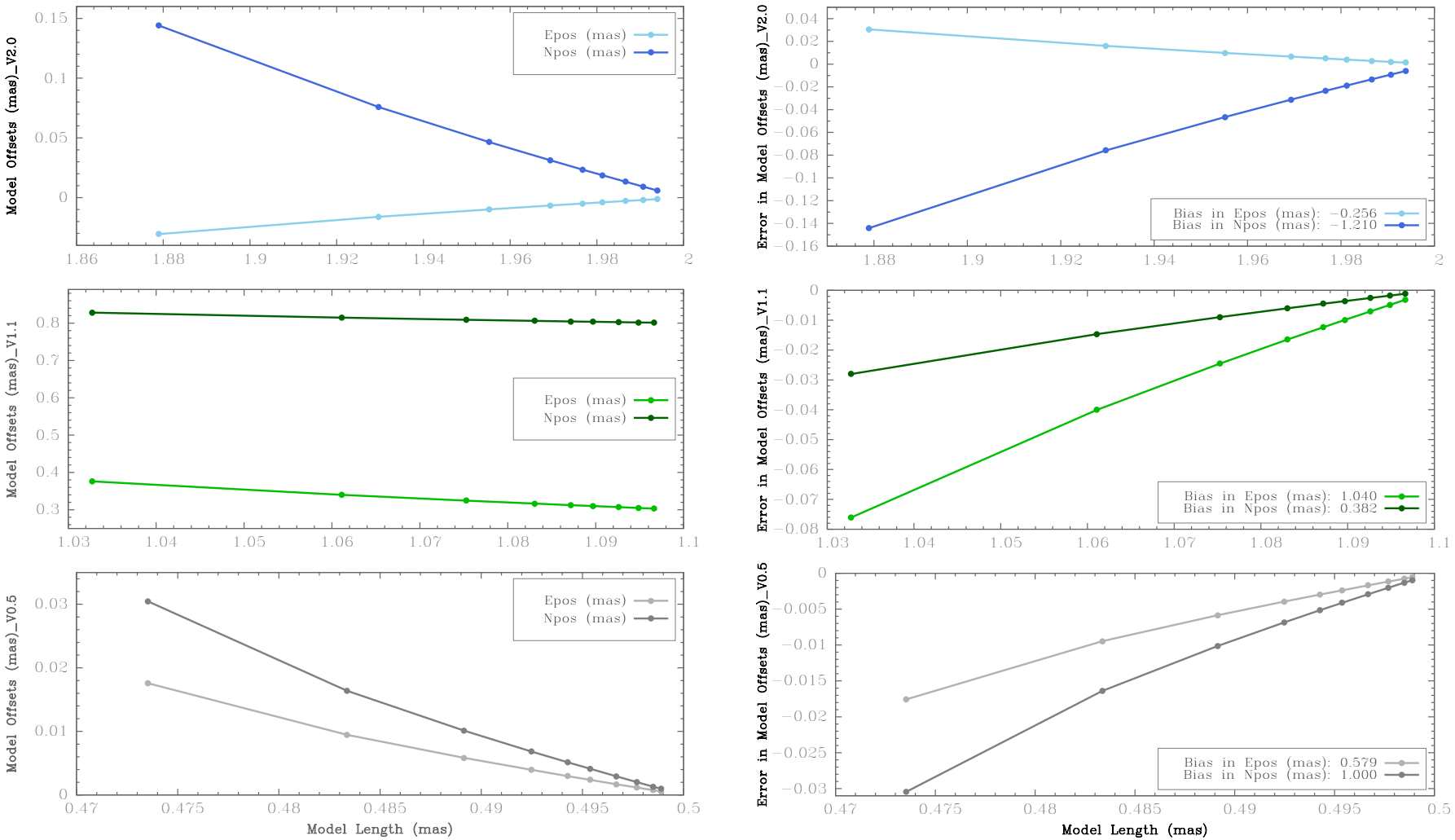

(a) Behaviour of model offsets as a function of lengths.

(b) Biases in model offsets as a function of lengths

Figure 4.8: Model behaviour and position offsets as a function of model lengths.

So far we have established that our ASYM model fits the visibility test data better for larger number of point source approximations (i.e., the biases are larger in small values of point source approximation in the ASYM model). Our triangle test models were generated using N=2000 point sources, large enough that increasing it further would make little difference, so any bias in the results that OMFIT reports would be due to the limited number of point source approximations in ASYM model, rather than the limited N used to generate the test data.

4.6 Test for Biases in ASYM Model

How much should we trust the results of OMFIT when using the ASYM model? The reliability of our results can be quantified by the precision of our ASYM model on how much its fitted values of (x_0, y_0), and length are biased as a function of N_OMFIT and model length. The plot 4.8b shows the error in the model offsets positions as a function of model lengths (keeping the value of point source approximation in ASYM constant). The biases in the model positions vary linearly with the model lengths and on comparing the three different model data from 0.5 to 2.0 mas, the biases in position offsets increases for a model data with increasing model lengths. The Figures 4.9 and, 4.10 show the variation of biases in model lengths and position offsets as a function of N_OMFIT and 1/N_OMFIT respectively. Even in these two cases, the biases seem to be dependent on 1/N_OMFIT.

We have found that the ASYM model parameters for positions (x_0, y_0), and length are biased of the order of length/N_OMFIT. Since the source of the bias in ASYM model fits depends on the point source approximation in ASYM model, it became clear that we need to make use of a larger number of point sources in the ASYM model to reduce the bias in our model fits. However, by how much should we increase the number of point sources in the ASYM model?

Before answering the above question, there is another question we should ask ourselves: When should we use the ASYM model? The ASYM model should be used mainly for marginally resolved sources (a good example is the nuclear region of the M81 galaxy). In the case of radio sources that are highly resolved and with sources that are larger than the resolution, one can work in the image plane and use imaging technique to analyse and study their sources. Moreover, for highly resolved sources, one needs a very large value of point sources in OMFIT program for the ASYM model so that the point source approximation to the model is reasonably close to the continuous

one.

Another consideration to ensure that ASYM model is working properly, the point-source approximation in ASYM model should be much closer than the resolution, θ:

$$\theta_{\mathrm{FWHM}} \simeq \frac{3438}{\mathrm{B_{max}}/\lambda}\mathrm{arcminutes} \tag{4.13}$$

The resolution from our u-v visibilities, estimated at 300 Mλ is 0.6876 ($\sim$ 0.70 mas FWHM) and the point sources in ASYM model are apart by $\sim$ 0.20 mas ($\sim$ FWHM/4). For a model length of 1.0 mas, using a series of less than 6 point sources (i.e., N_OMFIT < 6), makes the OMFIT's point sources in ASYM more than $\sim$ 0.17 mas apart relative to the beam, and gives us a very poor fit for the visibility data as the ASYM model becomes too crude. Using N_OMFIT > 100, where the ratio of Length/N_OMFIT $= 1/100 = 0.01$, making the point source approximations closer together than the beam and thus could give a much better fit for the visibilities.

To conclude, for a good compromise between computing speed[2] and resolution, we opted for N_OMFIT $= 50$. With N_OMFIT $= 50$, we obtain 10 points per FWHM out of 5*FWHM which is a reasonable compromise. For AGN with jet longer than 5*FWHM, one can use the imaging technique to analyse the source rather than turning to model fitting with the ASYM model. So then the "safe" region where we can expect the ASYM model to produce reliable results is when the biases are less than the realistic uncertainties provided by OMFIT, or $< 5\%$ of the FWHM.

[2]The runtime of OMFIT was $\sim$ 3 mins on average from HartRAO server which has a 3.20 GHz Intel Core i7 processor.

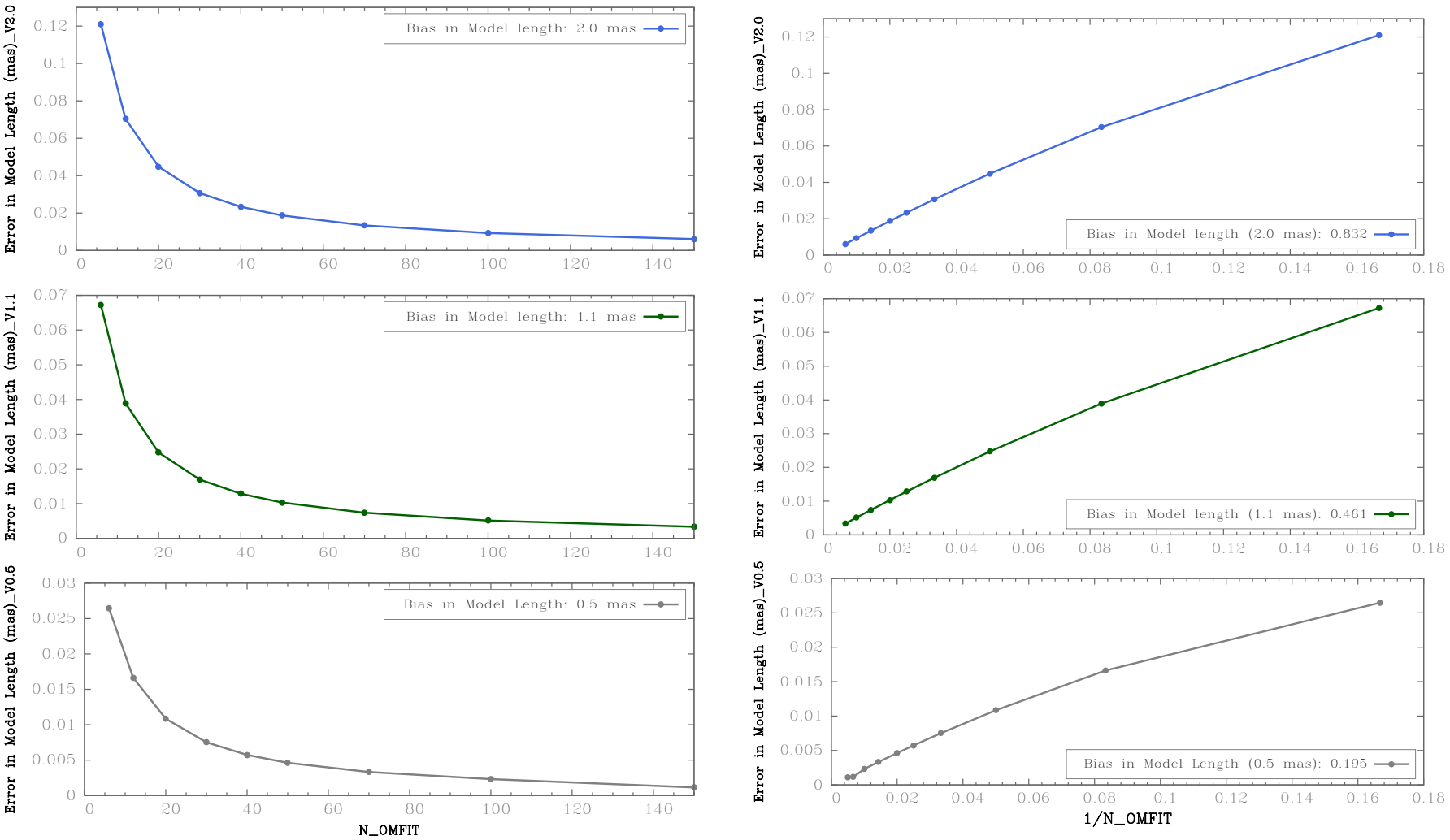

Figure 4.9: Biases in the model lengths as a function of N_OMFIT and 1/N_OMFIT.

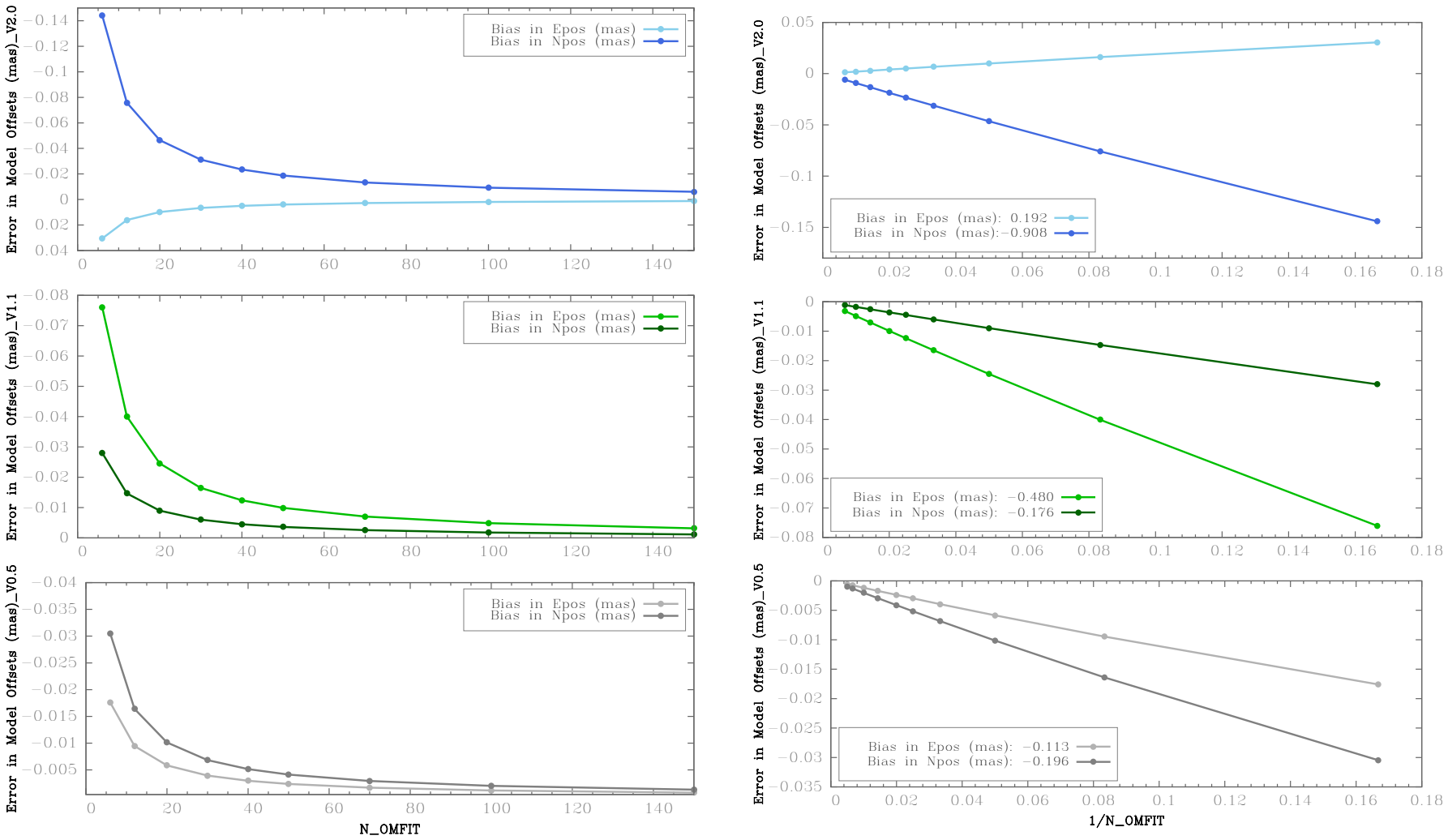

Figure 4.10: Biases in the model offsets as a function of N_OMFIT and 1/N_OMFIT.

Summary of Chapter 4 - Fourier-Plane Modeling:

1. The DOT and GAUS models are introduced as the two commonly used models for the parameterisation of a source brightness distribution.

2. The fact that the nature of M81* is not well-known, we developed a simple triangular model (referred to as ASYM) to reflect the shape of a core-jet structure often seen at mas scales. ASYM is a strictly one-sided model and is made up of a series of point sources to approximate a continuous triangular shape.

3. Since we do not have the measurements to justify a more complicated model, the least number of free parameters are attributed to ASYM, namely the flux density, position offsets, length, and position angle; compared to one or more elliptical GAUS models.

4. The parameters of the point sources in the ASYM model are functionally related to each other and lends itself easily to distributions along a line, making it relatively easy to generalise to non-linear slopes in flux density of the jet in M81*.

5. To convince ourselves that our model is doing the correct minimisation, we put ASYM to test by isolating two independent point sources (one at the nominal position and one at the lower end of the triangle) and their fitted values were compared to that of a DOT model located at the same positions. We confirm that the model calculation of ASYM is indeed correct as the latter returns the same fitted values and χ^2 to that of the DOT models.

6. We further tested ASYM with a sum of point sources using three test data models of varying model parameter values. Our objective was to see whether our OMFIT program can recover the correct fitted parameter values when we fit ASYM to those data models. We have found that the models' respective fitted values for the flux densities, lengths, and position offsets are recovered when we used ASYM made up of $\gtrsim 50$ point sources, with the exception of the position angles which are independent of the number of point source approximation.

7. Lastly, we tested the biases in the ASYM model. We found that ASYM model parameters for position offsets and length are biased of the order of length/N_OMFIT, suggesting that a larger number of point sources needed to be used. For a good compromise between computing speed and resolution, we settled down for a value of 50 point sources to be used for the ASYM model.

'A truly open mind means forcing our imaginations to conform to the evidence of reality, and not vice versa, whether or not we like the implications.'

Lawrence Krauss – A Universe from Nothing.

5

Results and Discussions

5.1 VLBI Model-Fitting Results

To characterise the emission region of M81*, the defining parameters of the ASYM and GAUS models are estimated for each epoch using the OMFIT program. This program includes complex antenna gains as free parameters in the fit. The best-fit model parameters for each epoch and frequency are listed in Table 5.1 and plotted in Figure 5.1. Constant standard errors of 40 μas at each frequency (which includes statistical and systematic contributions) were adopted and these standard constant errors represent, perhaps, an overestimate of the true uncertainty (please see Bietenholz et al. 2000 and Bietenholz et al. 2001 for a detailed discussion). In addition, the means of the parameter estimates and the root-mean-square (rms) values are given at the bottom of the respective columns in the same table. The uncertainties for the size and orientation are taken as 30 μas in the FWHM and 3° in the p.a. respectively (Bietenholz et al.,

2000). The position offsets of the fitted GAUS and ASYM models listed in Table 5.1 are given relative to the nominal correlator position. Due to phase self-calibration on M81*, the absolute position is lost, and the brightness peak appears very close to the nominal position. The offsets cannot, therefore, be directly compared between epochs; however, for each epoch, the offset between the GAUS and ASYM positions is meaningful.

The second column in Table 5.1 shows the fitted flux density of M81* at 8.4 GHz where the mean value is 130 mJy with a standard deviation of 38 mJy or 29%. At 5.0 GHz, the mean observed flux density is 119 mJy with a standard deviation of 35 mJy or 29%. The output in column (3) of Table 5.1 shows the fitted major axis of the Gaussian model (i.e., GAUS: FWHM at 8.4 and 5.0 GHz). On average, the FWHM of the GAUS model varies from $\sim 0.54 \pm 01.0$ mas at 8.4 GHz to $\sim 0.88 \pm 0.15$ mas at 5.0 GHz. The column (8) shows the fitted length of the ASYM model (i.e., ASYM: LEN at 8.4 GHz) to be $\sim 0.90 \pm 0.16$ mas on average.

The column (5) is that of the fitted p.a. of the GAUS model at the same two frequencies. On average, the fitted p.a. of the jet are $\sim 53^\circ$ and $\sim 59^\circ$ at 8.4 and 5.0 GHz respectively, suggesting that the p.a. of the jet extension is bent to the east at a lower frequency. The column (9) of Table 5.1 shows that the fitted p.a. of the ASYM model yields on average, a value of $\sim 55^\circ$ at 8.4 GHz. On comparing the average p.a. of the jet extension estimated by the ASYM and GAUS models at 8.4 GHz, we can see a strong agreement of the p.a. of the jet at larger and smaller radii respectively, along the jet axis of M81*.

Our model-fitting results show that a simple elliptical Gaussian model fits the visibility data of M81* better (i.e., has a lower reduced χ^2; although we may be somewhat overestimating the significance of how much better one model is over the other) than the ASYM model; except for 5 out of our 22 datasets at 8.4 GHz. To ensure that for most of the epochs, the GAUS is indeed a better fit to the visibility data of M81*, we performed an additional test by comparing models with the same number of free parameters, i.e., using a one-dimensional Gaussian model (by fixing the axis ratio to zero) and the ASYM model. With both models comprising of five free parameters each, we noticed that the ASYM model consistently fits poorly for most epochs. It is notable that since the real uncertainties on the visibility values are unknown, the actual reduced chi-squared values cannot be calculated. Instead, we calculate the scaling between the sum of square residuals and reduced chi-squared by assuming that the GAUS model produces the expected reduced chi-squared value of DOF (for large DOF) for each epoch, and we then compared the reduced chi-squared for the ASYM and GAUS models for each epoch. The epochs

Table 5.1: Summary of the VLBI model-fitting results

		Elliptical Gaussian (GAUS) Model						ASYM Model				
Date	S	major	minor	p.a.	$\Delta\alpha$	$\Delta\delta$	Reduced χ^2	length	p.a.	$\Delta\alpha$	$\Delta\delta$	Reduced χ^2
(dd/mm/yy)	(mJy)	(mas)	(mas)	(°)	(mas)	(mas)	-	(mas)	(°)	(mas)	(mas)	-
(1)	(2)	(3)	(4)	(5)	(6)	(7)	(8)	(9)	(10)	(11)	(12)	(13)
					8.4 GHz							
26/06/93	97.49	0.44 ± 0.03	0.04 ± 0.03	57 ± 3	0.37	0.24	639	0.78 ± 0.05	55 ± 3	0.64	0.45	369
18/09/93	94.74	0.45	0.17	53	0.36	0.27	4822	0.73	60	0.63	0.36	6052
16/12/93	80.94	0.44	0.21	50	0.34	0.28	5452	0.76	57	0.63	0.41	6066
28/01/94	100.37	0.46	0.16	48	0.34	0.31	4809	0.79	53	0.61	0.46	5157
14/03/94	84.58	0.61	0.15	45	0.43	0.43	15109	1.00	49	0.75	0.66	17866
21/04/94	140.59	0.61	0.14	46	0.43	0.42	11652	0.98	45	0.70	0.69	13781
21/06/94	116.21	0.61	0.17	45	0.43	0.43	19685	1.07	47	0.78	0.73	19730
29/08/94	95.76	0.72	0.13	46	0.52	0.50	8406	1.20	49	0.91	0.79	8487
30/10/94	105.78	0.42	0.10	47	0.31	0.29	8548	0.70	52	0.55	0.43	8702
23/12/94	81.46	0.50	0.21	48	0.37	0.34	14226	0.86	51	0.67	0.54	15635
12/02/95	136.40	0.45	0.18	49	0.34	0.29	10821	0.76	47	0.56	0.52	15932
17/08/95	151.96	0.70	0.12	52	0.55	0.43	1881	1.13	64	1.01	0.51	1880
18/12/95	117.81	0.46	0.17	53	0.37	0.28	8683	0.90	50	0.68	0.58	8221
07/04/96	145.57	0.59	0.18	58	0.50	0.32	9217	0.60	45	0.42	0.43	13085
31/08/96	146.74	0.53	0.12	49	0.40	0.35	8604	0.93	50	0.71	0.60	8424
13/12/96	150.93	0.55	0.29	52	0.44	0.35	10192	0.98	57	0.82	0.53	10129
06/06/97	110.44	0.54	0.15	52	0.42	0.33	7491	0.91	55	0.75	0.52	7493
14/11/97	162.43	0.45	0.15	55	0.37	0.26	18819	0.73	60	0.63	0.37	26968
02/06/98	206.82	0.66	0.16	57	0.56	0.36	22250	1.05	54	0.85	0.61	56304
07/12/98	209.74	0.58	0.24	66	0.53	0.23	21501	1.04	66	0.95	0.42	22141
24/02/00	184.49	0.68	0.20	65	0.61	0.29	34801	1.10	69	1.03	0.39	108407
12/11/00	142.12	0.51	0.24	63	0.46	0.23	29084	0.91	64	0.81	0.41	41251
Average	130	0.54	0.17	53	0.43	0.33	–	0.90	55	0.73	0.52	–
Rms	38	0.095	0.05	6	0.08	0.07	–	0.16	7	0.15	0.12	–

Table 5.1: continued.

		Elliptical Gaussian (GAUS) Model						ASYM Model				
Date	S	major	minor	p.a.	$\Delta\alpha$	$\Delta\delta$	Reduced χ^2	length	p.a.	$\Delta\alpha$	$\Delta\delta$	Reduced χ^2
(dd/mm/yy)	(mJy)	(mas)	(mas)	(°)	(mas)	(mas)	-	(mas)	(°)	(mas)	(mas)	-
(1)	(2)	(3)	(4)	(5)	(6)	(7)	(8)	(9)	(10)	(11)	(12)	(13)
					5.0 GHz							
26/06/93	86.20	0.75 ± 0.05	0.23 ± 0.05	64 ± 5	0.67	0.33	–	–	–	–	–	–
14/03/94	79.40	0.64	0.29	57	0.54	0.35	–	–	–	–	–	–
21/06/94	97.43	0.77	0.23	56	0.19	0.13	–	–	–	–	–	–
29/08/94	96.05	0.85	0.29	52	0.67	0.52	–	–	–	–	–	–
31/10/94	87.46	0.89	0.26	54	0.72	0.52	–	–	–	–	–	–
23/12/94	75.45	0.91	0.27	51	0.71	0.57	–	–	–	–	–	–
10/05/95	123.19	0.88	0.19	48	0.65	0.59	–	–	–	–	–	–
18/12/95	105.54	0.96	0.26	56	0.80	0.54	–	–	–	–	–	–
26/07/96	130.00	0.74	0.36	65	0.67	0.31	–	–	–	–	–	–
31/08/96	127.03	0.93	0.24	55	0.76	0.53	–	–	–	–	–	–
13/12/96	136.40	1.23	0.32	56	1.02	0.69	–	–	–	–	–	–
14/11/97	104.31	0.74	0.29	60	0.64	0.37	–	–	–	–	–	–
20/11/98	206.25	1.08	0.27	55	0.88	0.62	–	–	–	–	–	–
16/06/99	148.63	0.87	0.42	66	0.79	0.35	–	–	–	–	–	–
23/11/99	173.96	1.03	0.35	68	0.95	0.39	–	–	–	–	–	–
09/06/01	110.92	0.75	0.36	75	0.72	0.19	–	–	–	–	–	–
24/05/02	133.72	0.95	0.29	72	0.90	0.29	–	–	–	–	–	–
Average	119	0.88	0.29	59	0.72	0.43	–	–	–	–	–	–
Rms	35	0.15	0.06	8	0.18	0.16	–	–	–	–	–	–

The description of the columns of Table 5.1 is given as follows. Columns:

(1): The date (start of the observing run) in chronological order,

(2): The total flux density of M81* at 8.4 and 5.0 GHz observations,

(3): The FWHM of the major axis of the GAUS model,

(4): The FWHM of the minor axis of the GAUS model,

(5): The p.a. of the major axis of the GAUS model,

(6) & (7): the position offsets of the GAUS model relative to an arbitrary reference position used at the correlator within each epoch,

(8): The reduced chi-squared of the GAUS model displayed by OMFIT is equal to some scaling factor, Q times the actual reduced chi-squared. By assuming that the GAUS model is producing the best fit and is equal to the DOF, we calculated the scaling factor,

(9): The length of the ASYM model,

(10): The p.a. of the ASYM model,

(11) & (12): The position offsets of the ASYM model relative to an arbitrary reference position used at the correlator within each epoch,

(13): The actual reduced chi-squared of the ASYM model is calculated by multiplying the scaling factor, Q with the chi-squared obtained by the OMFIT program.

for which the ASYM model fits better than the GAUS model at 8.4 GHz are: 26/06/93, 17/08/95, 18/12/95, 31/08/96, and 13/12/96.

5.2 Discussions

5.2.1 Variability of M81* with GAUS and ASYM Models

An overall description of the temporal variability of the emission region of M81* and its structural evolution using a GAUS model at 8.4 GHz, and both 8.4 and 5.0 GHz, have been reported in Bietenholz et al. (2000), and Martí-Vidal et al. (2011) respectively. However, in this section, we revisit the description of the temporal variability of the emission region of M81* and show how the source structure of M81* evolves, as parametrised by both the GAUS model (at 8.4 and 5.0 GHz) and ASYM model (at 8.4 GHz only). Time-series images of M81* at 8.4 and 5.0 GHz (Figures 5.2 and 5.3 respectively) have been made to support the arguments to follow about the variability of M81*.

The Figure 5.1 (c), *bottom panel* shows that the flux densities at 8.4 and 5.0 GHz seem to be well correlated while the flux densities at 8.4 GHz of the GAUS and ASYM models are strongly correlated with the VLA flux density (the flux density scale is set so the total flux density in the model is equal to that measured at the VLA). From the light curves, it is evident that M81* exhibits active flaring episodes at 8.4 and 5.0 GHz. Even if our data are more spread from 1997 onwards, we can observe a clear increase in the flux density (what seems to be a four-year-long radio flare), where both the fitted GAUS and ASYM increases from June of 1997 to a maximum ($\sim$ 209 mJy at both frequencies) in November 1998 and then begins to decrease through June 2001. Outside this four-year-long flare, the maximum peak brightness amounts to a factor of $\sim$ 2 of the typical peak brightness.

The position angle of the fitted GAUS and ASYM models shown in Figure 5.1 (b) *middle panel*, is systematically different at different epochs and frequencies. M81* seems to be mostly oriented along the northeast-southwest axis ($\sim 54^\circ$) where the position angles of both the GAUS and the ASYM models vary with time and frequency. This hints at an underlying structure of M81* being mostly linear, reminiscent of a jet. The variations of the p.a. of both models appear very similar and vary smoothly for most epochs. The p.a. of the Gaussian model at 8.4 GHz varies smoothly between 45° and 66° while the variation of the ASYM model is between 45° and 69°, both with a timescale of $\sim$ 1 year.

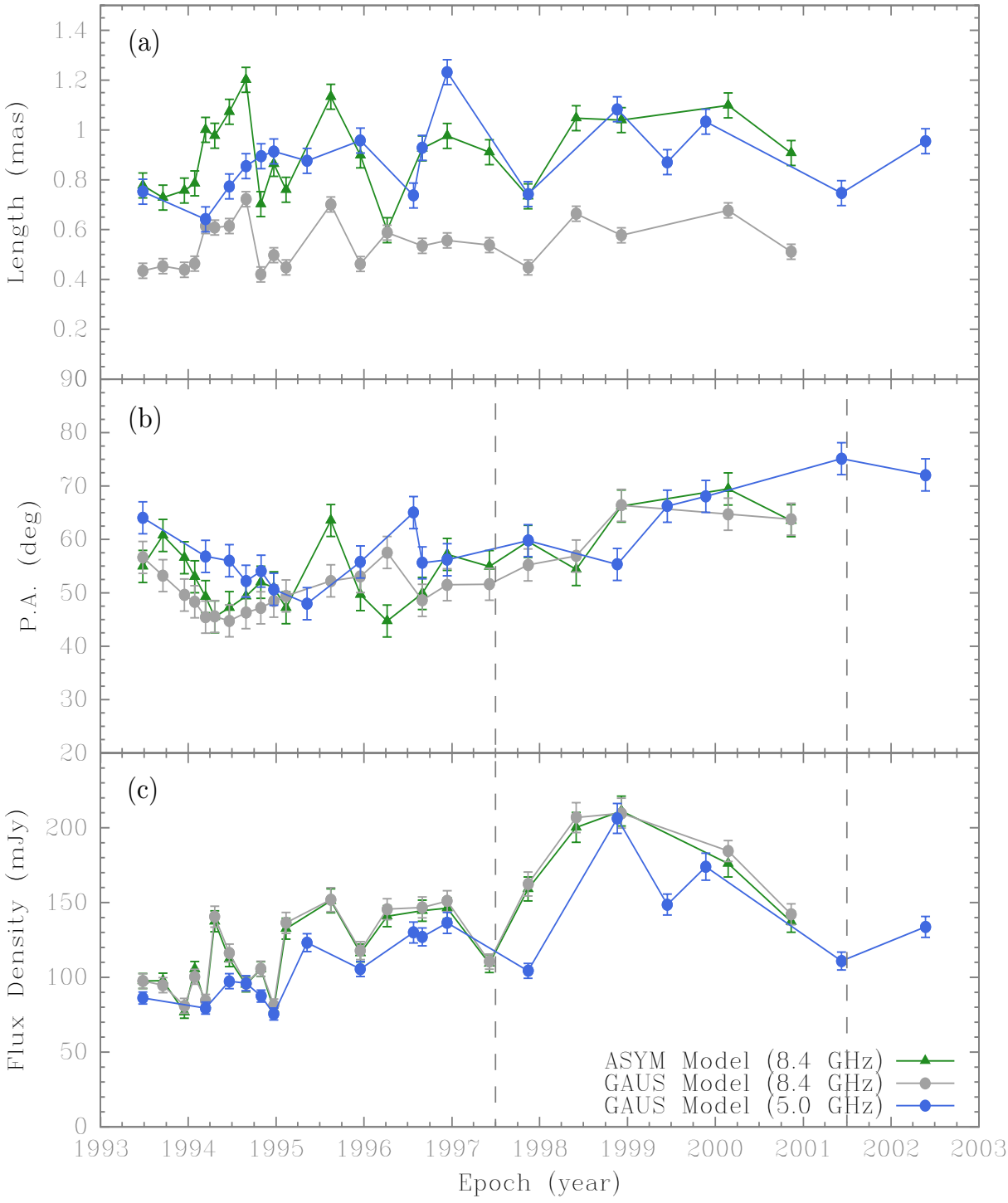

Figure 5.1: Temporal variability of the parameters of M81*. The parameters of the elliptical Gaussian at 8.4 GHz are indicated by grey circles, while those at 5.0 GHz are indicated by blue circles. The parameters of the ASYM are indicated by green triangles. The top panel, (a) shows the FWHM of the major axis of the GAUS model parameter and the length of the ASYM model. The central panel, (b) shows the p.a. of the major axis of the GAUS and that of the ASYM model. The lower panel, (c) shows the flux densities of the GAUS and the ASYM.

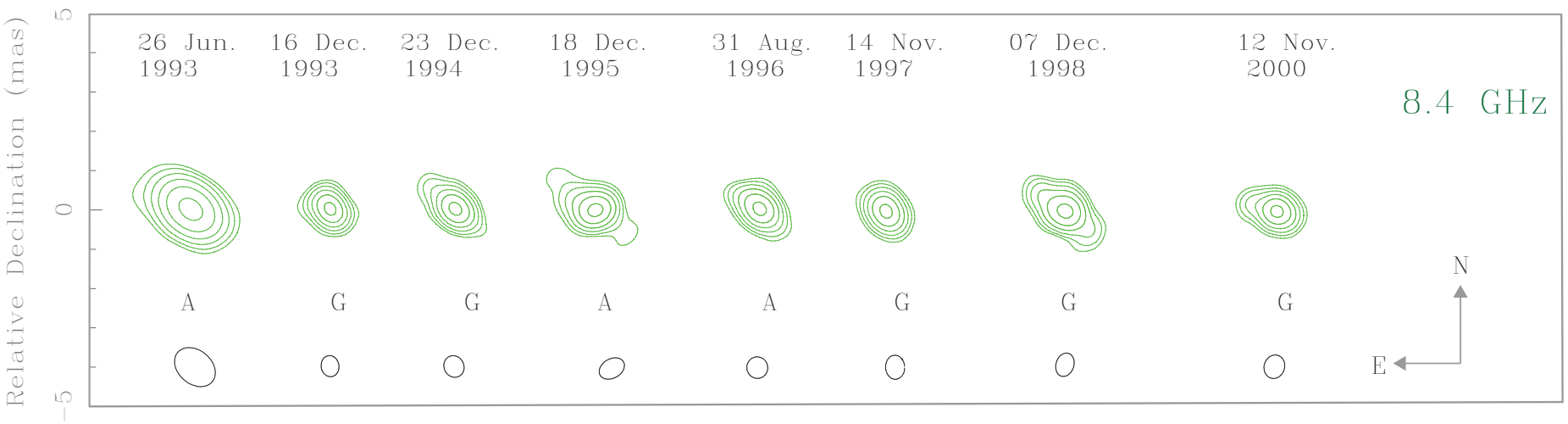

Figure 5.2: A sequence of images of M81★ showing its structural evolution from 1993 to 2000 at 8.4 GHz. For each image, the observing date, the peak brightness, and the contour levels which are at a percentage of the rms of the images are indicated below. The FWHM of the convolving beam is shown at the bottom of each image and listed below the images are the beam parameters in parentheses (FWHM major and minor axes, position angle). The labels A and G correspond to the epochs for which the ASYM and GAUS respectively provides a better fit for the visibility data of M81★. North is up and east is to the left.

(a) June 26, 1993; 95.4 mJy/beam
(1.18 × 0.871 mas at 49.4°)
Contours %: 2.5 5 10 20 40 80

(b) December 16, 1993; 56.2 mJy/beam
(0.549 × 0.46 mas at 10.1°)
Contours %: 2.5 5 10 20 40 80

(c) December 23, 1994; 59.0 mJy/beam
(0.572 × 0.512 mas at 28.1°)
Contours %: 2.5 5 10 20 40 80

(d) December 18, 1995; 83.9 mJy/beam
(0.698 × 0.5 mas at −60.2°)
Contours %: 2.5 5 10 20 40 80

(e) August 31, 1996; 103.0 mJy/beam
(0.56 × 0.541 mas at 14.3°)
Contours %: 2.5 5 10 20 40 80

(f) November 14, 1997; 122.0 mJy/beam
(0.623 × 0.949 mas at 3.06°)
Contours %: 2.5 5 10 20 40 80

(g) December 07, 1998; 111.0 mJy/beam
(0.618 × 0.464 mas at −18.3°)
Contours %: 2.5 5 10 20 40 80

(h) November 12, 2000; 88.9 mJy/beam
(0.533 × 0.463 mas at −19.8°)
Contours %: 2.5 5 10 20 40 80

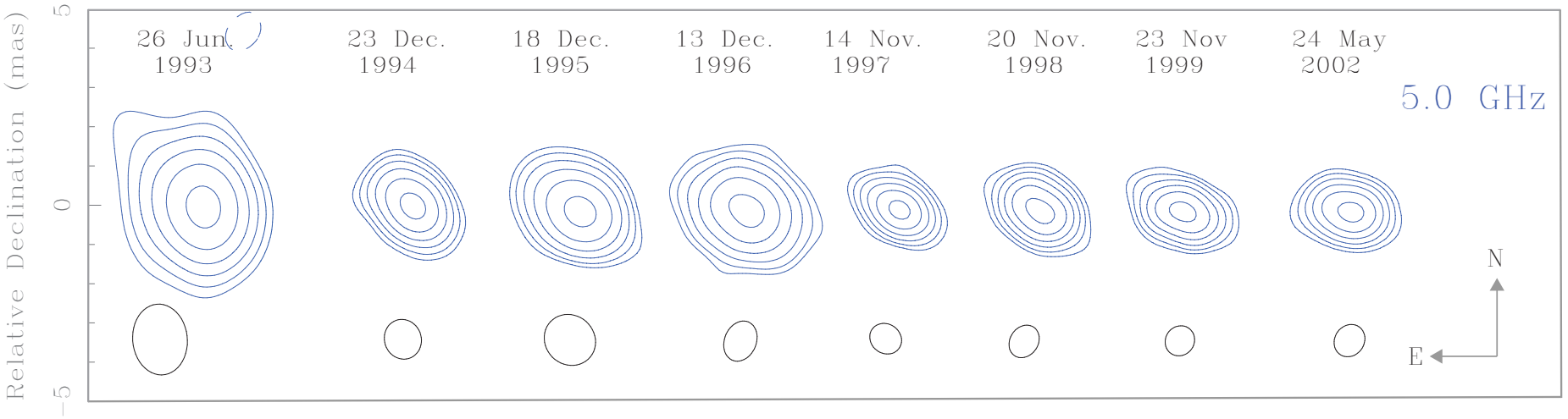

Figure 5.3: A sequence of images of M81* showing its structural evolution from 1993 to 2002 at 5.0 GHz. For each image, the observing date, the peak brightness, and the contour levels which are at a percentage of the rms of the images are indicated below. The FWHM of the convolving beam is shown at the bottom of each image and listed below the images are the beam parameters in parentheses (FWHM major and minor axes, position angle). North is up and east is to the left.

(a) June 26, 1993; 71.5 mJy/beam
(1.84 × 1.42 mas at 5.47°)
Contours %: -2.5 2.5 5 10 20 40 80

(b) December 23, 1994; 54.1 mJy/beam
(1.04 × 0.953 mas at 20.2°)
Contours %: 2.5 5 10 20 40 80

(c) December 18, 1995; 91.6 mJy/beam
(1.38 × 1.27 mas at 46.5°)
Contours %: 2.5 5 10 20 40 80

(d) December 13, 1996; 51.6 mJy/beam
(1.08 × 0.824 mas at $-22.4°$)
Contours %: -2.5 2.5 5 10 20 40 80

(e) November 14, 1997; 76.2 mJy/beam
(0.858 × 0.76 mas at 53.9°)
Contours %: 2.5 5 10 20 40 80

(f) November 20, 1998; 107.0 mJy/beam
(0.891 × 0.731 mas at $-33.9°$)
Contours %: 2.5 5 10 20 40 80

(g) November 23, 1999; 94.2 mJy/beam
(0.802 × 0.742 mas at $-37.4°$)
Contours %: 2.5 5 10 20 40 80

(h) May 24, 2002; 80.0 mJy/beam
(0.87 × 0.764 mas at $-34.3°$)
Contours %: 2.5 5 10 20 40 80

In addition, an elevated flux density from June 1997 to June 2001 seems to correspond to an increase in the p.a. of our fitted models (the increase in the p.a. of the GAUS model is more evident at 5.0 GHz) which suggests that the jet in M81* is moving towards a southwest direction. The position angle of the elliptical Gaussian model at 5.0 GHz increases from 60° to 75° during the four-year-long flare and the change in p.a. seems to decrease at later epochs or, even, to slightly reverse. Since the major axis of the fitted GAUS model and the length of the ASYM model are closely in line to the local direction of the jet in the region where the peak emission is produced, the different p.a. at different epochs indicate an evolving jet, bent to the east.

The Figure 5.1 (a), *top panel* shows the variations of the length of the fitted ASYM (i.e., ASYM: LEN at 8.4 GHz), and the major axis of the fitted GAUS model (i.e., GAUS: FWHM at 8.4 and 5.0 GHz). Our model-fitting results show that the fitted length of the GAUS and ASYM at 8.4 GHz are moderately well correlated and the variations in the length of the models are somewhat less smooth with the maximum length of the ASYM and GAUS models being $\sim$ 1.13 mas and $\sim$ 0.70 mas respectively. The length of the ASYM model is proportional to that of the elliptical Gaussian model at 8.4 GHz. There is an increase of $\sim$ 60% for the length of the major axis of the GAUS model between the 8.4 and 5.0 GHz by a fractional rms variation of the major axis of the GAUS model and length of the ASYM model of $\sim$ 11%. Even though the GAUS: FWHM is a better estimator of the source extent than ASYM: LEN, there is no apparent increase in the length of either GAUS or ASYM models which corresponds to the increase in flux density during its flaring periods between June 1997 to June 2001. Is is notable that the FWHM of the GAUS model is systematically larger at a lower frequency (it varies from $\sim$ 0.54 mas at 8.4 GHz to $\sim$ 0.88 mas at 5.0 GHz on average), thus indicating that the nuclear region of M81* at lower frequency is relatively broader (following the power-law as discussed in chapter 3, § 3.2).

Interestingly, the fitted length of the ASYM model at 8.4 GHz is much larger on average, with a value of $\sim$ 0.90 mas compared to $\sim$ 0.54 mas for the GAUS: FWHM model at the same frequency. Given that the ASYM results on length, position angle, and flux density are well-correlated with those from the GAUS model, this result seems to reflect the extent of the 50% point of both models (i.e., comparing the 0.5×LEN of the ASYM model to the FWHM of the GAUS model). Further, it is intriguing that for some reason, the fitted length of the ASYM model at 8.4 GHz is even larger compared to the major axis ($\sim$ 0.88 mas on average) of the GAUS model at 5.0 GHz. It might be plausible that the ASYM model is a better estimator of the physical length of M81* by tracing different parts of the continuous jet. However, given the scores of source morphologies, and our poor understanding of the physics, and our lack of knowledge of the actual physical lengths, it

seems unlikely that we could demonstrate which length parameter is more physical.

So far we have seen that the GAUS model is a better fit to M81* visibilities compared to the ASYM model. Even though the ASYM results on length, position angle, and flux density are well-correlated with those from the GAUS model, in general, one would rely on the fitted parameters of the GAUS model to extract useful information about M81*'s structure. However, we cannot make a general conclusion that the ASYM model would provide a statistically poorer fit without testing the model on at least a few other sources; the effort to fit the ASYM to an entirely different source is beyond the scope of this MSc thesis.

5.2.2 Estimation of the core position in AGN

Bietenholz et al. (2000) have shown that the 0.60 ± 0.30 FWHM from the centre of the GAUS model (towards its southwest half-maximum point) was the most stable point with respect to the centre of the source SN 1993J. They concluded from this stability that the stable point corresponds to the core of M81*. One of the differences between the GAUS and ASYM models is that the former is symmetrical while the ASYM model is asymmetric by nature. In order to estimate where the core might be located with respect to the radio brightness distribution, one need to consider how the radio brightness distribution is related to the physical structure. The nominal position of the GAUS model is at the centre of the elliptical Gaussian while for the ASYM model, it is at the position of its apex (i.e., the bright end of the triangle).

Should one resort to the 60% FWHM point to estimate the core position of a particular radio source, owing to the GAUS's symmetry, it cannot reveal on which side the bright end, presumably the position of the core should be. A GAUS model provides two points which are at $0.60\times$FWHM as shown in Figure 5.4. The best estimate for the core position would be an average value of those two points (i.e., the centre-point of the GAUS model). However, the centre-point of a GAUS model is not a good estimator for the core position and the nuclear region of AGN are known to exhibit rapid flux variability.

What follows is a test to demonstrate whether, on average, the nominal position of the ASYM model (even though ASYM provides a poorer fit in the case of M81*, its fitted parameter values are well correlated with those from the GAUS model) could be closer to the 60% FWHM point (towards the southwest along the fitted major axis) than is the centre-point of a GAUS model,

assuming that 60% FWHM prescription is the true position of the core at each epoch. We emphasise that the arguments to follow are rather speculative, and this effort is only to show whether the ASYM model can provide a strong impetus for further testing and usage on other sources which appear asymmetric on the smallest scales, including those with a well-established core position in literature such as M87 (Hada et al., 2011).

Since our data has been self-calibration in phase, the absolute position information is lost (see text § 2.2.1 for details). Hence, in this thesis, we restrict ourselves to relative positions of the peak brightness point within each epoch of observations; using the 60% FWHM: GAUS as our fiducial point. The position offsets of the fitted peak brightness point of the ASYM model (in columns 8 and 9 of Table 5.2) relative to the fiducial point, and peak brightness (nominal) point of the fitted GAUS model (in columns 10 and 11) are tabulated in Table 5.2 and plotted in Figure 5.5. The different peak brightness (x_0, y_0) positions that the GAUS (centre-point) and ASYM (apex) models return are also tabulated in Table 5.2: columns 2 & 3, and 6 & 7 respectively. While the centre of the fitted Gaussian is not formally identical to the peak brightness point of an arbitrary brightness distribution, they are virtually coincident to within a small fraction (< 10 μas) of the positional uncertainties of our self-calibrated data as shown in columns 2 and 3 of Table 5.2.

The Figure 5.5 shows that on average, the estimated distance of the brightness peak of ASYM relative to the fiducial point is 47 ± 20 μas (this value corresponds to a linear scale of ~ 186 AU at a distance of 3.96 ± 0.29 Mpc (Bartel et al., 2007) from Earth) at an angle of 45.5° while the estimated distance of the brightness peak of the ASYM model relative to the GAUS centre-point is 0.27 ± 0.04 mas (corresponds to $\sim 1,085$ AU on a linear scale); at an angle of 35.6°. In short, we have shown that the ASYM's nominal position is ~ 6 times closer to the 60% FWHM point than is the centre-point of a GAUS model, where the 60% FWHM point has been shown to be astrometrically stable in the particular case of M81* (Bietenholz et al., 2000).

Table 5.2: Position Offsets of Models Brightness Peak at 8.4 GHz

Date	Position Offsets		Fiducial Points		Position Offsets		Relative positions from			
	GAUS (centre)		GAUS at 0.6×FWHM (SW)		ASYM (apex)		ASYM to 0.6×FWHM (SW)		ASYM to GAUS (centre)	
(dd/mm/yy)	α (mas)	δ (mas)	α (mas)	δ (mas)	$\Delta\alpha$ (mas)	$\Delta\delta$ (mas)	α (mas)	δ (mas)	$\Delta\alpha$ (mas)	$\Delta\delta$ (mas)
(1)	(2)	(3)	(4)	(5)	(6)	(7)	(8)	(9)	(10)	(11)
26/06/93	0.00	0.00	-0.15	-0.07	-0.14	-0.07	0.01	0.00	-0.14	-0.07
18/09/93	-0.00	0.00	-0.22	-0.18	-0.19	-0.15	0.02	0.03	-0.19	-0.15
16/12/93	0.00	0.00	-0.21	-0.16	-0.19	-0.12	0.02	0.04	-0.19	-0.12
28/01/94	0.00	0.00	-0.23	-0.21	-0.20	-0.17	0.03	0.04	-0.20	-0.17
14/06/94	0.00	0.00	-0.27	-0.26	-0.22	-0.21	0.04	0.05	-0.23	-0.21
21/04/94	-0.00	0.00	-0.27	-0.25	-0.22	-0.21	0.04	0.04	-0.22	-0.21
21/06/94	0.00	0.00	-0.24	-0.22	-0.22	-0.18	0.02	0.04	-0.22	-0.18
29/08/94	0.01	0.01	-0.34	-0.30	-0.28	-0.25	0.05	0.04	-0.29	-0.26
30/10/94	0.00	-0.00	-0.19	-0.18	-0.17	-0.16	0.02	0.02	-0.17	-0.16
23/12/94	0.00	0.00	-0.22	-0.18	-0.20	-0.16	0.02	0.03	-0.20	-0.16
02/12/95	-0.00	-0.00	-0.20	-0.16	-0.18	-0.14	0.03	0.01	-0.18	-0.14
17/08/95	-0.00	-0.00	-0.34	-0.25	-0.30	-0.22	0.04	0.03	-0.30	-0.22
18/12/95	0.00	-0.00	-0.22	-0.18	-0.18	-0.17	0.03	0.01	-0.18	-0.17
07/04/96	-0.01	-0.00	-0.26	-0.19	-0.28	-0.20	-0.01	-0.00	-0.27	-0.19
31/08/96	0.00	0.00	-0.24	-0.21	-0.21	-0.17	0.03	0.04	-0.21	-0.18
13/12/96	0.01	0.00	-0.24	-0.22	-0.25	-0.14	-0.01	0.08	-0.25	-0.14
06/06/97	0.00	0.00	-0.24	-0.16	-0.21	-0.14	0.03	0.02	-0.21	-0.14
14/11/97	0.00	0.00	-0.22	-0.16	-0.19	-0.13	0.03	0.03	-0.19	-0.13
02/06/98	-0.00	-0.00	-0.33	-0.22	-0.26	-0.18	0.07	0.03	-0.26	-0.18
07/12/98	-0.00	0.00	-0.33	-0.16	-0.27	-0.12	0.07	0.04	-0.27	-0.12
24/02/00	0.00	0.00	-0.37	-0.18	-0.28	-0.11	0.09	0.07	-0.28	-0.11
12/11/00	-0.01	-0.01	-0.28	-0.13	-0.25	-0.11	0.04	0.03	-0.24	-0.10
Average	–	–	–	–	–	–	0.03	0.03	-0.22	-0.16
Rms	–	–	–	–	–	–	0.02	0.02	0.04	0.04

The descriptions for the columns of Table 5.2 are given as follows:

Columns:

(1): The date of observations,

(2)-(3): The position offsets of the peak brightness point (w.r.t an arbitrary reference position used at the correlator) of the elliptical GAUS model (centre) for each epoch,

(4)-(5): Fiducial point: 60% FWHM (south-west) points of the elliptical GAUS model for each epoch,

(6)-(7): The position offsets of the peak brightness point (w.r.t an arbitrary reference position used at the correlator) of the ASYM model (apex) for each epoch,

(8)-(9): Relative positions from the ASYM (apex) model to the fiducial point within each epoch,

(10)-(11): Relative positions from the ASYM (apex) model to the elliptical Gaussian (centre) model within each epoch.

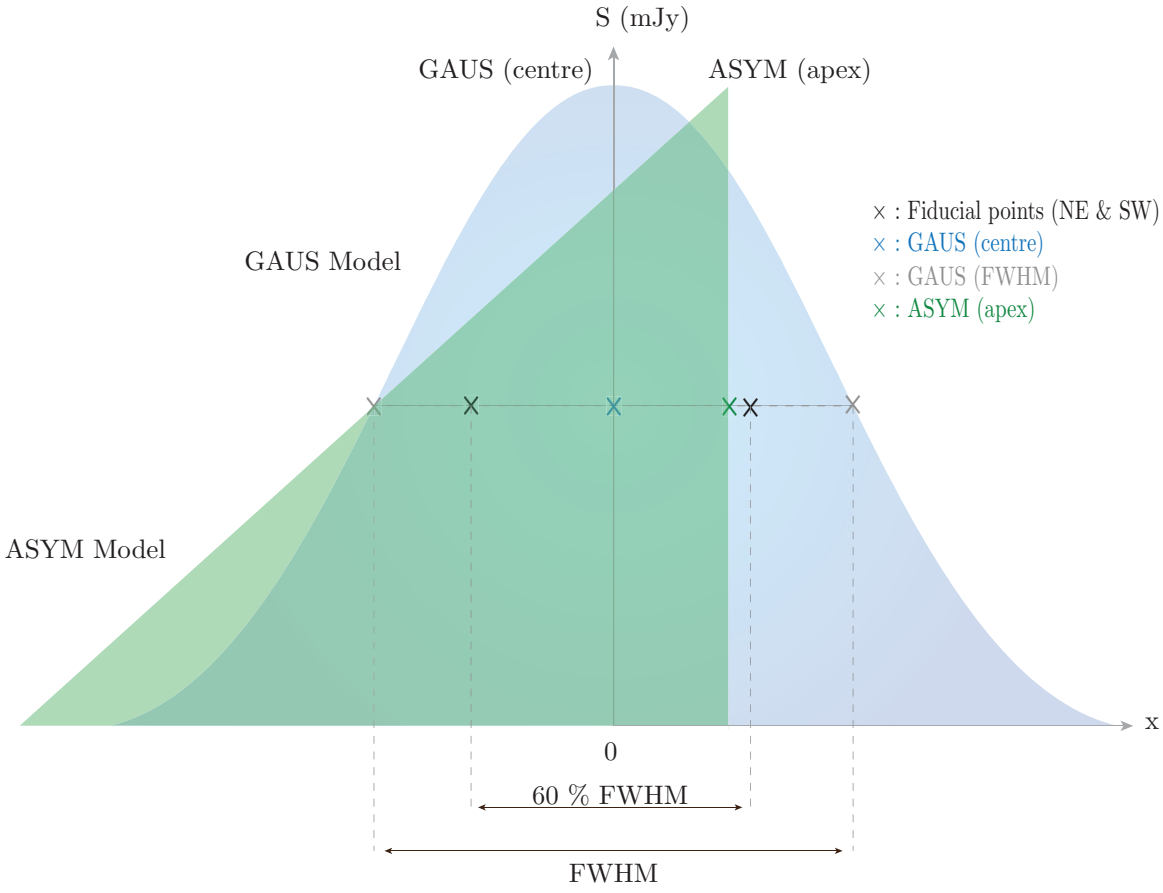

Figure 5.4: A schematic diagram of the elliptical Gaussian model (GAUS) where the position of the brightness peak is identical with the geometrical centre-point of the GAUS model (i.e., close to the nominal position), and the peak brightness position of the ASYM model is slightly offset from the GAUS centre-point.

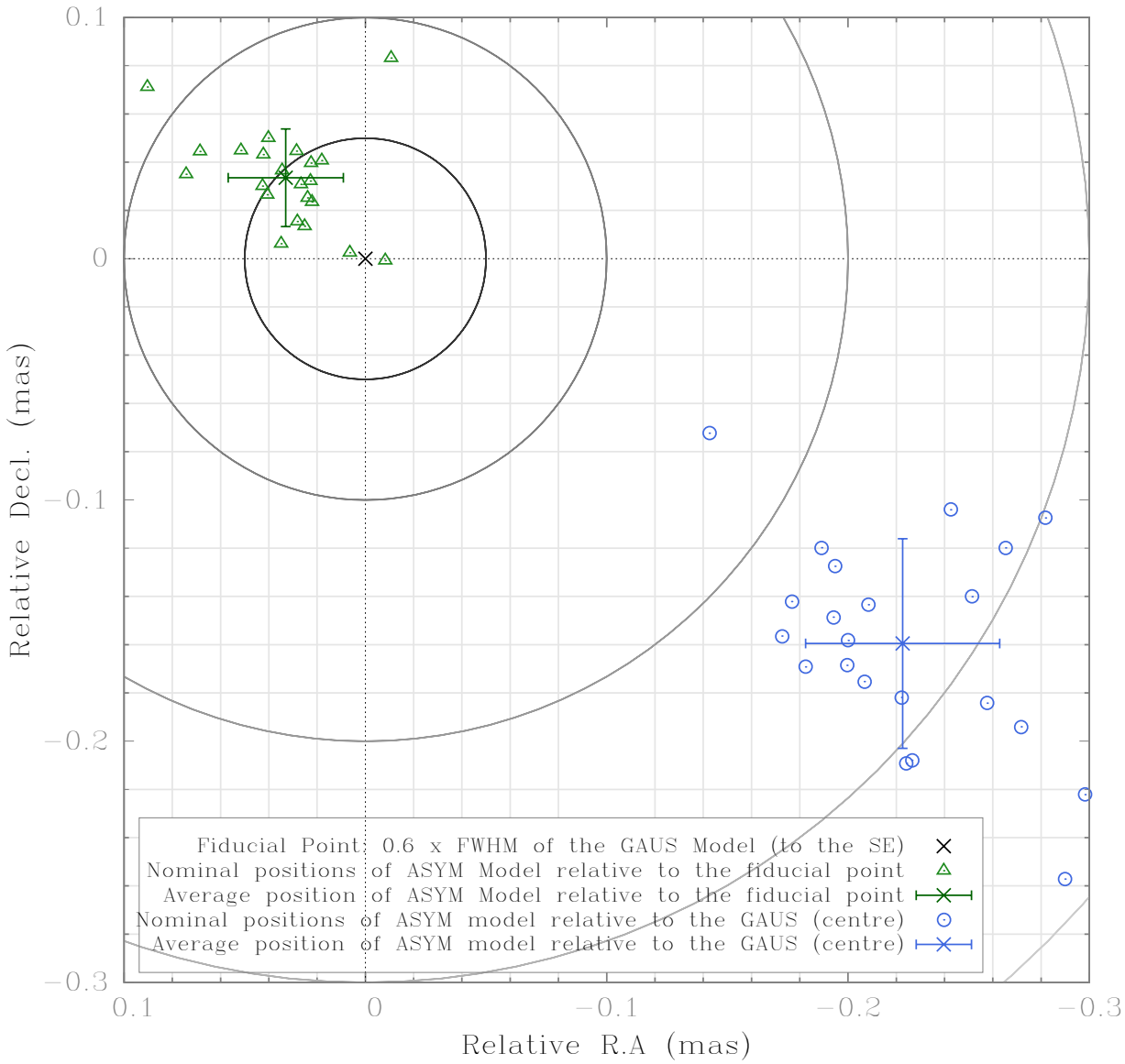

Figure 5.5: The relative positions of the GAUS and ASYM models peak brightness with respect to a fiducial point, which is 60% of the FWHM along the fitted major axis of the GAUS model, in the southwest direction, for each epoch of observations. The *blue empty circles* and *empty green triangles* show the position offsets of the fitted GAUS model (centre) and fitted ASYM model (apex) respectively (arbitrary reference position used at the correlator) both relative to the fiducial point. The blue and green crosses show the average position offsets over all epochs at 8.4 GHz for each fitted positions of the ASYM model relative to the GAUS (centre), and ASYM model relative to the fiducial point, with the plotted rms variation being 40 μas and 20 μas respectively. A grid and concentric circles of radius 0.05, 0.1, 0.2, and 0.3 mas are plotted to show the range where the peak brightness points of the models are located relative to the fiducial point.

Summary of Chapter 5 - Results and Discussions:

1. The purpose of this chapter was to explain the defining parameters and variability of the GAUS and ASYM models estimated for each epoch and frequency to characterise the emission region of M81*.

   (a) The long-term radio light curves show that M81* is highly variable and the flux densities at 8.4 and 5.0 GHz are strongly correlated for both models, with active flaring episodes. We also observed a major outburst lasting $\sim$ 4 years that was reported by Martí-Vidal et al. in 2011. Both the fitted GAUS and ASYM increases from June of 1997 to a maximum ($\sim$ 209 mJy at both frequencies) in November 1998 and then begins to decrease through June 2001. We suggest that the outburst could have led to the ejection of a newly detected feature, i.e., a knot (e.g., see Figure 3.8).

   (b) The average values of the fitted major axis of the GAUS at 5.0 and 8.4 GHz suggest that the jet is systematically larger at a lower frequency. In addition, the fitted minor axis of the GAUS model (average) indicates that the nuclear region of M81* at a lower frequency is relatively broader. The fitted length of the ASYM model is much larger on average and it is proportional compared to the GAUS: FWHM model at 8.4 GHz. We argued that given ASYM results on length, p.a., and flux density are well correlated with those from the GAUS model, the increase in the length of the ASYM model seems to reflect the extent of the 50% point of both models. Lastly, no apparent increase in the length of either GAUS or ASYM models were observed which corresponds to the increase in the flux density during the four-year-long radio flare.

   (c) The position angles of the fitted GAUS and ASYM models are systematically different at different epochs and frequencies. M81* seems to be mostly oriented along the northeast-southwest axis ($\sim 54^\circ$), with the length of the ASYM model closely in line to the p.a. of the major axis of the GAUS model for most epochs. We suggest that this result hints at an underlying structure of M81* being mostly linear, reminiscent of a jet. The variations of the p.a. of both models appear very similar and vary smoothly for most epochs.

2. Even though we made use of some additional data (1997 onwards), the values and interpretation of the temporal and structural variability of the GAUS model at 8.4 GHz in this thesis are in close agreement to that reported by Bietenholz et al. (2000). Fitting a GAUS model with VLBI data at two different frequencies (8.4 and 5.0 GHz), plus an additional model (i.e., ASYM), further solidify our insights into the variability of M81*.

3. Lastly, we have shown that on average, the estimated distance of the brightness peak of ASYM relative to the fiducial point (i.e., 60% FWHM point) is surprisingly close, 47 ± 20 μas (corresponds to $\sim$ 186 AU at a distance of 3.96 ± 0.29 Mpc from Earth) at an angle of 45.5° which is $\sim$ 6 times closer than the peak brightness of a GAUS model. This implies that the ASYM model may hold some promise to estimate the core position in AGN, befitting geodesists and the phase-reference astronomy. To convincingly argue about the reliability of ASYM to locate the core position remains to be demonstrated for other AGN.

'Nothing is more powerful than an idea *whose time has come.'*

– Victor Hugo

6

Conclusions and Future Outlook

6.1 The Nature of M81*

VLBI study of compact radio sources provides an opportunity to probe the inner nuclear region of AGN. Over the course of many years, extensive and detailed VLBI observations of high-luminosity AGN jets have been made to reveal their nature (e.g., see Zensus, 1997). At a lower-power level, the nature of the compact radio nuclei in LLAGN is still unclear (Falcke et al., 2004), including that of M81*.

At the smallest scales, the radio emission emanating from nuclear region of M81* is resolved into a core and a one-sided jet structure. The nuclear region of M81* is thought to be similar to those of large and high-luminosity AGN but at a lower power level. However, owing to the small angular size of M81*, even with its close proximity to Earth, the jet in M81* it not easily discernible (see text, § 3.5.1). For illustration, Figures 5.2 and 5.3 show a time series of images of M81*at 8.4

and 5.0 GHz respectively. The images at 8.4 GHz, in particular, show that M81* to be a very compact source with a small protrusion (reminiscent of a jet) in the northeast direction, varying with epoch.

The prevailing picture of a two-sided jet morphology of an AGN is generally accepted as the basis of unified models. However, owing to relativistic beaming effects (Urry & Padovani, 1995) and/or circumnuclear obscuration from ionized gas distribution in a torus or warped disc (see text, § 3.5.2), an apparent one-sided jet emanating from the central parsec of accretion discs surrounding a SMBH is thought to apply for most AGN. In fact, our sequence of images additionally show that the radio morphology of M81* is not two-sided and does not appear completely symmetrical, it is undoubtedly more extended to the northeast than the southeast in almost all of our images. How much the jet in M81* dominates over the counter-jet is not clear.

The preconceived notion among radio astronomers that many well resolved AGN jet are highly asymmetric with a one-sided jet motivated us to come forth with a new model (i.e., ASYM), which is strictly a one-sided, asymmetric model. By fitting the ASYM model to the visibility data of M81*, we expected our model to be an enhancement over fitting a two-sided, symmetric Gaussian model. The model-fitting technique allows us to investigate the structural variability more quantitatively and use the full resolution capacity of our instrument.

Contrary to what we anticipated, for 77% of our epochs, the ASYM model fits the visibility of M81* poorly compared to both the GAUS model and a one-dimensional Gaussian model, i.e., M81* is closer to a Gaussian than a triangular shape; especially during its outbursts from mid 1997 to mid 2001 as shown in Figure 5.1 and when the brightness distribution of M81* is less extended as shown in Figure 5.2. We argue that the misfit of ASYM at 8.4 GHz suggests that M81* do not conform but rather, is in conflict to the general consensus that AGN are apparently asymmetric at the smallest scales observed with VLBI. Furthermore, the misfit of M81* suggests that M81* is not strictly a core with only an apparent one-sided jetted source, but that it is mostly symmetrical with a significant jet counterpart which cannot be overlooked.

An alternative explanation is that the peak brightness of the radio jet in M81* may be in fact some distance from the stationary core. However, VLBI observations of other well-resolved sources such as the inner jet of M87 have shown that the brightest part of the jet is located at its base (i.e., the region of the jet located closer to the core). For instance, VLBI radio observations of the M87 inner jet show a well-resolved structure extending to within 0.5 mas (0.04 pc) of the

radio core (see Acciari et al., 2009, and references therein). Moreover, with the exception of a few individual sources (where the stationary core identification was not straightforward as the AGN exhibited frequent flares which made the emission from the ejected components to dominate that of the core), a substantial number of AGN jet in the MOJAVE sample show that their brightest feature are located at the extreme end (towards the core) of a one-sided jet at most or all epochs (Lister et al., 2009b).

In closing, we find that M81* may not be representative (i.e., its behaviour would differ) from the broader class of one-sided jets described in the literature, particularly the blazars which are high-luminosity and/or highly beamed sources.

6.2 A Perspective for the Future

The ASYM model has been developed to parameterise marginally resolved sources with a one-sided jet, consisting of the least number of parameters compared to one or more elliptical Gaussians. However, there are rooms to improve the robustness of the ASYM model by making it even more general. What follows are two accessible areas for future investigation that we touch upon.

VLBI images of parsec-scale jets are known to be associated with some degree of bending[1] which we assume is caused by an external pressure gradient interacting with the jet while moving through the nuclear region of the source. For a curved jet, the real p.a. becomes a function of radius, and the single value fitted by the models is an average over the whole length of the jet. Consequently, the incorporation of a *curvature parameter* to a geometrical model can be a useful feature to have. One of the major questions is to find out if the jet flow follows a preset curved trajectory or is ballistic. Ballistic motion can produce a curved jet if it originates from a rotating nozzle, as might be induced if the AGN is part of a binary system.

Moreover, the main result of this thesis suggests that M81* observed at milli-arcsecond level may have some significant amount of jet-counterpart which cannot be overlooked. Therefore, the addition of an *extra "length" parameter*, consisting of another series of point sources for the

[1]Note that a gradient density across the jet, standing shock waves and/or influence of magnetic field, and a precessing nozzle might be responsible for the observable bent in the jet.

jet-counterpart (as illustrated in Figure 6.1) can be used to investigate the degree of sidedness in M81★ and even for other AGN observed at the smallest scales.

The one-dimensional Gaussian and the ASYM models consist of only one position angle and one "length" parameters. So neither can directly estimate the degree of curvature in AGN. However, unlike the one-dimensional Gaussian model, the ASYM model can take up extra parameters without becoming too complex. So the inclusion of the two aforementioned parameters in a two-sided ASYM model could provide us with a wealth of information regarding the structural variability, the degree of bending, and the degree of sidedness in M81★ and in other AGN.

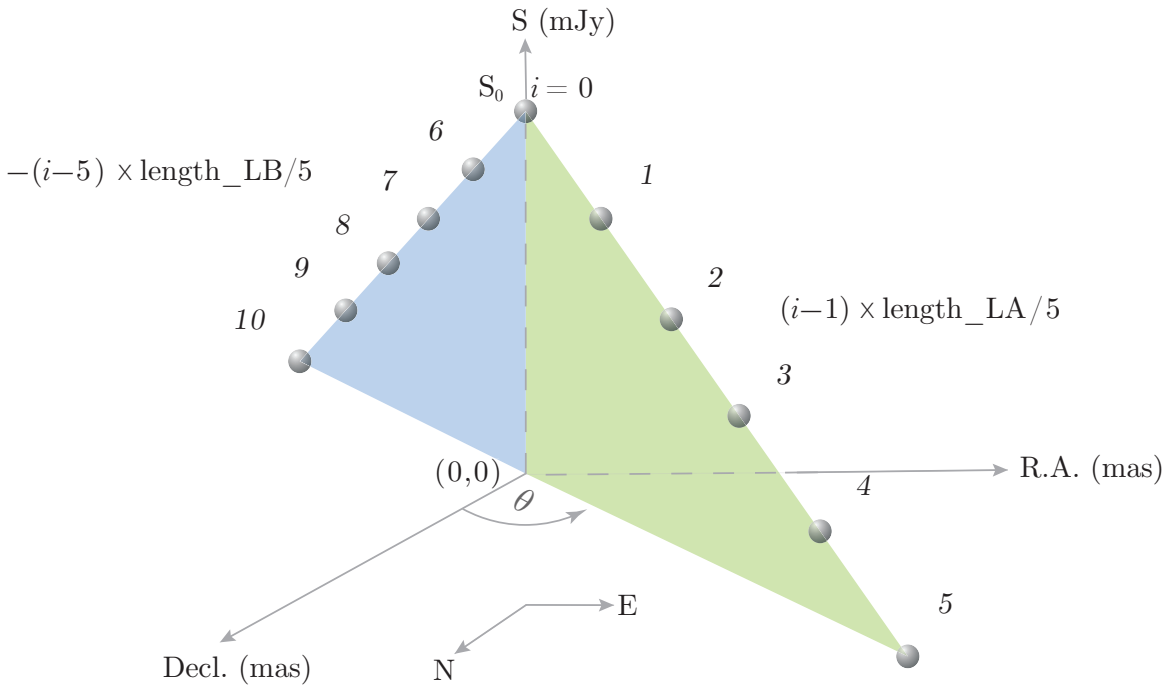

Figure 6.1: Schematic diagram of a two-sided asymmetric triangle model approximated to a collection of point sources which ranges from $i = 0$ to $N - 1$. For the sake of simplicity, the schematic diagram illustrates only 5 point sources on each side of the model, depicting both the jet and the counter-jet, with $i = 0$ is the central point source. The point sources $i = 1$ to 5 are at $(i - 1) \times$ length_LA/5 while the point sources $i = 6$ to 10 are at $-(i - 5) \times$ length_LB/5. The total length parameter of the two-sided ASYM model is L, where L = LA + LB.

Appendices

.1 Model-Fitting Program (OMFIT)

The Algorithm of our OMFIT program used to implement the ASYM model is shown below. To perform the minimization, the OMFIT program starts with some set of model values (such as S0, LA,...), calculates the model FT for each visibility and then examines the SSR as well as the derivatives of SSR with respect to the model parameters. Then it adjusts the model parameters (a new iteration) and repeats until it has converged; see § 2.3.3 for more detail. A full version of the modified OMFIT program (renamed as OMFTA), along with its help file can be downloaded here[2]. The subroutines for the ASYM model begins from line 6225 to 6496 and the explanation of the subroutines, variables, and the include functions are annotated in the OMFTA program.

```
The following source models are supported by our modified OMFIT (OMFTA) program:

 Model  Type    #parameters  parameter description          parameter unit *1*

 'DOT'  Point      3         Flux density of point source    [Jy]
        source               Offset east of phase center     [mas]
                             Offset north of phase center    [mas]

 'GAU'  Gaussian   6         Flux density of Gaussian        [Jy]
                             Offset East of phase center     [mas]
                             Offset North of phase center    [mas]
                             Major axis angular size         [mas]
                             Axial ratio (minor/major)       [dimensionless]
                             Position Angle of major axis    [deg. East of
                                                              North on the sky]

 'ASYM' Asymmetric 5       Flux density of Asymmetric Triangle [Jy]
        Triangle           Offset East of phase center         [mas]
                           Offset North of phase center        [mas]
                           Length of positive extent           [mas]
                           Position Angle of positive extent   [deg. East of
                                                                North on the sky]
```

[2]http://tinyurl.com/Arvind-Ramessur-Thesis-2017

.1.1 Algorithm of the ASYM Model

```
C     Added by Arvind RAMESSUR (Last Updated: 20 Feb 2016)
C     Point Source Approx. of a one-sided triangle Model;
C     ASYM in terms of Total Flux density.
C=======================================================================
      SUBROUTINE ASYMTN (NMOD, SMOD)
C   Input
C      MOD     C*(*)  model code
C   Output
C      NMOD    I      number of parameters for this model type
C      SMOD    I      number of scratch parameters for this model type
C-----------------------------------------------------------------------
C                                 Set up fittables and extra parameters
C-----------------------------------------------------------------------
     INTEGER NMOD, SMOD
C-----------------------------------------------------------------------
C                           5 parameters: x,y (peak brightness points),
C                           log(+ve extent), total flux density and p.a
      NMOD = 5
C     SMOD = ID + NMOD + extra stored XSGOB parameters needed (ID = 5)
C     Extra stored XSGOB: 1-3 = sky (u,v,w), 4 = flux density(non log)
C     5 = +ve extent (non long), and 6,7 = cos(p.a), sin(p.a)
C-----------------------------------------------------------------------
      SMOD = 5 + NMOD + 7
      RETURN
      END
C=======================================================================
      SUBROUTINE ASYMTD (OP, S, PPMOD, PEMOD, UPMOD, UEMOD, CMOD, UMOD)
C                           translate to/from internal values of fitted
C                           parameters to outside world. Called when reading
C                           in starting model and when finished.
C-----------------------------------------------------------------------
C   Input
```

```
C       MOD     C*(*)  model code
C       OP      C*(*)  operation to perform
C   Output
C       CMOD    C*(*)  string containing name of parameters
C       UMOD    C*(*)  string containing units of parameters
C   Input/Output
C       PPMOD   R(*)   Model parameters in internal format
C       PEMOD   R(*)   Model errors in internal format
C       UPMOD   R(*)   Model parameters in external format
C       UEMOD   R(*)   Model errors in external format
C-----------------------------------------------------------------------
      CHARACTER OP*(*),  CMOD(*)*8, UMOD(*)*8
      DOUBLE PRECISION PPMOD(*), PEMOD(*), UPMOD(*), UEMOD(*)
      INTEGER S
      INCLUDE 'ZINFO.INC'
      INCLUDE 'INCS:PSTD.INC'
C-----------------------------------------------------------------------
      IF (OP(1:7).EQ.'To-Prog') THEN
C                                       convert to internal units
C                                       Sanity check
         IF (UPMOD(1) .LT. 0.) UPMOD(1) = 0.
C                                       models unit is total flux
         PPMOD(1) = LOG(UPMOD(1))
         PPMOD(2) = UPMOD(2) * POSSK(S)
         PPMOD(3) = UPMOD(3) * POSSK(S)
         PPMOD(4) = LOG(UPMOD(4) * POSSK(S))
C                                      model is +/- extent
         PPMOD(5) = UPMOD(5) / RAD2DG

      ELSE IF (OP(1:7).EQ.'To-User') THEN
C                                       convert to external units
         UPMOD(1) = EXP(PPMOD(1))
         UPMOD(2) = PPMOD(2) / POSSK(S)
         UPMOD(3) = PPMOD(3) / POSSK(S)
```

```
         UPMOD(4) = EXP(PPMOD(4)) / POSSK(S)
         UPMOD(5) = PPMOD(5) * RAD2DG

C                                        compute external error bars
         UEMOD(1) = UPMOD(1) * PEMOD(1)
         UEMOD(2) = PEMOD(2) / POSSK(S)
         UEMOD(3) = PEMOD(3) / POSSK(S)
         UEMOD(4) = EXP(PPMOD(4))*PEMOD(4) / POSSK(S)
         UEMOD(5) = PEMOD(5) * RAD2DG
C                                        assign labels and units
         CMOD(1) = 'flux    '
         UMOD(1) = 'Jy      '
         CMOD(2) = 'E-offset'
         UMOD(2) = 'mas     '
         CMOD(3) = 'N-offset'
         UMOD(3) = 'mas     '
         CMOD(4) = '+ve ext '
         UMOD(4) = 'mas     '
         CMOD(5) = 'P.A '
         UMOD(5) = 'deg N->E'
         IF (S.EQ.1) THEN
            UMOD(2) = 'asec    '
            UMOD(3) = 'asec    '
            UMOD(4) = 'asec    '
            END IF
         END IF
      RETURN
      END
C=======================================================================
      SUBROUTINE ASYMTS (XMGOB, XSGOB)
C     Update any XSGOBs which change with a change of the fitted parameters
C     (when model changes) but are not dependent on the u,v,w; i.e., have to
C     be recalculated only once per iteration, not once per visibility per iteration).
C-----------------------------------------------------------------------
```

```
      DOUBLE PRECISION XMGOB(*), XSGOB(*)
C     REAL LA, LLA
C     DOUBLE PRECISION LFLUX, FLUX, THETA
      INCLUDE 'ZINFO.INC'
C                                 Declare sky standard
      INCLUDE 'INCS:PSTD.INC'
C                         Include PSTD (parameters related trigonometry).
C     such as PI, GD2RAD, AS2RAD, etc.



C                                  note
C                       XMGOB(1) = log(flux density)
C                       XMGOB(2-3) = posn x,y
C                       XMGOB(4) = log(+ve extent) = LA
C                       XMGOB(5) = p.a
C-----------------------------------------------------------------------
C                       XSGOB(1-3) sky
C                       XSGOB(4) = flux (non log)
C                       XSGOB(5) = +ve extent (non log)
C                       XSGOB(6) = cos(p.a)
C                       XSGOB(7) = sin(p.a)
C-----------------------------------------------------------------------
C     GET SKY OFFSET MODEL
      CALL STDSKI (XMGOB(2), XSGOB(1))
C-------------------------------------------------------------
C     Log(S_tot) = log of total flux density; S_tot = total flux density(non-log)
C     Log(S_tot) = XMGOB(1)
C     S_tot = XSGOB(4)

      XSGOB(4) = EXP(XMGOB(1))
C -------------------------------------------------------------
C     LLA = log of +ve extent, LA;  LA = +ve extent(non-log)
C     LLA = XMGOB(4)
C     LA = EXP(LLA)
```

```
C     XSGOB(5) = LA

      XSGOB(5) = EXP(XMGOB(4))
C-----------------------------------------------------------
C                                      P.A of Model, i.e., THETA
C     THETA = XMGOB(5)
C        storing COS(theta) and SIN(theta) in XSGOBs; Model P.A
      XSGOB(6) = COS(XMGOB(5))
      XSGOB(7) = SIN(XMGOB(5))
      RETURN
      END
C=======================================================================
      SUBROUTINE ASYMTM (U, V, W, UU, UV, VV,
     *   MODC, MODTC, XMGOB, XSGOB, LGOB, LGRAD, GRAD)
C            Calculate model value for each visibility in each iteration.
C            It makes use of the XSGOBs calculated by ASYMTS above.
C-----------------------------------------------------------------------

      INTEGER I, N
      DOUBLE PRECISION U, V, W, UU, UV, VV, XMGOB(*),XSGOB(*)
      COMPLEX MODC, MODTC, GRAD(*), TEM2C, CI, VF, PSHIFT, INVGAIN
      COMPLEX DVI_DLLA, DVI_DPA
      LOGICAL LGRAD, LGOB(*)
      INCLUDE 'ZINFO.INC'
      INCLUDE 'INCS:PSTD.INC'
      REAL S0, LS_tot, LA, SKYP, DEAST, DNORT
      REAL X(1000), Y(1000), S(1000), LLA, SX, P
      PARAMETER (CI = (0.0, 1.0))
      INCLUDE 'INCS:DMSG.INC'
C     INCLUDE 'INCS:DMSG.INC' (AIPS include messaging: For future use!)
C-----------------------------------------------------------------------
C      APPSKI stores the sky offsets for this visibility in SKYP.
       CALL APPSKI (XMGOB(2), XSGOB(1), U, V, W, SKYP, DEAST, DNORT)
```

```
      VF = (0.0, 0.0)
      S_tot = XSGOB(4)
      LS_tot = XMGOB(1)
      LA = XSGOB(5)
      LLA = XMGOB(4)
      COST = XSGOB(6)
      SINT = XSGOB(7)
C     GRAD(1) = (0.0,0.0)
      GRAD(4) = (0.0,0.0)
      GRAD(5) = (0.0,0.0)
C     Test case for the ith point source, (first pt source with index 0)
C     and no. of points, NPOINTS, N (OMFIT_N).
      N = 50

      P = (N+1)*N
      SX = S_tot*2./P

      DO 100 I = 0, N
C     The point source parameters, S_i, X_i and Y_i

C    S_i as a function of S_total:

C             S(I+1) = S_tot/((N+1)/2.)*(N-I)/N

             S(I+1) = SX*(N-I)

             X(I+1) = LA*I/N*SINT
             Y(I+1) = LA*I/N*COST
C-----------------------------------------------------------------------
C     S(i) = flux density of ith point sources.
C     VF = sum of ith point source over N model components
C     Reference:  Arvind Ramessur (MSc Thesis)
C     VF = (SO*(N-I))/N*EXP(-2*PI*CI*LA*(U*I/N*SINT)+(V*I/N*COST))
C     Scaling length(mas)/POSSK: LA*U = LA*U*2*PI
```

```
C      F.T sign convention changed from -ve to +ve (16 Nov 2016).

               VF = VF + S(I+1)*EXP(CI*(U*X(I+1)+V*Y(I+1)))

 100     CONTINUE
C
C      MODTC is the model; S(I+1)*EXP(2*PI*CI*(U*X(I+1)+V*Y(I+1))) or VF times
C      PSHIFT, which  is the position shift (Phase rotation of a complex num)
       PSHIFT = CEXP(CI*SKYP)
       MODTC = VF * PSHIFT
C      MODC: gain correction for the particular visibility (1/_gain)
       INVGAIN = MODC
       MODC = INVGAIN * MODTC
C      TEM2C store j*MODC
       TEM2C = CI * MODC
C
C                Reminder:
C                       XSGOB(1-3) sky
C                       XSGOB(4) = flux or S0
C                       XSGOB(5) = +ve extent (LA) (non log)
C                       XSGOB(6) = cos(p.a)
C                       XSGOB(7) = sin(p.a)
C---------------------------------------------------------------------
C    GRAD are the derivatives of model visibility wrt. model parameters
C    LGRAD: logical variable.
       IF (LGRAD) THEN
          IF (LGOB(1)) GRAD(1) =    MODC
          IF (LGOB(2)) GRAD(2) =    DEAST * TEM2C
C     GRAD(2) = d(model)/dx
          IF (LGOB(3)) GRAD(3) =    DNORT * TEM2C
C     GRAD(3) = d(model)/dy
C ---------------------------------------------------------------------
          IF (LGOB(4)) THEN
C     GRAD(4) = d(model)/dLLA
```

```
             DO 222 I = 0, N
C              DVI_DLLA = DVI/DLA * DLA/DLLA

C              DVI_DLLA = d[ith model component]/dLA
               DVI_DLLA = S(I+1)*EXP(CI*(U*X(I+1)+V*Y(I+1)))*
     *                   CI*(U*X(I+1)+V*Y(I+1))

               GRAD(4) = GRAD(4) + DVI_DLLA
 222         CONTINUE
C              GRAD(4) = sum of DVI_DLLA over N model components
               GRAD(4) = GRAD(4)*INVGAIN*PSHIFT
            END IF
C -------------------------------------------------------------------
          IF (LGOB(5)) THEN
C            GRAD(5) = d(model)/dPA

             DO 333 I = 0, N
C              DVI_DPA = d[ith model component]/dPA
               DVI_DPA = S(I+1)*CI*(U*Y(I+1)-V*X(I+1))
     *                   *EXP(CI*(U*X(I+1)+V*Y(I+1)))
               GRAD(5) = GRAD(5) + DVI_DPA
 333         CONTINUE
C              GRAD(5) = sum of DVI_DPA over N model components
               GRAD(5) = GRAD(5)*INVGAIN*PSHIFT
             END IF
          END IF

 999  CONTINUE
      RETURN
      END
C    End of the ASYM Model
C-------------------------------------------------------------------
```

Bibliography

Acciari, V. A., Aliu, E., Arlen, T., Bautista, M., Beilicke, M., Benbow, W., Bradbury, S. M., Buckley, J. H., Bugaev, V., Butt, Y., & et al. 2009, Science, 325, 444

Anderson, J. M. & Ulvestad, J. S. 2005, ApJ, 627, 674 [ADS]

Bartel, N. & Bietenholz, M. F. 2000, PRO, 1, 17 [ADS]

Bartel, N., Bietenholz, M. F., Rupen, M. P., & Beasley, A. J. 2002, ApJ, 581, 404 [ADS]

Bartel, N., Bietenholz, M. F., Rupen, M. P., & Conway, J. E. a. 2000a, Nature, 368, 610 [ADS]

Bartel, N., Bietenholz, M. F., Rupen, M. P., & Dwarkadas, V. V. 2007, ApJ, 668, 924

Bartel, N., Bietenholz, M. F., & Rupen, M. P. a. 2000b, SCI, 287, 112 [ADS]

Bartel, N., Herring, T. A., Ratner, M. I., Shapiro, I. I., & Corey, B. E. 1986, Nature, 319, 733

Bevington, P. R. & Robinson, D. K. 1992, Data Reduction and Error Analysis for the Physical Sciences, 3rd edn. (New York: Mc Graw-Hill)

Bietenholz, M. F., Bartel, N., & Rupen, M. P. 2000, ApJ, 532, 895 [LINK]

—. 2001, ApJ, 557, 770

Bietenholz, M. F., Bartel, N., Rupen, M. P., Conway, J. E., Beasley, A. J., Sramek, R. A., Romney, J. D., Titus, M. A., Graham, D. A., Altunin, V. I., Jones, D. L., Rius, A., Venturi, T., Umana, G., Weiler, K. W., van Dyk, S. D., Panagia, N., Cannon, W. H., Popelar, J., & Davis, R. J. 1996, ApJ, 457, 604

Bietenholz, M. F., Bartel, N., Rupen, M. P., & Grant, C. S. 2004, ApJ, 615, 173 [LINK]

Blandford, R. D. & Konigl, A. 1979, STI, 232, 34 [ADS]

Blandford, R. D. & Znajek, R. L. 1977, STI, 179, 433 [LINK]

Bower, G. C., Goss, W. M., Falcke, H., Backer, D. C., & Lithwick, Y. 2006, APJL, 648, L127

Bridle, A. H. & Perley, R. A. 1984, ARA&A, 22, 319

Cawthorne, T. V. 1991, Beams and Jets in Astrophysics, p. a. hughes, p. 187 edn. (Cambridge: (Cambridge, Cambridge Univ. Press)

Condon, J. J., Cotton, W. D., Greisen, E. W., Yin, Q. F., Perley, R. A., Taylor, G. B., & Broderick, J. J. 1998, AJ, 115, 1693

Cornwell, T. and Fomalont, E. B. 1999, in Astronomical Society of the Pacific Conference Series, Vol. 180, Synthesis Imaging in Radio Astronomy II, ed. Taylor, G. B. and Carilli, C. L. and Perley, R. A., 187

Cotton, W. D., Feretti, L., Giovannini, G., Lara, L., & Venturi, T. 1999, ApJ, 519, 108

Dent, W. A. 1965, Science, 148, 1458

Devereux, N., Ford, H., Tsvetanov, Z., & Jacoby, G. 2003, ApJ, 125, 1226 [ADS]

Di Matteo, T., Springel, V., & Hernquist, L. 2005, Nature, 433, 604

Doeleman, S. S., Shen, Z.-Q., Rogers, A. E. E., Bower, G. C., Wright, M. C. H., Zhao, J. H., Backer, D. C., Crowley, J. W., Freund, R. W., Ho, P. T. P., Lo, K. Y., & Woody, D. P. 2001, AJ, 121, 2610

Falcke, H., Körding, E., & Nagar, N. M. 2004, , 48, 1157

Fey, A. L. & Charlot, P. 2000, ApJS, 128, 17 [ADS]

Fey, A. L., Clegg, A. W., & Fomalont, E. B. 1996, ApJS, 105, 299

Fomalont, E. B. 1969, ApJ, 157, 1027

Gabuzda, D. C. & Gómez, J. L. 2001, MNRAS, 320, L49

Ghez, A. M., Salim, S., Weinberg, N. N., Lu, J. R., Do, T., Dunn, J. K., Matthews, K., Morris, M. R., Yelda, S., Becklin, E. E., Kremenek, T., Milosavljevic, M., & Naiman, J. 2008, ApJ, 689, 1044

Gillessen, S., Eisenhauer, F., Trippe, S., Alexander, T., Genzel, R., Martins, F., & Ott, T. 2009, ApJ, 692, 1075

Hada, K., Doi, A., Kino, M., Nagai, H., Hagiwara, Y., & Kawaguchi, N. 2011, Nature, 477, 185–187

Heckman, T. 1980, A&A, 87, 1 [ADS]

Hirabayashi, H., Hirosawa, H., Kobayashi, H., Murata, Y., Edwards, P. G., Fomalont, E. B., Fujisawa, K., Ichikawa, T., Kii, T., Lovell, J. E. J., Moellenbrock, G. A., Okayasu, R., Inoue, M., Kawaguchi, N., Kameno, S., Shibata, K. M., Asaki, Y., Bushimata, T., Enome, S., Horiuchi, S., Miyaji, T., Umemoto, T., Migenes, V., Wajima, K., Nakajima, J., Morimoto, M., Ellis, J., Meier, D. L., Murphy, D. W., Preston, R. A., Smith, J. G., Tingay, S. J., Traub, D. L., Wietfeldt, R. D., Benson, J. M., Claussen, M. J., Flatters, C., Romney, J. D., Ulvestad, J. S., D'Addario, L. R., Langston, G. I., Minter, A. H., Carlson, B. R., Dewdney, P. E., Jauncey, D. L., Reynolds, J. E., Taylor, A. R., McCulloch, P. M., Cannon, W. H., Gurvits, L. I., Mioduszewski, A. J., Schilizzi, R. T., & Booth, R. S. 1998, Science, 281, 1825

Ho, L. C. 2008, ARA&A, 46, 475

Ho, L. C., Filippenko, A. V., & Sargent, W. L. W. 1997a, ApJ, 487, 568

—. 1997b, ApJ, 112, 315 [ADS]

Ho, L. C., van Dyk, S. D., Pooley, G. G., Sramek, R. A., & Weiler, K. W. 1999, ApJ, 118, 843 [ADS]

Högbom, J. A. 1974, A&AS, 417 [ADS]

Jennison, R. C. & Das Gupta, M. K. 1953, Nature, 172, 996

Jones, D. L., Wehrle, A. E., Piner, B. G., & Meier, D. L. 2001, ApJ, 553, 968

Kellermann, K. I. 1964, ApJ, 140, 969

Kellermann, K. I., Sramek, R., Schmidt, M., Shaffer, D. B., & Green, R. 1989, AJ, 98, 1195

Konigl, A. 1981, ApJ, 243, 700 [ADS]

Kormendy, J. & Richstone, D. 1995, ARA&A, 33, 581

Krolik, J. H. 1999, Active galactic nuclei : from the central black hole to the galactic environment, 1st edn. (Princeton New Jersey, 1999: Princeton University Press)

Laing, R. A. 1988, Nature, 331, 149

Lister, M. L., Aller, H. D., Aller, M. F., Cohen, M. H., Homan, D. C., Kadler, M., Kellermann, K. I., Kovalev, Y. Y., Ros, E., Savolainen, T., Zensus, J. A., & Vermeulen, R. C. 2009a, AJ, 137, 3718

Lister, M. L., Cohen, M. H., Homan, D. C., Kadler, M., Kellermann, K. I., Kovalev, Y. Y., Ros, E., Savolainen, T., & Zensus, J. A. 2009b, AJ, 138, 1874

Ma, C., Arias, E. F., Bianco, G., Boboltz, D. A., Bolotin, S. L., Charlot, P., Engelhardt, G., Fey, A. L., Gaume, R. A., Gontier, A.-M., Heinkelmann, R., Jacobs, C. S., Kurdubov, S., Lambert, S. B., Malkin, Z. M., Nothnagel, A., Petrov, L., Skurikhina, E., Sokolova, J. R., Souchay, J., Sovers, O. J., Tesmer, V., Titov, O. A., Wang, G., Zharov, V. E., Barache, C., Boeckmann, S., Collioud, A., Gipson, J. M., Gordon, D., Lytvyn, S. O., MacMillan, D. S., & Ojha, R. 2009, IERS Technical Note, 35

Maltby, P. & Moffet, A. T. 1962, ApJS, 7, 141

Marek, A. A., Gunnlaugur, B., & James, E. P. 1998, Theory of Black Hole Accretion Disks, 1st edn. (United Kingdom: Cambridge University Press)

Martí-Vidal, I., Marcaide, J. M., Alberdi, A., Pérez-Torres, M. A., Ros, E., & Guirado, J. C. 2011, A&A, 533, 16 [ADS]

Miyoshi, M., Moran, J., Herrnstein, J., Greenhill, L., Nakai, N., Diamond, P., & Inoue, M. 1995, Nature, 373, 127

Morganti, R. 2002, in Astronomical Society of the Pacific Conference Series, Vol. 258, Issues in Unification of Active Galactic Nuclei, ed. Maiolino, R. and Marconi, A. and Nagar, N., 63

Nagar, N. M., Falcke, H., & Wilson, A. S. 2005, A&A, 435, 521 [ADS]

Parma, P., Fanti, C., Fanti, R., Morganti, R., & de Ruiter, H. R. 1987, A&A, 181, 244

Piner, B. G. & Kingham, K. A. 1997, ApJ, 479, 684

Rees, M. J. 1966, Nature, 211, 468

Reuter, H. P. & Lesch, H. 1996, A&A, 310, L5 [LINK]

Rickett, B. J. 1990, ARA&A, 28, 561

Ripero, J. & Garcia, F. 1993, IAUC, 5731, 1 [ADS]

Rybicki, G. B. & Lightman, A. P. 1979, Radiative Processes in Astrophysics, 1st edn. (Canada: Wiley-Interscience Publication)

Ryle, M. & Hewish, A. 1960, MNRAS, 120, 220

Sakamoto, K., Fukuda, H., Wada, K., & Habe, A. 2001, AJ, 122, 1319 [ADS]

Sandage, A. & Bedke, J. 1994, The Carnegie Atlas of Galaxies. Volumes I, II. by Sandage, A.; Bedke, J (Carnegie Institution of Washington Publ., No. 639)

Schmidt, M. 1963, Nature, 197, 1040

Shields, G. A. 1999, PASP, 111, 661

Sholomitskii, G. B. 1965, , 9, 516

Sovers, O. J., Fanselow, J. L., & Jacobs, C. S. 1998, Reviews of Modern Physics, 70, 1393

Taylor, G. B., Carili, C. L., & Perley, R. 1999, Synthesis Imaging in Radio Astronomy II, 2nd edn., Vol. 180 (San Francisco: ASP Conference Series)

Thompson, A. R., James, M. M., & George, W. Swenson., J. 2001, Interferometry and synthesis in Radio Astronomy, 2nd edn. (Verlag GmbH & Co. KGaA: John Willey & Sons, INC)

Ulvestad, J. S., Wrobel, J. M., Roy, A. L., Wilson, A. S., Falcke, H., & Krichbaum, T. P. 1999, APJL, 517, L81

Unwin, S. C., Cohen, M. H., Hodges, M. W., Zensus, J. A., & Biretta, J. A. 1989, ApJ, 340, 117

Urry, C. M. & Padovani, P. 1995, PASP, 107, 803 [ADS]

Walker, R. C., Dhawan, V., Romney, J. D., Kellermann, K. I., & Vermeulen, R. C. 2000, ApJ, 530, 233

Wilson, A. S., Roy, A. L., Ulvestad, J. S., Colbert, E. J. M., Weaver, K. A., Braatz, J. A., Henkel, C., Matsuoka, M., Xue, S., Iyomoto, N., & Okada, K. 1998, ApJ, 505, 587

Xu, C., Baum, S. A., O'Dea, C. P., Wrobel, J. M., & Condon, J. J. 2000, AJ, 120, 2950

Zensus, J. A. 1997, ARA&A, 35, 607

Zensus, J. A. and Pearson, T. J. 1988, in IAU Symposium, Vol. 129, The Impact of VLBI on Astrophysics and Geophysics, ed. Reid, M. J. and Moran, J. M., 7–16